DISSERTATION

UNDERSTANDING THE DAILY TO DECADAL EVOLUTION OF MOUNTAIN GLACIERS IN ALASKA AND HIGH MOUNTAIN ASIA FROM SATELLITE REMOTE SENSING

Submitted by

Lucas R. Zeller

Department of Geosciences

In partial fulfillment of requirements

For the Degree of Doctor of Philosophy

Colorado State University

Fort Collins, Colorado

Summer 2024

Doctoral Committee:

Advisor: Daniel McGrath

Sean Gallen
Matthew Ross
Caitlyn Florentine

ABSTRACT

UNDERSTANDING THE DAILY TO DECADAL EVOLUTION OF MOUNTAIN GLACIERS IN ALASKA AND HIGH MOUNTAIN ASIA FROM SATELLITE REMOTE SENSING

Glaciers are important components of mountain ecosystems, mountain hydrological systems, and the global water cycle. Improving our scientific understanding of the spatial and temporal variability in glacier changes and the physical processes that drive those changes will allow better prediction of future glacier evolution. In this dissertation, I explore ways in which satellite-based remote sensing products can be used to study mountain glaciers across a wide range of spatial and temporal scales, with a specific focus on Alaska and High Mountain Asia.

The accumulation area ratio (AAR) of a glacier reflects its current state of equilibrium, or disequilibrium, with climate and its vulnerability to future climate change. In Chapter 1, I present an inventory of glacier-specific annual accumulation areas and equilibrium line altitudes (ELAs) for over 3,000 glaciers in Alaska and northwest Canada (88% of the regional glacier area) over the 2018–2022 period derived from Sentinel-2 satellite imagery. I find that the five-year average AAR of the entire study area is 0.41, with an inter-annual range of 0.25–0.49. More than 1,000 glaciers, representing 8% of the investigated glacier area, were found to have effectively no accumulation area. Summer temperature and winter precipitation from ERA5-Land were found to be effective predictors of inter-annual ELA variability across the entire

study area (R^2=0.47). An analysis of future climate projections (SSP2-4.5) shows that ELAs will rise by 170 m on average by the end of the 21st century. Such changes would result in a loss of 25% of the modern accumulation area, leaving more than 1,900 glaciers (22% of the investigated area) with no accumulation area. These results highlight the current state of Alaska glacier disequilibrium with modern climate, as well as their vulnerability to projected future warming.

In High Mountain Asia, many glaciers have thick debris cover over the majority of their ablation zones, earning them the name 'debris-covered glaciers'. Supraglacial lakes (SGLs) play an important role in debris-covered glacier (DCG) systems by enabling efficient interactions between the supraglacial, englacial, and subglacial environments. Developing a better understanding of the short-term and long-term development of these features is needed to constrain DCG evolution and the hazards posed to downstream communities, ecosystems, and infrastructure from rapid drainage. In Chapter 2, I present an analysis of supraglacial lakes on eight DCGs in the Khumbu region of Nepal by automating SGL identification in PlanetScope, Sentinel-2, and Landsat 5–9 satellite images. I identify a regular annual cycle in SGL area, with lakes covering approximately twice as much area during their maximum annual extent (in the pre-monsoon season) than their minimum annual extent (in the post-monsoon season). The high spatiotemporal resolution of PlanetScope imagery (~ daily, 3 m) shows that this cycle is driven by the appearance and expansion of small lakes in the upper debris-covered regions of these glaciers throughout the winter. Decadal-scale expansion of large, near-terminus lakes was identified on four of the glaciers (Khumbu, Lhotse, Nuptse, and Ambulapcha), while the remaining four showed no significant increases over the study period. The seasonal variation in

SGL area is of comparable or greater magnitude as decadal-scale changes, highlighting the importance of accounting for this seasonality when interpreting long-term records of SGL changes from sparse observations. The complex spatiotemporal patterns revealed in this analysis are not captured in existing regional-scale glacial lake databases, suggesting that more targeted efforts are needed to capture the true variability of SGLs on large scales.

In Chapter 3, I expand these methods across a wider spatial extent by using the Landsat 5, 7, 8, and 9 archive to delineate SGLs on debris-covered glaciers across all of High Mountain Asia at near-annual cadence from 1988–2023. I find that SGL area has increased throughout the study period, rising to 17.2 km^2 (0.7% of the investigated debris-covered area) in 2023, compared to ~8 km^2 (0.3% of debris-covered area) in 1988. SGL growth is most concentrated in the Himalaya and Nyainqêntanglha regions, which have also experienced the greatest rates of 20th and 21st century mass loss. The 21st century SGL growth is concentrated almost entirely near the termini of these glaciers, indicating the possibility of continued growth and coalescence into large proglacial lakes. Areas of high SGL concentration are predominantly found in areas with lower surface gradients, low velocity, and thicker debris cover. Glaciers with high SGL concentrations are found to have steeper longitudinal gradients of thinning, with greater thinning rates further from the terminus resulting in lower surface slopes and more concave geometries throughout their entire debris-covered extents. However, the representative longitudinal thinning pattern of glaciers without substantial SGL formation have become more similar to this pattern in recent years, suggesting that more of these glaciers may be primed for SGL formation in the future.

ACKNOWLEDGEMENTS

I am immensely grateful for the many people who have made this work possible. I would like to thank my advisor, Dan McGrath, for his continuous advice, support, and trust throughout the entire course of this PhD and master's, and for allowing me the freedom to explore and develop as a scientist. Thank you to my committee members, Caitlyn Florentine, Sean Gallen, and Matt Ross, for the support and time which they have given.

Thank you to the many collaborators and mentors, in both official and unofficial capacities, who have contributed to this work. The entire High Mountain Asia research team, and Scott McCoy and Jack Jacquet for their teamwork, suffering, and laughter while we were in Nepal. The USGS Benchmark Glacier Project for their invaluable guidance and my unofficial committee member Louis Sass for your insight and words of encouragement. To the community surrounding me at Colorado State University who I have enjoyed working with immensely, particularly the past and present research crew of Randall, Bri, Wyatt, Holly, Ash, and Ally.

Thank you Mom, Dad, Dan, Rae, and the too many aunts, uncles, cousins, and grandparents to list, for your unwavering support and confidence in me.

And to Anna, for always being there every step of this journey.

TABLE OF CONTENTS

LIST OF TABLES

LIST OF FIGURES

1. INTRODUCTION

Glaciers are key components of human-environmental systems across the world. Mountain glaciers (excluding those in Greenland and Antarctica) cover more than 700,000 km^2 of the Earth's surface, with a total volume of 158,000 km^3 (Farinotti and others, 2019; RGI Consortium, 2023). They promote ecological and environmental heterogeneity via their control on fluxes of water temperature, nutrients, and sediments (Lane and others, 2017; Cauvy-Fraunié and Dangles, 2019), are popular tourism destinations (Purdie and others, 2015), and provide avenues for natural recreation and exploration (Welling and others, 2015). They are also a source of fresh water for human consumption, crop irrigation, and hydroelectric power even during times of drought (Pritchard, 2019; Immerzeel and others, 2020), making them an important component of high-mountain environments which have been coined "the world's water towers".

Mountain glaciers across the globe have been retreating and losing mass over the 20th and 21st centuries in response to climate change, and have become one of the iconic images of global warming (Zemp and others, 2019; Wouters and others, 2019; Ciracì and others, 2020; Hugonnet and others, 2021; Jakob and Gourmelen, 2023). Rates of mass loss have accelerated from ~50 gigatons per year (~1.4 mm sea level rise per decade) in the 1960–2000 period to ~250 gigatons per year (~7 mm sea level rise per decade) in the 21st century (Zemp and others, 2019; Hugonnet and others, 2021). Glacier mass loss will continue in the coming decades (Hock and others, 2019; Rounce and others, 2023). Future mass loss rates and timing are dependent on the specific carbon emissions scenario used for modeling, and may peak anywhere between 2035 at 13 mm sea level rise per decade (assuming 1.5 °C of warming) or after 2100 at >22 mm sea level rise per decade (assuming 4 °C of warming) (Rounce and others, 2023).

The impacts from glacier mass loss are felt on local to global scales. On global scales, melting glaciers contribute to sea level rise. Recent studies estimate that the water contained in mountain glaciers is equivalent to 32 cm of sea level rise (Farinotti and others, 2019). The mass loss and subsequent sea level rise contribution of mountain glaciers from 1900–2018 is of comparable or even slightly greater magnitude relative to that of the Antarctic and Greenland ice sheets, despite holding only a small fraction of their ice volume (Frederikse and others, 2020). By the end of the 21st century, mountain glacier contribution to sea level rise is projected to be ~9–15 cm relative to 2015 (Rounce and others, 2023). Including ice sheet mass losses increases these estimations of sea level rise to ~13–25 cm under typical emissions scenarios, and as much as 42 cm if more "pessimistic" assumptions of Antarctica mass-balance feedbacks are made (Edwards and others, 2021). Even the best-case scenarios represent enough sea level rise to displace hundreds of millions of people living in coastal areas around the globe (Kulp and Strauss, 2019).

On a more local scale, as glaciers melt, the magnitude and timing of their ecosystem services shift (e.g. downstream supply of cold water, sediments and nutrients) (Huss and others, 2017; Milner and others, 2017). For example, with warmer temperatures, end-of-winter glacier ice and snow melt will transition to beginning earlier in the spring season, and earlier melt-out of snowpack will decrease late-summer and autumn streamflow contributions (Beamer and others, 2017). Initially, as a glacier melts its net annual runoff will increase. However, over time as the glacier becomes smaller and holds less mass, the net annual runoff will begin decreasing until eventually the glacier disappears and no longer provides late-summer runoff (Huss and Hock, 2018). The timing of this transition from increasing glacier runoff to decreasing glacier runoff is referred to as “peak water”. Understanding these patterns at both the basin and global scale is important for knowing how to best adapt to the future water regimes, but is highly dependent on specific glacier geometry, regional climate, and the uncertainty of future climate (Zekollari and others, 2020; Rounce and others, 2023). Recent estimates show that “peak water” may have already passed in some regions (e.g. New Zealand and the Low Latitudes); in other regions, peak water is projected to pass at some point in the 21st century (from 2060–2080 in Alaska, 2025–2030 in South Asia East, 2035–2055 in Central Asia, and 2050–2075 in South Asia West) (Huss and Hock, 2018; Rounce and others, 2023).

As glaciers retreat, cryosphere-related hazards are also expected to become more frequent (Stoffel and Huggel, 2012). Glacial lakes, dammed by terminal moraines after glaciers retreat or by ice in the case of complex branching and/or surging glaciers, can suddenly drain, releasing vast quantities of water into downstream systems which threaten human settlements, infrastructure, and fragile environments (Veh and others, 2020; Rick and others, 2022). Slope instabilities and related mass movements from recently deglaciated mountainsides, or from thawing permafrost, can cause direct damage to areas below them or initiate cascading downstream hazards (such as causing lakes to breach their dams and catastrophically drain) (Deline and others, 2021; Shugar and others, 2021). In rare cases, entire glaciers can suddenly detach from their bed and result in massive ice-rock avalanches (Evans and others, 2009; Kääb and others, 2021). Accurately predicting the occurrence of these events is difficult (or impossible), but they represent a serious and growing risk to communities and infrastructure in the vicinity of these environments.

Historically, glacier mass changes have been measured and monitored using primarily in-situ methodologies which involve the interpolation or extrapolation of point measurements of glacier mass gain or loss across an entire glacier (Sass and others, 2017; O'Neel and others, 2019). Geodetic methods (using digital elevation models captured at different points in time to measure the change in the glacier surface elevation) are often used in conjunction to account for limitations and systematic biases present in these in situ measurements (Huss, 2013; Klug and others, 2018; Zeller and others, 2023). For example, taking measurements within heavily crevassed ice falls is difficult (Colgan and others, 2016), lingering in areas prone to avalanching is unwise (Florentine and others, 2020), and accessing the glacier bed to measure basal melt is effectively impossible (Alexander and others, 2011), and these areas all experience mass change processes that are distinct from the locations where in situ measurements are made. These in situ measurements of single glaciers can then be extrapolated to the regional or mountain-range scale (often in tandem with remotely-sensed geodetic data) by using careful assumptions about topography and climate patterns (Huss, 2012).

The rise in the availability of freely-available satellite-based remote sensing observations of the earth has ushered in a new era of measuring and observing glaciers and glacier changes at continental- to global-scales. Within the last five years, global-scale glacier-specific measurements of ice thickness (Farinotti and others, 2019; Millan and others, 2022), ice flow velocity (Gardner and others, 2022; Millan and others, 2022), debris cover extent (Scherler and others, 2018; Herreid and Pellicciotti, 2020), debris-cover thickness (Rounce and others, 2021), glacial lake abundance (Shugar and others, 2020), and glacier mass change (Hugonnet and others, 2021) have been developed. The availability of such datasets has enabled vast improvements in the understanding of the physical drivers of glacier changes (Brun and others, 2019), changes in glacier-related hazards (Furian and others, 2022), and more accurate modeling of global glacier evolution (Rounce and others, 2023).

With that being said, there are still many aspects of glaciology which remain unknown and unstudied. These knowledge gaps include limitations in our understanding of descriptive understanding of their surface features/processes as well as the spatial and temporal variability of their physical, hydrologic, and climatological attributes. For example, the creation of a consistent and accurate delineation of the global extent of glaciers is an ongoing task (RGI Consortium, 2023), and the creation of a globally-accurate time-varying inventory from satellite observations has not been attempted.

As glacier mass loss continues in the coming years and decades (Rounce and others, 2023), there is an urgent need to continue to develop ways of utilizing satellite remote sensing products for studying mountain glaciers. Such techniques are needed to develop improved observational datasets, improve our understanding of glaciological processes, and to improve predictions of future changes in these mountain environments.

With these questions in mind, my dissertation is focused on utilizing satellite remote sensing tools to investigate mountain glaciers across a wide range of spatial and temporal scales. This research is split into three chapters.

Chapter 1 is focused on glaciers in Alaska and northwest Canada. In this study, I use Sentinel-2 satellite imagery to investigate the spatial and temporal patterns of end-of-summer snow covered areas of ~3,000 glaciers across a five-year study period (2018–2022). I combine these observations with glacier topography, climate reanalysis products, and climate projections to investigate the glaciers' vulnerability to future climate change.

I show that more than 1,000 glaciers, representing 8% of the investigated glacier area, have effectively no accumulation area, meaning they are entirely out of equilibrium with modern climate and are guaranteed to be unable to survive in their present form. Based on future climate projections, glacier equilibrium line altitudes are expected to rise by 170 m on average by the end of the 21st century. Such changes would result in a loss of 25% of the modern accumulation area and leave more than 1,900 glaciers (22% of the investigated area) with no accumulation area. These results paint a picture of how glaciers in Alaska are out of equilibrium with modern climate, will continue to become even more out of equilibrium, and are certain to undergo major changes (retreat and mass loss) in the coming decades.

Chapter 2 is focused on eight glaciers in the Sagarmāthā (Mount Everest) region of Nepal which have thick debris cover over the majority of their ablation zones (hence the name 'debris-covered glaciers'). I use PlanetScope imagery (~3 m imagery at ~daily cadence) to delineate the extent of supraglacial lakes (SGLs) on these glaciers at high spatial and temporal resolution over the 2017–2022 time period. From this dataset, I investigate the short-term (seasonal-to-annual) patterns in SGL variability. I then use these observations as a validation dataset to optimize SGL identification in coarser-resolution Landsat and Sentinel-2 imagery, allowing an investigation into the decadal-scale trends in SGL evolution at coarser spatial scale (10 and 30 m). Direct field observations and uncrewed aerial system (UAS) surveys from May 2023 provided additional insight into the local-scale topography of these glaciers. I identify a regular annual cycle in SGL area, with lakes covering approximately twice as much area during their maximum annual extent (in the pre-monsoon season) than their minimum annual extent (in the post-monsoon season). This cycle is driven by the appearance and expansion of small lakes in the upper debris-covered regions of these glaciers throughout the winter. These seasonal variations in SGL area are of comparable or greater magnitude as decadal-scale changes, highlighting the importance of accounting for this seasonality when interpreting long-term records of SGL changes from sparse observations. The complex spatiotemporal patterns revealed in this analysis are not captured in existing regional-scale glacial lake databases, suggesting that more targeted efforts are needed to capture the true variability of SGLs on large scales.

In the final chapter, I apply the methodology developed for Chapter 2 across a wider spatial extent by using the Landsat 5, 7, 8, and 9 archive to delineate SGLs on debris-covered glaciers across all of High Mountain Asia at near-annual cadence from 1988–2023. Using this dataset, I investigate the spatial and temporal variability of SGLs across the region, finding that SGL area has increased throughout the study period, rising to 19.4 km^2 (0.8% of the investigated debris-covered area) in 2023, compared to ~10 km^2 (0.4% of debris-covered area) in

1988. This SGL growth is most concentrated in the Himalaya and Nyainqêntanglha regions as a result of these regions experiencing the greatest rates of mass loss in the 20th and 21st centuries. Furthermore, this 21st century SGL growth is concentrated almost entirely near the termini of these glaciers, indicating the possibility of continued growth and coalescence into large proglacial lakes.

Each chapter is formatted as a manuscript for submission to a peer-reviewed journal, with self-contained introduction, study area, methodology, results, and discussion sections. Chapter 1 has been published in the *Journal of Glaciology* (Zeller and others, 2024a), Chapter 2 has been published in *The Cryosphere* (Zeller and others, 2024b), and Chapter 3 is in preparation for submission to *Geophysical Research Letters.* Supplementary text, tables, and figures (where appropriate) for each chapter are provided in the appendices (Appendix A for Chapter 1, Appendix B for Chapter 2, Appendix C for Chapter 3).

CHAPTER 1: EQUILIBRIUM LINE ALTITUDES, ACCUMULATION AREAS, AND THE VULNERABILITY OF GLACIERS IN ALASKA[1]

1.1. Introduction

Glaciers play an important role in a wide range of both human and ecological systems (O'Neel and others, 2015; Immerzeel and others, 2020). Global observations show that glaciers have lost mass throughout the 20th and 21st centuries, and mass loss from glaciers in Alaska and northwest Canada (the Randolph Glacier Inventory "Alaska region"; (RGI Consortium, 2017)) outpaced any other region (Larsen and others, 2015; Zemp and others, 2019; Hugonnet and others, 2021). Global glacier mass loss will continue through the end of the century, and glaciers in the Alaska region are projected to provide the largest contribution to global sea level rise in the 21st century of any glacierized region on Earth (Rounce and others, 2023).

Repeated, systematic observations of glacier mass balance provide critical information for understanding how glaciers respond to a changing climate (Zemp and others, 2009). However, fewer than 0.1% of glaciers in the Alaska region have consistent and long-term in situ

[1] Chapter 1 is published in the *Journal of Glaciology* as "Equilibrium line altitudes, accumulation areas, and the vulnerability of glaciers in Alaska" (Zeller and others, 2024a)

observations (U.S. Geological Survey Benchmark Glacier Program and others, 2016). Geodetic remote sensing methods offer a complementary approach to collecting direct measurements, providing insight into glacier mass balance across local to global scales. However, geodetic mass balance approaches are affected by a variety of potential biases related to limitations on glacier area change datasets (Florentine and others, 2023), different processing steps in the elevation data processing chain (Piermattei and others, 2023), and the time intervals over which they can be applied (Huss, 2013).

The elevation of the boundary between the snow-covered and snow-free portions of a glacier is referred to as the transient snow line altitude (SLA). For glaciers with a distinct accumulation and ablation season (such as the Alaska region), the SLA at the end of the ablation season can be used as a proxy for the annual equilibrium line altitude (ELA) (Rabatel and others, 2012). The area which remains snow covered at the end of the ablation season represents the glacier's accumulation area (AA), which can be used in conjunction with the total glacier area to calculate the glacier's accumulation area ratio (AAR) (Cogley and others, 2010). Further, this snow covered area on a glacier surface is readily observable from space-based platforms by differentiating the areas of a glacier which are covered in snow from those which are ice or firn, because snow has higher reflectance across visible and near-infrared wavelengths (Gao and Liu, 2001).

The ELA and AAR provide insight into the relationship between local climate and glacier mass balance on short (annual) time scales, as variations in the ELA and AA respond to changing patterns and magnitudes of snow accumulation and ablation. Remotely-sensed observations of these variables can be used for translating long-term geodetic mass balance measurements to annual time steps (Davaze and others, 2020), investigating glacier vulnerability and disequilibrium (McGrath and others, 2017; Carturan and others, 2020; Lorrey and others, 2022), and calibrating glacier models (Geck and others, 2021).

Many previous studies have explored approaches to extracting the SLA from optical satellite imagery, with a focus on identifying the snow-covered areas from Landsat imagery using methods that range from manual delineation to fully automated classification approaches. These studies have focused on glaciers in the Tropics (Rabatel and others, 2012), the European Alps (Rabatel and others, 2008; Rastner and others, 2019; Prieur and others, 2022) and High Mountain Asia (Racoviteanu and others, 2019; Guo and others, 2021), or a global sample of glaciers (Li, Wang, and others, 2022), but very few have utilized the higher spatial and temporal resolution of Sentinel-2 imagery (Kavan and Haagmans, 2021).

These previous studies tend to be limited to a small sample size of glaciers (fewer than 250), focus on regional-scale SLAs rather than glacier-specific SLAs, and/or have not made the derived datasets accessible for use in other studies. Additionally, few studies have explored SLA and snow cover extraction in the Alaska region, and those that have are focused on a small sample size or regional approximations of snow line variability from coarser-resolution MODIS imagery (Pelto, 2011; Shea and others, 2013).

To evaluate the current state and future vulnerability of glaciers across the entire Alaska region, I create a high-resolution inventory of 2018–2022 end-of-summer AAs and ELAs for over 3,000 glaciers (>76,000 km^2) using an automated classification of Sentinel-2 imagery. Using this dataset I assess the current state of Alaska glacier accumulation areas and investigate the climatic drivers of ELA variability. Lastly, I project how ELAs will change by the end of the century using an ensemble-mean of 13 global climate models and estimate the resulting loss of glacier accumulation area across the region.

1.2. Study Area

I derived AAs and ELAs for glaciers defined by the Randolph Glacier Inventory (RGI) version 6.0 (RGI Consortium, 2017). All glaciers in the Alaska region larger than 2 km^2 were evaluated (Figure 1). This includes 3031 individual glaciers (11% of the 27,108 glaciers in the region) which together cover 76,569 km^2 (>88% of the total glaciated area). Glaciers smaller than 2 km^2 were excluded from this analysis as their smaller size increases the relative effects of misclassification, and local terrain and topography provide more dominant controls on their patterns of snow accumulation and ablation (Florentine and others, 2018). Glacier in the Brooks Range (of which 31 are larger than 2 km^2) were excluded due to their short ablation seasons and limited mass turnover when compared to those at lower altitudes.

The Randolph Glacier Inventory defines five subregions (“O2Regions”) that encompass the study area: the Alaska Peninsula, Alaska Range, West Chugach Mountains, Saint Elias Mountains, and North Coast Ranges. I further divided these into 16 smaller subregions (“O3Regions”), largely following the regions used by (Kienholz and others, 2015). Glaciers are clustered mainly along the coast of the Gulf of Alaska in a maritime climate. Further from the coast, glaciers in the Alaska Range are generally smaller and experience a more interior climate with colder temperatures and less precipitation.

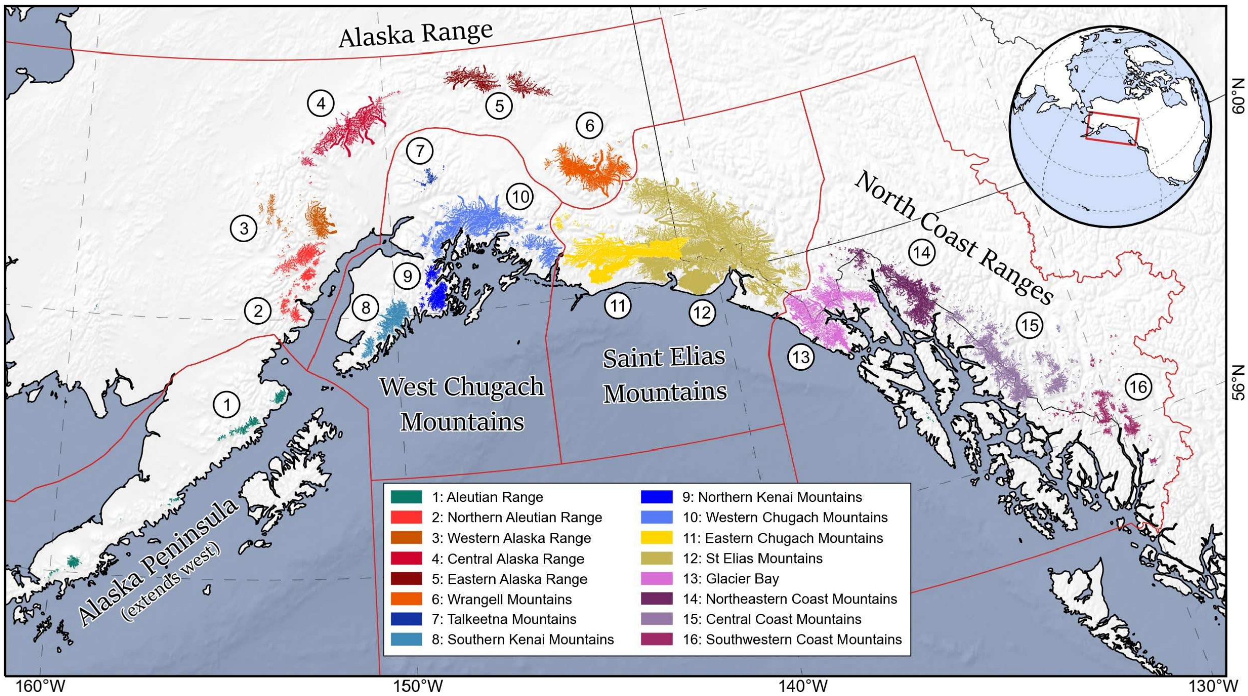

Figure 1: The study area in Alaska and northwest Canada. Glaciers included in the study are mapped, with colors corresponding to their O3Region. The inset legend indicates the color, name, and labeled number of each O3Region. Red outlines and corresponding names indicate the O2Regions defined by the Randolph Glacier Inventory. Inset globe and rectangle show the global context of the area. This map, and all other figures, are presented in the Alaska Albers equal-area projection (EPSG:3338).

1.3. Methods

The snow cover distribution on glacier surfaces was delineated in all 2018–2022 Sentinel-2 multispectral imagery during the May–November months using a random forest classifier. After preliminary filtering and infilling of data gaps, each glacier's SLA was extracted for each observation by identifying the elevation band at which the glacier surface transitioned from majority snow-free (ablation zone) to majority snow-covered (accumulation zone). The maximum SLA was identified from each annual time series of SLAs and taken to represent the ELA. This resulted in a ten-meter resolution annual accumulation area (AA) product for each glacier each year, along with the annual ELA. The five annual AA products for each glacier were then combined to produce a single average AA product, from which the five-year average ELA was calculated. Each of these steps is described in detail in the following sections.

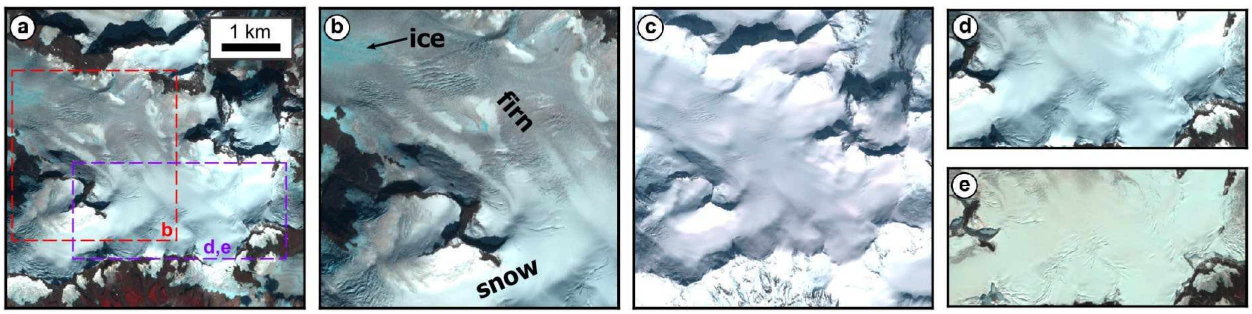

Figure 2: An example of a Sentinel-2 image from which the training data was collected, showing Wright Glacier (RGI60-01.02602) (a), with example snow, firn, and ice regions labeled in (b). Boxes in (a) indicate the extent of (b) (d) and (e). (c–e) shows the process of normalizing imagery by the snow-on mosaic. (c) shows the snow-on mosaic of Wright Glacier, (d) shows a subset of the original image, and (e) shows the effect of snow-on normalization. All images are displayed using the near-infrared, red, and green bands.

1.3.1. Random forest classification

A random forest classifier (Breiman, 2001) was created to classify Sentinel-2 top of atmosphere reflectance images of glaciers into six classes: snow, firn, ice, debris/rock, water, and shadow. I created a training dataset was created in Google Earth Engine (GEE) (Gorelick and others, 2017) from eight Sentinel-2 datatakes (the continuous image strip acquired by a single Sentinel-2 satellite, hereafter called images), with images selected to represent the full spatial and temporal range of the study area. Polygons of each class were manually digitized on each of these eight images (Figure 2). 20,000 pixels of each class were randomly chosen from each image and band values extracted, resulting in 160,000 point observations of each class (960,000 total).

In addition, a representative snow-on mosaic of the study region was created by combining all late-winter (between 19 February and 30 April) cloud-free Sentinel-2 imagery for 2018–2022. Each image's band reflectance was normalized relative to this snow-on mosaic, and these normalized band values were also used as inputs to the random forest classifier. This snow-on normalization was used as a way to provide a topographic correction for variable reflectances caused by variations in the solar incidence angle on the glacier's surface (Figure 2). The normalized difference water index (NDWI) (Gao, 1996) and normalized difference snow index (NDSI) (Dozier, 1989) were calculated for each observation and included as features in the classification (Table A1).

The random forest classifier was trained using the scikit-learn RandomForestClassifier() implementation (Pedregosa and others). Eight-fold cross validation was used for estimating the classifier's accuracy and to tune hyperparameters (*n_estimators* and *max_depth*), with all observations from one of the Sentinel-2 images held out in each "fold" of the cross validation. A final classifier was trained on the entire training dataset using the optimized parameters (*n_estimators*=50, *max_depth*=15, *min_samples_split*=500, *min_samples_leaf*=100, *max_features*='sqrt'), and was imported to GEE.

1.3.2. Snow cover identification

The random forest was used to classify all available Sentinel-2 images of the study glaciers from 2018–2022 between May and November in GEE (n=1.4 million glacier images). Cloudy pixels were masked using the s2cloudless algorithm (Zupanc, 2017) with a cloud probability threshold of 20% (pixels with cloud probabilities higher than this were masked).

Areas with slopes greater than 25° were also masked to avoid misclassification of these areas due to the high solar incidence angles. Terrain shadows were physically modeled and masked out using the GEE TerrainShadow() function, with the Copernicus WorldDEM-30 (GLO-30 DEM) (European Space Agency and Airbus, 2022) and image-specific sun azimuth and incidence angles as inputs.

Binary snow cover maps of each glacier were made for each observation date from the image classification results, distinguishing between accumulation (snow), ablation (firn, ice, debris, and water), and missing data (cloud and shadow) areas. A pixel-wise temporal filter was used to fill missing data and remove outliers in the surface classification by using the most frequently observed class in all other observations up to seven days before and 3 days after. If there were no usable observations in that period, then the pixels were left as no-data. Frequent misclassification of debris cover as clouds by the s2cloudless algorithm was observed, so the debris cover product from Herreid and Pellicciotti (2020) was used to fill in missing data gaps over these areas. Observations were then discarded if they had less than 30% coverage of the glacier surface before applying the filtering and infilling or less than 70% coverage after applying the filtering and infilling.

1.3.3. SLA, ELA, and AAR extraction

A time-varying digital elevation model (DEM) of each glacier was constructed by combining the GLO-30 DEM with glacier-specific elevation change products from Hugonnet and others (2021). The original GLO-30 DEM was taken to represent the 2013 glacier surface elevation, as it was constructed using data acquired during the 2010-12-01 to 2015-01-31

TanDEM-X mission (Rizzoli, Martone, Gonzalez, and others, 2017). X-band radar penetration into snow and ice may introduce uncertainty (less than 4 m penetration depth expected for wet snow) (Millan and others, 2015; Rizzoli, Martone, Rott, and others, 2017), but it is considered negligible for these purposes as I am most interested in relative differences in ELA across space and time rather than using the GLO-30 DEM for point measurements of surface elevation changes. DEMs for each year were constructed by applying the 2010–2014 and 2015–2019 glacier surface elevation change rates, with the 2015–2019 product extended for the years 2020–2022.

The SLA was extracted for each glacier's daily snow-cover products using a modification of the approach described in Rastner and others (2019). The glacier surface area was divided into elevation bands at 10-meter increments. The fractional snow cover of the observed pixels within each band was calculated, and bands with fewer than 50 observed pixels were removed. Bands with at least a 50% snow cover fraction were labeled accumulation bands, and those with less than 50% were labeled ablation bands. The lowest point with at least five consecutive accumulation bands was then taken to represent the SLA of the glacier at that time step. If no SLA was identified, then the lowest point with four consecutive bands, and then three consecutive bands was found. If there was still no SLA identified, then the SLA was assumed to be higher than the elevation range of the glacier, and the SLA is assigned the glacier's maximum elevation. The glacier's AAR was also calculated at each time step as the ratio between the observed snow-covered area and the total observed area of the glacier.

This resulted in a series of accumulation area maps of each glacier (referred to as "observations" below) with an SLA and AAR associated with each. For each glacier each year, the observation with the maximum SLA was chosen to represent its annual accumulation area and ELA. But first, inaccurate observations were filtered out by identifying outliers in each glacier's annual SLA and AAR time series. This works on the assumption that the trend in SLA and AAR over the course of a given melt season should be consistent (with SLA increasing and AAR decreasing). Widespread misclassification of the glacier surface in a single image (for instance from atmospheric noise, or clouds not being properly masked out) would result in the image's derived SLA and AAR being out of sync with the seasonal progression up to that point in time.

For each observation, a linear regression was fit to the SLAs from all other observations in the preceding 60 days, and the expected SLA for the given date was predicted. If the observation of interest had an SLA which was more than 200 m higher than predicted by this linear regression, then the observation was flagged as an outlier and removed. I tested various thresholds and found 200 m to optimize the trade-off between omitting erroneous due to misclassification without excluding real-world changes in SLA. The same process was applied using the AARs, and observations with AARs which were more than 0.15 lower than predicted based on the linear regression were removed. Underestimations of SLA and over-estimations of AAR were never considered outliers, as these conditions are physically realistic effects of new snow accumulation. Similarly, observations from days after the observation of interest were not included in the linear regression because rapid decreases in SLA (and increases in AAR) at the onset of the accumulation season could result in these "true" end-of-summer observations being flagged as outliers.

After these filtering steps, the maximum SLA for each glacier in each year was found, and that observation was taken to represent the end-of-summer accumulation area product and annual ELA. If multiple observations had the same SLA, then the one with the smallest AAR was chosen. For glaciers larger than 500 km^2 (n=22), additional manual selection was used to ensure the optimal end-of-summer observation was chosen. I refer to these products as each glacier's "annual AA" products.

1.3.4. Final formatting

Each glacier's annual AA products were combined to create an average accumulation area product (referred to as the "average AA" products) by taking the most frequent observation of each pixel (defaulting to accumulation area if the number of years of accumulation and ablation were equal). The ELA was then recalculated for these average AA products, to provide a baseline long-term (5-year average) ELA of each glacier. Remaining missing data gaps were then filled in each annual AA and average AA product. Missing data for elevations at or above the ELA were classified as accumulation areas, and those below the ELA were classified as ablation areas. The majority of these missing data pixels were located at higher elevation, north facing slopes which were in terrain shadows across the entire observation period, and were predominantly infilled as accumulation areas. Not accounting for these missing data gaps would lead to a systematic underestimation of accumulation area across the region. The AAR of each product was then recalculated, and these final infilled products were used for subsequent analyses. The RGI glacier outlines (derived predominantly from imagery over the

2004–2010 period) and total glacier area were used for all analyses, as there are no time-varying glacier extent datasets available for the entire study region.

1.3.5. Climate data

To investigate the climatic controls on glacier ELAs and generate future ELA projections, I utilized ERA5-Land (Copernicus Climate Change Service, 2019) reanalysis datasets to investigate the climatic controls on observed glacier ELAs and global climate models from CMIP6 (Eyring and others, 2016) to estimate end-of-century ELA changes. Average daily summer (June, July, August) temperature and total winter (January, February, March) precipitation of each of the 16 O3Regions were calculated from ERA5-Land daily values for 2018–2022, and annual anomalies were calculated for each region in each year. A 13-model ensemble, selected for its representativeness over North America (Mahony and others, 2022), was used for CMIP6 analyses. Ensemble-mean values for the SSP2-4.5 scenario, considered the standard "middle of the road" scenario, were used (O'Neill and others, 2016). Average summer temperature and total winter precipitation was found for the 2013–2022 (modern) and 2090–2099 (future) periods to calculate the projected end-of-century changes in each.

1.4. Results

1.4.1. Classification accuracy

The random forest classifier showed highly accurate results in the cross-validation testing. Throughout the eight cross-validation folds, the median classification accuracy and F1 scores across all classes was 93.1% (with ranges of 67.4–99.8% and 66.7–99.8%, respectively).

When considering just the performance in identifying snow, the median accuracy increases to 99.5% (ranging from 90.1% to 99.9%) and the median F1 score increases to 98.6% (ranging from 76.9% to 99.8%) (Figure 3).

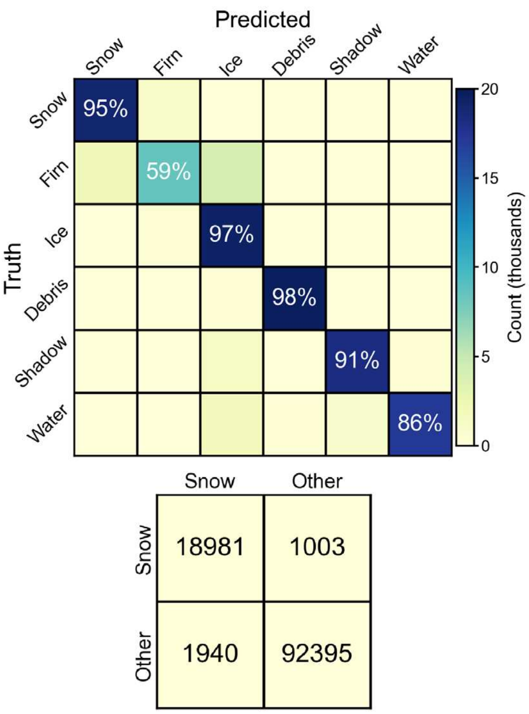

Figure 3: Confusion matrices showing the prediction results of the random forest classifier, as estimated from cross-validation. Top shows the average confusion matrix from the eight cross-validation folds, with the predicted class shown on the x-axis and true class on the y-axis. Squares are colored by the number of observations in each. Text inside each true positive square indicates the accuracy of that class (i.e. snow was correctly classified 95% of the time, firn 59%, etc…). Bottom shows the same confusion matrix collapsed down to just the snow class and all others.

The US Geological Survey (USGS) collects seasonal and annual glaciological mass balance observations at three "Benchmark Glaciers" within the study area (U.S. Geological Survey Benchmark Glacier Program and others, 2016). Mass balance profiles are created from point observations of annual mass balance, and the ELA is calculated as the point at which the annual mass balance is zero. I used observations from these three glaciers (Wolverine Glacier, Gulkana Glacier, and Lemon Creek Glacier) to validate the accuracy of the remotely-sensed ELA results (Figure 4).

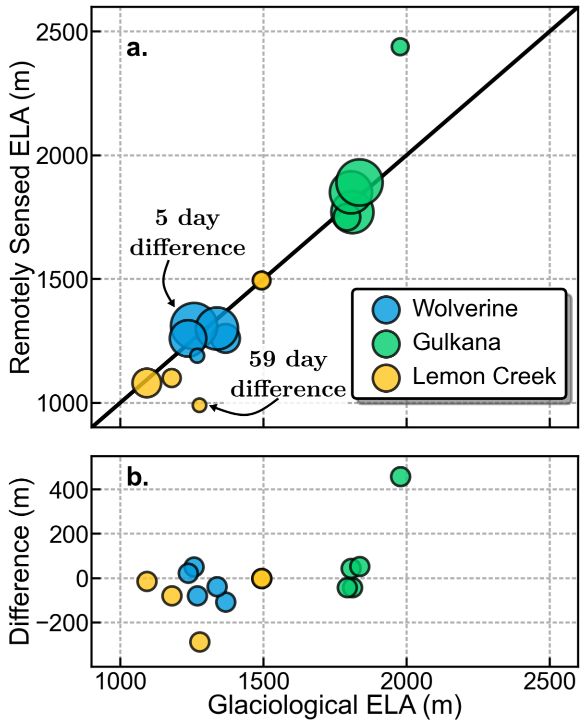

Figure 4: Comparison between glaciological ELAs and the derived ELAs (Remotely Sensed ELA) on three benchmark glaciers. (a) shows the ELAs derived from each plotted against each other, and (b) shows the magnitude of difference between the two (remotely-sensed minus in situ). Marker size in (a) indicates the number of days separating the observations, with smaller dots indicating larger time discrepancies (ranging from 5 days to 59 days). Note that there are two points for Lemon Creek at 1500 m, indicating two years in which the ELA was above the elevation range of the glacier in both the remotely-sensed and in situ datasets.

The mean absolute ELA error for all glaciers was 88 m (median absolute error of 44 m), with a mean bias of –4 m (median bias of –13 m). These errors were skewed by two outliers in the dataset on Gulkana and Lemon Creek glaciers. The outlier on Gulkana was caused by significant cloud cover which was misidentified as firn and ice, and the outlier on Lemon Creek was caused by no cloud-free imagery being available in the later summer months. Removing these outliers results in a mean absolute error of 44 m and bias of −18 m (indicating the remotely sensed ELAs were on average 18 m lower than the glaciological ELAs).

1.4.2. Spatial patterns

The automated methods resulted in physically realistic patterns of glacier ELAs and AARs at both the individual glacier and regional scale. A clear relationship between continentality (the glaciers' distance from the ocean) and ELAs was found, with glaciers with a geometric center nearer to the ocean having lower ELAs than more continental glaciers due to increased moisture availability and precipitation (Figure 5). For glaciers within 100 km of the ocean, each additional kilometer from the ocean leads to an increase in ELA of 8.6 m (with an intercept of 1027 m at the ocean). However for those glaciers further than 100 km from the ocean the trend is less clear.

The total accumulation area of all study glaciers is 31,334 km^2 (calculated form the five-year average products), with a corresponding AAR of 0.41. The AAR of individual subregions varies substantially across the study area, ranging from 0.26 (in the Aleutian Range) to 0.49 (in the Wrangell Mountains) (Figure 6, Table A2). The glaciers with the highest AARs tend to be large tidewater glaciers (e.g. Hubbard Glacier, Yahtse Glacier, Taku Glacier), while smaller glaciers on the periphery of their mountain ranges have the lowest AARs.

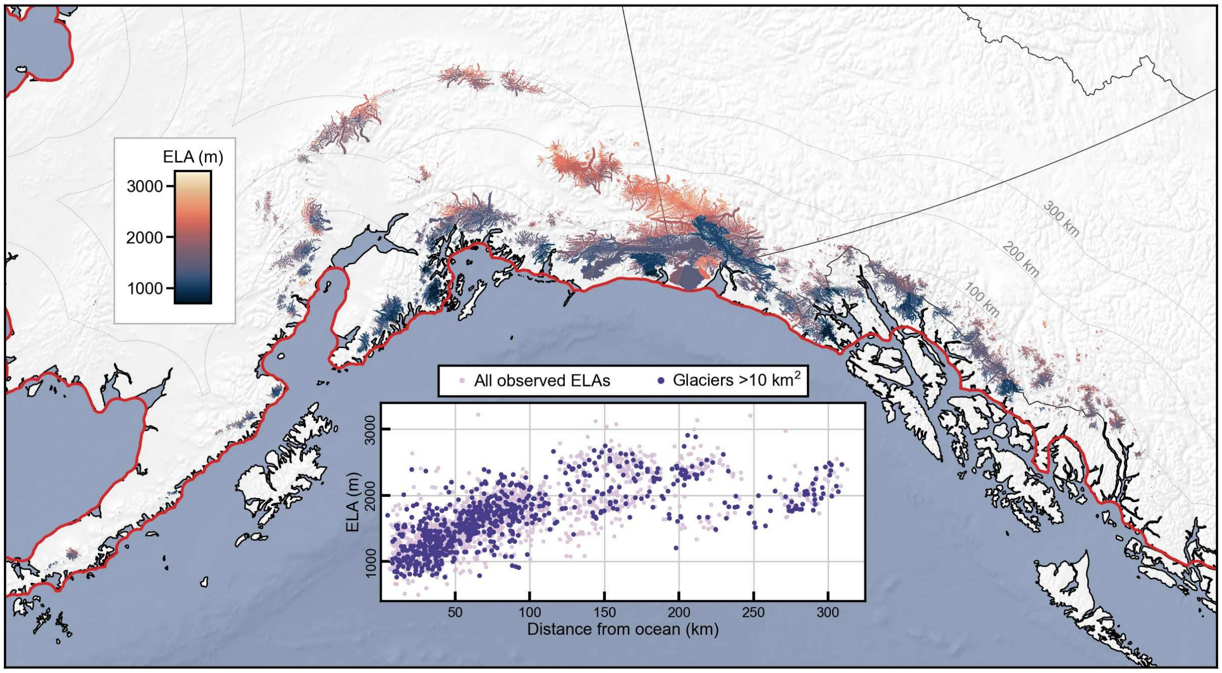

Figure 5: The ELA of each glacier (indicated by the color), as calculated from the five-year (2018–2022) average AA products. Inset scatterplot shows the relationship between distance-from-ocean and ELA. Light colored dots are all glaciers with observable ELAs, and darker purple dots are glaciers with observable ELAs that are larger than 10 km^2. Red line indicates the coastline that was used.

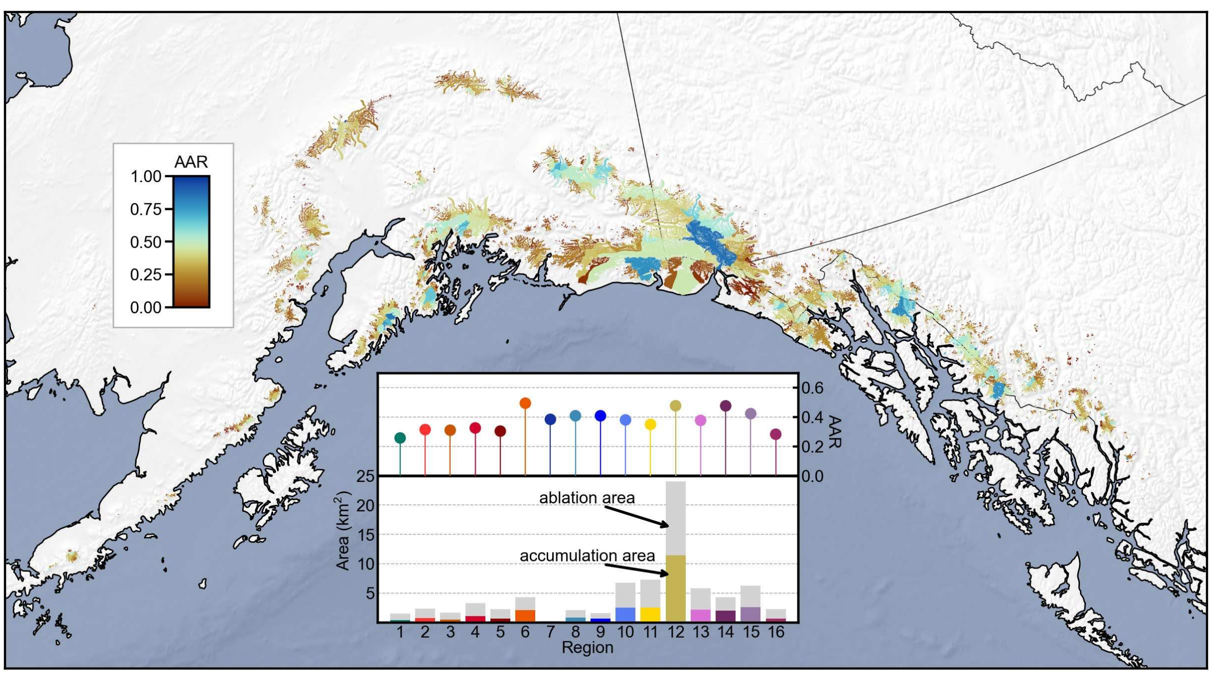

Figure 6: The AAR of each glacier (indicated by the color), as calculated from the five-year average AA products. Inset plots show the total accumulation and ablation area of each O3Region (bottom, left axis), as well as the total AAR (top, right axis), with numbers and colors corresponding to Figure 1.

Our observed AARs are well correlated with coincident observations of glacier elevation change (Figure 7). The average of the 2018 and 2019 AARs of each O3Region was compared to the average 2015–2019 elevation change rate from Hugonnet and others (2021). Regions with lower AARs (less accumulation area) exhibited greater elevation change (mass loss) than regions with higher AARs (R^2=0.54). I also note that regions with marine-terminating glaciers (regions 8–15) display greater surface elevation loss (i.e. greater mass loss) than other regions with similar AARs (Kochtitzky and others, 2022). This is explainable by the increased glacier mass loss from frontal ablation of these glaciers (a process which is not captured by variations in accumulation area) in addition to surface mass balance (the process which variations in accumulation area does capture). Region 13 seems to not fit this pattern as well (Figure 7), which may be attributable to the Glacier Bay tidewater glaciers undergoing rapid retreat in the early 20th century and now being more or less stable (McNabb and Hock, 2014).

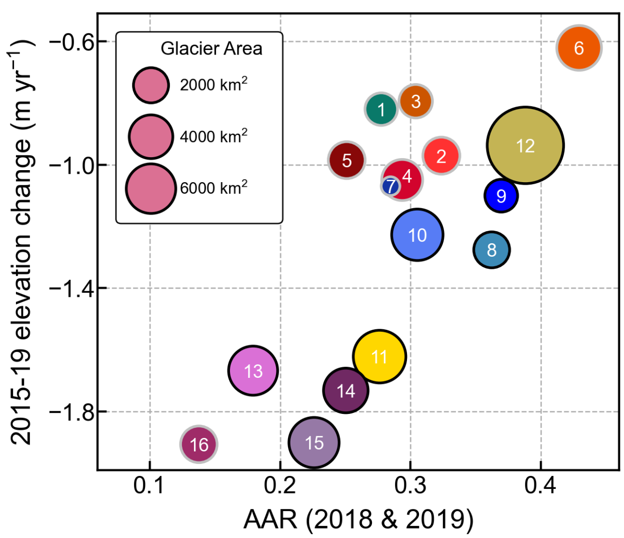

Figure 7: Comparison between average AAR for 2018 and 2019 and the 2015–2019 elevation change rate in each O3Region. Markers are colored and labeled according to Figure 1, with their size corresponding to the total glacier area in each. Points with black borders indicate regions that contain marine-terminating glaciers, while those with grey borders do not.

1.4.3. Temporal patterns

Substantial inter-annual variability in ELA was observed (Figure 8). The median difference between the maximum and minimum ELA of individual glaciers was 470 m (interquartile range of 330–650 m) across the five-year study period. The highest ELAs across the entire region were observed in 2019 with ELAs being 140 m higher than average across all glaciers, while the lowest ELAs were observed in 2021 at 90 m below the average. The particularly high ELAs in the North Coast Ranges in 2018 and 2019 match with observations on TAKU Glacier of ELAs which were 150 m higher than any other year of record (1948-2022), caused by exceptionally warm summer temperatures even at high elevations (Pelto, 2019). The range in observed ELAs resulted in substantial variability in AAR across the study region, with the median difference between the maximum and minimum glacier AAR being 0.46 (interquartile range of 0.30–0.62), with the most pronounced variability found in the North Coast Ranges (Figure 8, Table A3).

1.5. Discussion

1.5.1. Methodology limitations

The automated methodology that is presented here allows for annual glacier AARs and ELAs to be efficiently extracted across large regions at high spatial resolution. However, as with any approach that is applied at scale there are limitations. Although the five-day return interval for Sentinel-2 provides imagery at a higher frequency than Landsat missions, capturing the true end-of-summer snow cover distribution is still dependent on the availability of suitable cloud-free imagery prior to the date of maximum SLA. In particularly cloudy years, this can result in offsets of more than a month between the true glaciological mass balance minimum and the timing of the best available image (Figure 4).

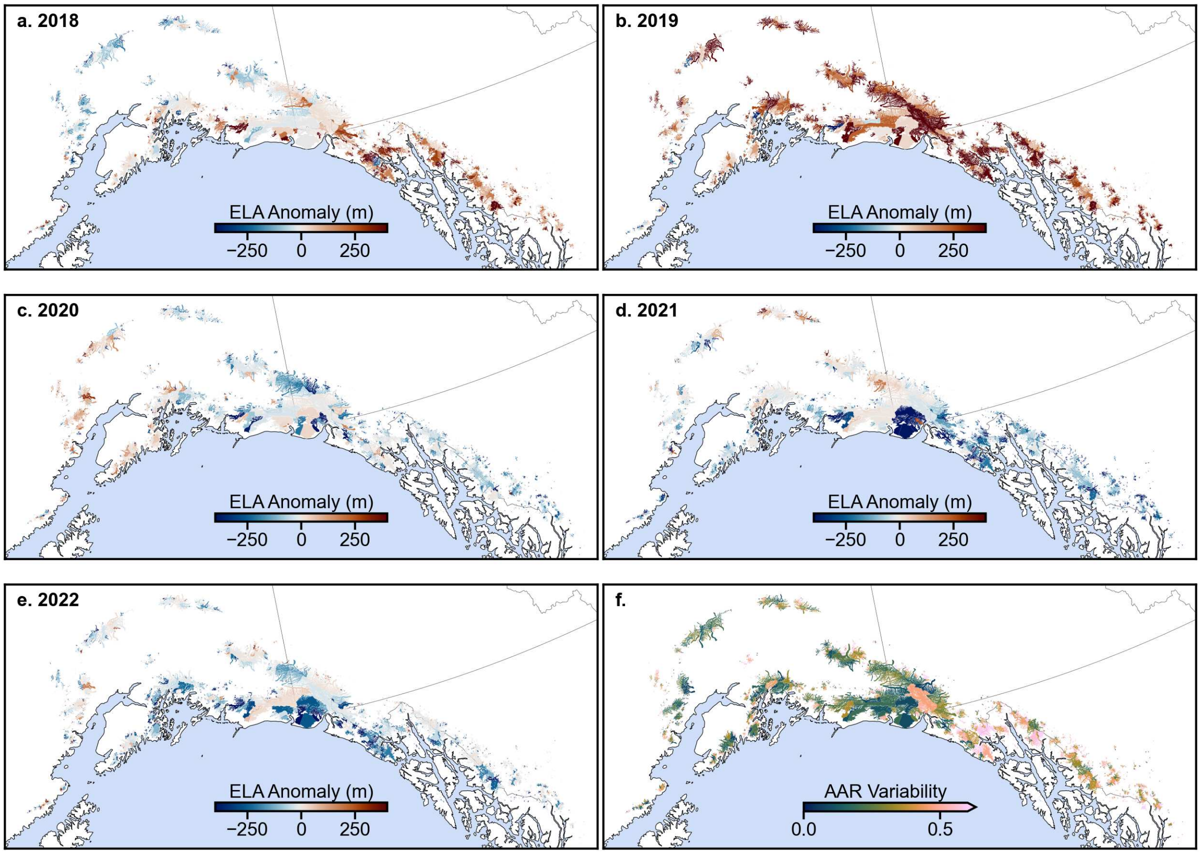

Figure 8: Interannual variability in the ELA of each glacier (a–e), presented as anomalies from each glacier's average ELA in Figure 5. Red colors indicate higher-than average ELAs, blue colors indicate lower-than average ELAs. (f) shows the variability in AAR for each glacier across the five years of observations.

The random forest classification approach which I implemented has high accuracy (Figure 3), but misclassification is still possible particularly in steeper terrain or when cloud cover is not properly identified. Areas with slopes greater than 25 degrees (largely ice falls and glacier headwalls) were masked out in the analysis to limit misclassification of these areas. In rare cases, this may make it impossible to identify the true ELA on glaciers if the ELA falls within the elevation range of an extensive ice fall because too large of an area is masked out. Other machine learning approaches that are able to incorporate the wider spatial context of imagery, such as a convolution neural network, might be capable of improving the glacier surface facies classification. However, such an approach would require a much larger training data set and be more computationally expensive.

Using the RGI glacier area dataset allows direct comparison between these findings and other studies, and facilitates the use of these AA, ELA, and AAR products in future studies. RGI outlines in the Alaska region are derived from satellite imagery primarily from 2004–2010, and glacier retreat in the intervening years means that non-glacierized areas are included in this analysis. This systematic over-estimation of glacier area causes the AARs to be smaller than if contemporaneous glacier extents were used, but the accumulation area and ELAs are not impacted. Roberts-Pierel and others (2022) analyzed glacier surface area changes over the majority (but not all) of the study region, and found that total glacier area in 2020 was ~94.5% of the 2006 glacier area (the approximate date of imagery from which the RGI glacier outlines were derived). This suggests that the modern-day AAR estimates which I present here may be over-estimated by ~5.5%, and the true modern region-wide AAR would be 0.43.

Lastly, climate reanalysis products and future climate projections in mountainous regions have inherent limitations due to the scarcity of in situ data and complex topography (Zandler and others, 2019). The end-of-century ELAs that I present here are meant to represent a reasonable estimate of future changes in these regions, rather than absolute projections of glacier-specific AAR and ELA changes.

1.5.2. Benchmark Glaciers and regional variability

One of the goals of the USGS Benchmark Glacier observations, and mass balance programs across the globe, is to provide detailed insight into the mass balances processes on the single glacier scale such that those observations can provide standards for comparison against other glaciers in the surrounding regions (Huss, 2012; O'Neel and others, 2019). The interannual variability in mass balance on benchmark glaciers is uniquely captured by seasonal in situ measurements, yet their geometry, location, or hypsometry can result in short-term and long-term benchmark glacier mass balance changes that are atypical of the wider regional changes (Fountain and others, 2009; Zemp and others, 2009).

The ELA and AAR products in this study provide an opportunity to investigate how well the interannual variability of site-specific benchmark glacier mass balance captures the wider regional mass balance by using the region's AAR as a proxy for its annual mass balance. To do so, I compare the annual mass balance of each of the three benchmark glaciers to the annual AAR of their surrounding regions (Figure 9). The annual balances at Lemon Creek are strongly correlated ($P<0.01$) with the AAR of the O2Region and O3Region, with r^2 values greater than 0.96 (Figure 9). The mass balance and regional AAR are less well correlated at Gulkana Glacier ($r^2=0.73$ and $P=0.07$ for the O3Region, $r^2=0.58$ and $P=0.13$ for the O2Region), while Wolverine Glacier is the least correlated ($r^2=0.33$ and 0.19, $P=0.32$ and 0.49).

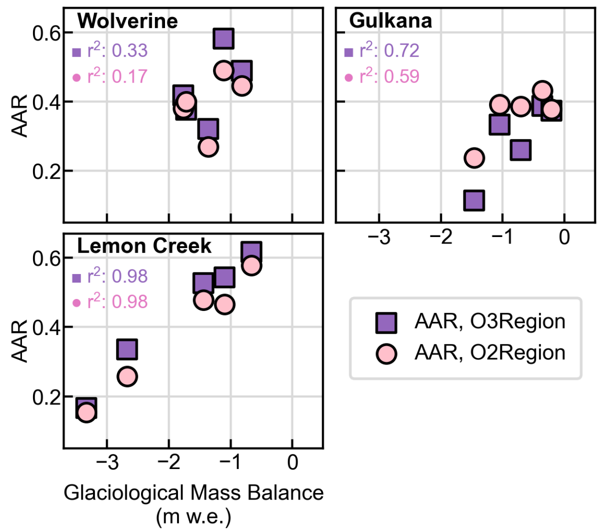

Figure 9: Relationship between glaciological mass balances of the three Benchmark Glaciers and the AAR of their O2Region (pink dots) and O3Region (purple squares), with each point representing a single year. r^2 values are shown for a linear regression of each. Higher r^2 values indicate that the benchmark glacier mass balance variations are more representative of the annual AAR variations of their surrounding regions.

The higher correlation that I find for Lemon Creek may be due to the larger range of annual balances (2.7 m w.e.) and AAR (0.45) for this glacier and region over the five years of observation, as compared to Wolverine (1.0 m w.e. and 0.26) and Gulkana (1.3 m w.e. and 0.27). Alternatively, it may be that there is greater intra-regional variability in mass balance in the regions surrounding Wolverine and Gulkana, or the five years may not provide a long enough temporal baseline for such an investigation.

1.5.3. Climate and ELAs

Winter precipitation and summer temperatures from ERA5-Land were used to investigate the climatic drivers of ELA variations at the regional scale (ELAs and climate variables were grouped by O3Region). Over the five-year study period, ELAs were found to be positively correlated ($P<0.01$) with summer temperatures (higher summer temperature led to higher ELAs) and negatively correlated ($P<0.01$) with winter precipitation (increased winter precipitation led to lower ELAs) (Figure 10). Across the entire Alaska region each 1 °C increase in summer temperature was associated with a 62 m increase in ELA, while each 10% increase in winter precipitation was associated with a 24 m decrease in ELA. However, these relationships were not consistent across the entire study area. Coastal regions (O3Regions 8–16) and interior regions (O3Regions 3–7) showed contrasting patterns (Figure 9). Winter precipitation was found to be a stronger predictor of ELA variability in coastal regions while the linear relationship between ELA and summer temperature was not statistically significant ($P=0.13$). Conversely, for the interior regions summer temperature was a stronger predictor of ELA while the linear relationship between ELA and winter precipitation was not statistically significant ($P=0.67$).

A multiple linear regression model, using winter precipitation and summer temperature, was fit to all subregions. This model (adjusted $R^2=0.46$) found that each 1 °C increase in summer temperature resulted in an ELA rise of 85 m, and each 10% increase in winter precipitation resulted in ELA lowering 32 m.

Changes in summer temperature and winter precipitation derived from CMIP-6 data were used to predict the magnitude of end-of-century ELA changes. A single model was used, rather than a region-specific or glacier-specific approach, because the goal was to investigate the realistic magnitude of ELA changes, rather than provide absolute predictions. A more robust approach might include climate projection downscaling or including multiple SSP scenarios, but is beyond the scope of this study.

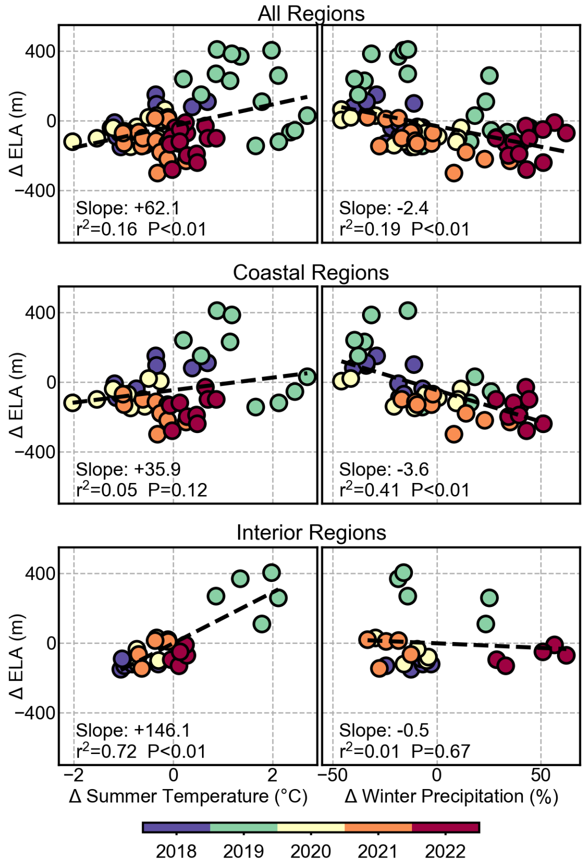

Figure 10: The relationship between climate and ELA variability across the study area. Y-axis on each subplots is the annual variability in ELA of each O3Region. X-axis of the left column is the ERA5-Land derived summer temperature (scaled as difference from mean), and the X-axis of the right column is the ERA5-Land derived winter precipitation (scaled by percent difference from mean). Points are colored according to the year which they represent. The top row includes all subregions in the study area. Middle row includes only the coastal subregions (8–16). Bottom row includes only the interior subregions (3–7).

The CMIP6 ensemble shows that summer temperature increases will range from +1.7 to +3.2 °C across the study region between the 2013-2022 and 2090-2099 periods. Winter precipitation is also projected to increase, ranging from +4% to +29% relative to modern precipitation. The resulting end-of-century projected ELA rise ranges from +86 to +249 meters relative to the present-day (Figure 11). The most extreme increases in ELA are projected to occur in the North Coast Ranges, due to the combination of the largest projected temperature increase and smallest increase in winter precipitation. These findings are similar to those of McGrath and others (2017) which utilized a similar approach but with a much smaller sample size of in situ observations. The regional AAR which I find in this study is substantially lower than the range of possible AARs which they considered when estimating modern glacier ELAs, highlighting the novelty and value which my glacier-specific observation of accumulation areas and ELAs provides.

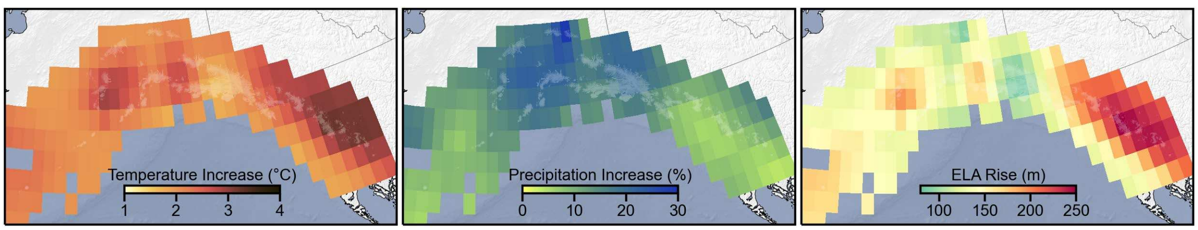

Figure 11: Changes in summer temperature (left) and winter precipitation (center) between 2013–2022 and 2090–2099 from a 13-member ensemble of CMIP6 global climate models under the "middle of the road" scenario SSP2-4.5. The resulting change in ELA, as calculated from the multilinear regression described above, is shown on the right.

The projected ELA increases presented here are increases in the long-term-average ELA. Individual years are likely to have more extreme changes (both positive and negative). The 2019 mass balance year highlights how anomalies of +300 m in some regions are realistic expectations for inter-annual ELA variability. Anomalies this large, on top of the projected increase in long-term average ELA, could result in individual melt seasons with ELAs 500+ meters above what are seen today, with corresponding significant glacier mass losses in those years.

1.5.4. Glacier disequilibrium and vulnerability

I modeled the future changes in accumulation area for a range of ELA increases using a hypsometric approach which accounts for glacier area altitude distribution (Figure 12). For each glacier, the modern ELA was incrementally increased and the resulting AA and AAR was calculated by assuming all surface area above the ELA would be in the accumulation zone and all surface area below the ELA would be in the ablation zone. The initial AAR conditions were calculated by applying the same hypsometric approach given the modern ELAs of each glacier, rather than using the average observed AAR, to remove the effects of snow cover below and exposed ice above the ELA. The ELA rise was calculated for each glacier by sampling the projected ELA rise shown in Figure 11 using each glacier's geometric center point (provided by the RGI "CenLon" and "CenLat").

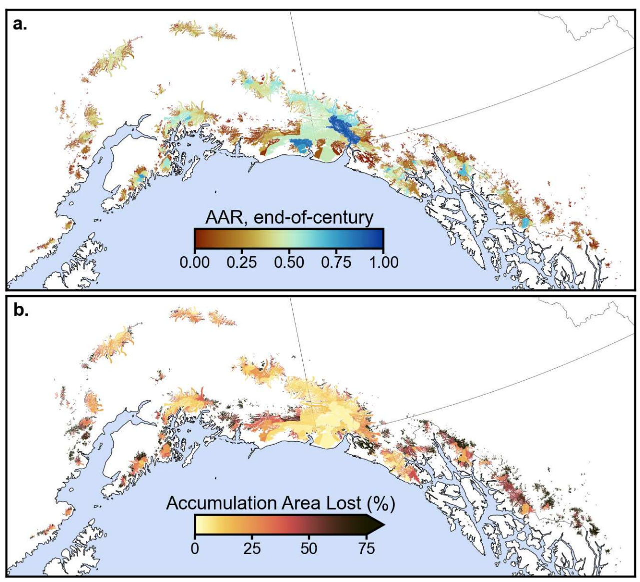

Figure 12: (a) The end-of-century AAR for each glacier calculated by applying the ELA rise in Figure 11 to modern-day ELAs. (b) The percent of the modern-day accumulation area which would be lost with the projected ELA rise.

Across the entire region, total accumulation area is projected to decrease to 75% of its modern extent by the end of the century, resulting in an AAR of 0.33 (compared to the modern hypsometric-derived AAR of 0.44) (Figure 12). Substantial differences are found between individual regions, ranging from 12% to 73% loss of the modern AA in the Eastern Chugach Mountains and Central Coast Mountains respectively (Table A2), which matches well with the patterns of end-of-century mass loss projected by Rounce and others (2023).

A substantial number of glaciers are already entirely within the ablation zone in the present day, which I define as not having an observable ELA or having an AAR of <10% in the five-year average products (Figure 13). A total of 1009 glaciers in this study currently lack an accumulation zone, with a cumulative surface area of over 6400 km^2 (8% of the studied area). Without an accumulation zone, these glaciers should be assumed to be entirely out of equilibrium with the modern climate and unable to persist in their present form (Pelto, 2010). Under the projected end-of-century scenario of ELA rise, this will increase to 1944 glaciers and 16500 km^2 (22% of the studied area). The majority of these glaciers are small and on the periphery of their mountain ranges (Figure 13). However, there are numerous large glaciers that are almost entirely ablation zone today or are likely to be by the end of the century; for example: Marvine/Hayden Glacier (445 km^2), the eastern tributary of Bering Glacier (534 km^2), Tana Glacier (515 km^2), Miles Glacier (420 km^2), and the glaciers within the Yakutat Icefield (>1000 km^2).

The end-of-century decreases in AAR will push glaciers even further out of equilibrium with climate than they are in the modern day. The present-day regional AAR of 0.41 is well below the range of values that would be needed for glaciers larger than 1 km^2 to be at equilibrium with climate (0.54–0.64) (Kern and László, 2010). Combining this range of AARs with the modern accumulation area of 31000 km^2 would suggest that the present-day accumulation area is capable of sustaining 49000–58000 km^2 of total glacierized area, substantially less than the RGI-defined glacier extent of 76000 km^2 of these study glaciers. Under the projected end-of-century ELA rise scenario the total sustainable glacier area drops to 39000–46000 km^2, suggesting a potential loss of up to 49% of the current glacier surface area.

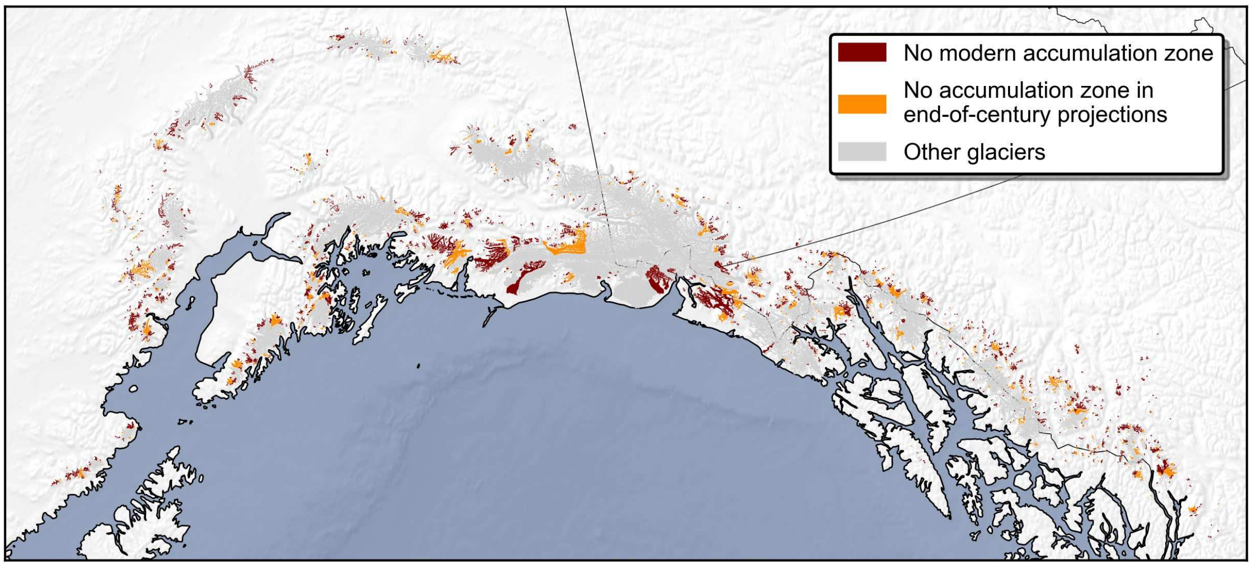

Figure 13: Identification of glaciers with no modern (2018–2022) accumulation area. Red indicates glaciers with no modern accumulation area. Orange indicates glaciers that would lose their accumulation area with the projected end-of-century ELA rise.

These projections of area change are in line with the most drastic scenarios considered by McGrath and others (2017) over these same glaciers (a 225 m increase in ELA under the RCP 8.5 climate projection), despite using less extreme climate forcings. This is due to the differences in the initial AAR and ELA values used in each study while using the same glacier geometry. McGrath and others (2017) assumed that glaciers are near equilibrium with modern climate (using AARs ranging from 0.5-0.75) in order to derive glacier-specific ELAs. In contrast, my projections of glacier area change include the committed area loss due to modern-day disequilibrium, highlighting the value of our glacier-specific observations to provide validation and to constrain model initialization in future studies.

These projected glacier area losses will not occur immediately, but rather will take decades to be realized, with this response time controlled largely by glacier geometry. Furthermore, the modeled declines in AAR are based only on modern-day surface elevations and glacier area, and do not account for future glacier surface elevation changes or surface area changes. In reality, the altitude-mass-balance feedback will increase the glacier surface area below the ELA and amplify the magnitude of glacier area loss, while the reduced glacier area will diminish AAR losses (Huss and others, 2012; Trüssel and others, 2013; Sass and others, 2017).

1.6. Conclusions

In this study I presented a detailed investigation of the modern and future state of glacier accumulation areas and equilibrium line altitudes for over 3000 glaciers which account for 88% of the glacier cover in the Alaska region. The automated methods which I developed using Sentinel-2 imagery could be applied in future year and to other glacier regions. Furthermore, the derived products have potential uses in applications beyond what is presented here, such as for validating and constraining glacier models, to understand spatial variability in snow accumulation and ablation across a range of spatial and temporal scales, and as a supplement to in situ and geodetic products.

I found that the total accumulation area ratio of these glaciers is 0.41, with an inter-annual range of 0.25–0.49. The observed AAR is substantially smaller than the steady-state AAR of 0.54–0.64, indicating that, on a regional scale, glaciers are out of equilibrium with modern climate. Furthermore, more than 1000 glaciers were found to have effectively no modern accumulation area. I observed substantial year-to-year variations in ELA and AAR, with an average glacier-specific ELA range of 470 meters and AAR range of 0.46 across the five years.

I found that the temporal variability in ELAs can be explained by inter-annual climate variability. Summer temperatures and winter precipitation derived from ERA5-Land were found to be good predictors of regional-scale ELA variability, with winter precipitation being a stronger predictor of ELAs in coastal regions while summer temperatures were more important for continental regions. An analysis of future climate projections indicated that ELAs will rise by an average of ~170 m (ranging from 85–250 m) under a middle-of-the-road greenhouse gas emission scenario, with the largest changes expected in the North Coast Ranges. I investigated the vulnerability of modern glaciers to these changes, and found that the projected ELA rise would result in a loss of 25% of the modern-day glacier accumulation area, while 1938 of the studied glaciers (22% of the investigated area) would be left with no functional accumulation area. In order to reach a new equilibrium with the projected end-of-century climate, up to 49% of the modern glacier surface area may be lost.

1.7. Data availability

The derived snow cover products and metrics are publicly available at https://doi.org/10.5066/P1QHST6F (Zeller and others, 2024c). USGS Benchmark Glacier data are available at https://doi.org/10.5066/F7HD7SRF (U.S. Geological Survey Benchmark Glacier Program and others, 2016). Glacier elevation change products are available at https://doi.org/10.6096/13 (Hugonnet and others, 2021). All Sentinel-2 imagery, ERA5-Land reanalysis products, CMIP6 climate projections, and the Copernicus WorldDEM-30 are available and were accessed via the Google Earth Engine Data Catalog at https://developers.google.com/earth-engine/datasets/catalog. All code developed for this study is available through a public GitHub repository: https://github.com/lucas-zeller/Glacier-Snow-Lines.

CHAPTER 2: SEASONAL TO DECADAL DYNAMICS OF SUPRAGLACIAL LAKES ON DEBRIS-COVERED GLACIERS IN THE KHUMBU REGION, NEPAL[2]

2.1. Introduction

The processes controlling the response of debris-covered glaciers (DCGs) to changing climatic conditions are distinct from those of clean-ice glaciers and tend to be less well studied and understood (Brun and others, 2019, 201; Miles and others, 2020). Supraglacial lakes (SGLs) on DCGs can increase ablation rates through increased radiation absorption, ice cliff calving, and efficient transfer of heat to the englacial and subglacial environments (Miles and others, 2022). Further, rapid drainage of these lakes presents a potential hazard to downstream communities and infrastructure (Rounce and others, 2017; Miles and others, 2018), particularly in cases where smaller ponds coalesce into large terminal lakes capable of causing catastrophic glacier lake outburst floods (Watanabe and others, 2009).

Understanding the evolution of SGLs on DCGs has been limited by difficulties associated with directly observing these features (Racoviteanu and others, 2022). The rugged topography

[2] Chapter 2 has been published as: Zeller L, McGrath D, McCoy SW and Jacquet J (2024) Seasonal to decadal dynamics of supraglacial lakes on debris-covered glaciers in the Khumbu region, Nepal. The Cryosphere 18(2), 525–541. doi:10.5194/tc-18-525-2024

of DCGs generally limits the scope of in situ investigations to single lakes and/or individual glaciers. Remote-sensing approaches to studying the glacier-wide spatial and temporal patterns in lake evolution have been limited by (1) the spatial resolution of freely available satellite imagery (e.g., Landsat and Sentinel-2) being large relative to the size of many SGLs and (2) the infrequent revisit period of satellites acquiring higher-spatial-resolution imagery preventing detailed assessment of the rapid temporal evolution of these lakes.

Previous studies have found that SGLs tend to form in areas with low surface gradients and low glacier flow velocities (Reynolds, 2000). The temporal stability of individual lakes can vary widely, with some appearing stable on decadal scales, while others fill and drain annually, semi-annually, or seemingly randomly (Narama and others, 2017; Steiner and others, 2019). Seasonal to annual patterns in lake development have been observed, with links to ice velocity variations, water availability from precipitation and snow/ice melt, and the opening or collapsing of englacial conduits (Benn and others, 2001; Mertes and others, 2017; Watson, Quincey, and others, 2018).

There are few existing studies which have investigated the seasonal variations in SGL lake areas on DCGs on glacier-wide scales. These studies have generally relied on coarser-resolution Landsat imagery aggregated over decadal time periods (Miles and others, 2017; Narama and others, 2017) or have used a sensor integration approach with both optical and synthetic aperture radar (SAR) datasets (Wendleder and others, 2021). Further, the majority of these studies (including ours) have focused on DCGs in High Mountain Asia and particularly in regions of the Himalayas and the Karakoram which are impacted by the Indian summer monsoon.

These studies find that SGLs generally form in the early spring from the accumulation of rain and meltwater, grow in size through the pre-monsoon season (1 March–15 June), and then drain during the monsoon season (15 June–30 September). The frequent snow cover and frozen surfaces tend to make lake identification difficult during the winter, but SGLs are generally assumed to be stable or very slowly drain throughout the post-monsoon (1 October–30 November) and winter (1 December–28 February) months (Miles and others, 2017; Watson, Quincey, and others, 2018).

Despite these patterns in SGL area and drainage that have been observed over seasonal timescales, the majority of studies investigating SGL development on decadal timescales have not explicitly accounted for seasonality in lake areas (Watson and others, 2016; Steiner and others, 2019; Mohanty and Maiti, 2021). Rather, these studies tend to utilize a series of individual higher-resolution images that cover a wide range of years but are captured at irregular seasonal timing. Improving our understanding of the dynamics of short-term SGL variability would allow us to differentiate between the confounding effects of seasonal and long-term trends in SGL area. Therefore, the goal of this study is to develop consistent observations of SGL evolution over daily to decadal timescales on eight glaciers in the Khumbu region of Nepal through the integration of PlanetScope satellite imagery (Planet Team, 2017), Sentinel-2 and Landsat 5–9 imagery, and in situ field observations.

2.2. Study Area

I investigated SGL dynamics on eight glaciers in the Khumbu region of Nepal (Figure 14; Table B1). The glaciers in this region are characterized by ablation zones which have nearly continuous debris cover, slow ice flow velocities ($< 10\,\mathrm{m\,yr^{-1}}$) (Gardner and others, 2022), and low-gradient surface slopes ($<$ 5 degrees). Debris-covered areas range in elevation from 4800–5300 m, with debris thickness tending to increase towards the glacier termini (Rounce and others, 2021). Five of the glaciers in this study have a southerly aspect and flow direction, two (Ambulapcha and Ama Dablam) flow north, and one (Imja) flows westward (Figure 14). Lhotse Shar and Imja flow into the rapidly expanding Imja Tsho, resulting in increased ice flow velocities compared to the other glaciers in this study (Watanabe and others, 2009).

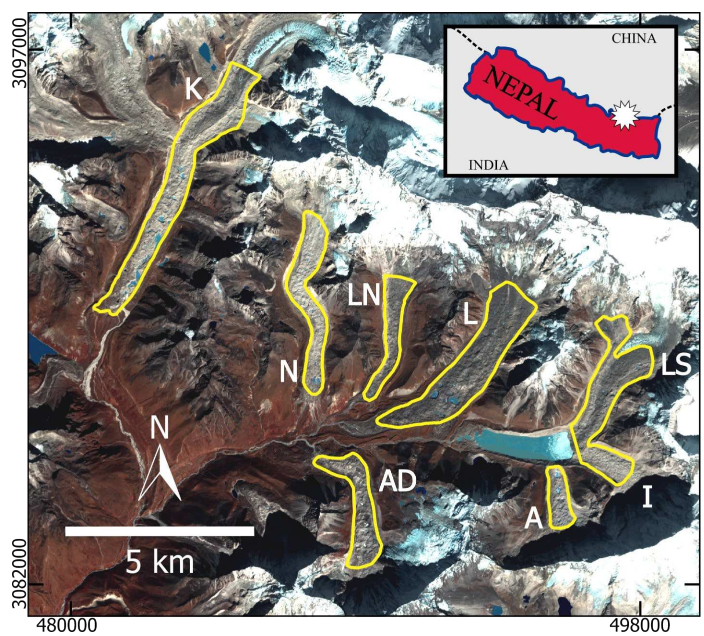

Figure 14: Sentinel-2 satellite image (13 November 2020) of the study area. The debris-covered areas of the eight glaciers are outlined in yellow. Letters adjacent to each glacier are shortened names (K=Khumbu, N=Nuptse, LN=Lhotse Nup, L=Lhotse, LS=Lhotse Shar, I=Imja, A=Ambulapcha, AD=Ama Dablam). Inset map shows the region's location within Nepal (indicated by the white star). The coordinate frame indicates the Easting/Northing range of the figure within UTM Zone 45N.

The climate in the Khumbu region is characterized by monsoonal summer seasons, during which the majority of the 587 ± 34 mm of annual precipitation falls, and cold and dry winter seasons (Perry and others, 2020). The limited winter precipitation leads to non-continuous snow cover on the study glaciers' surfaces throughout the winter; however, cold air temperatures regularly result in frozen lake surfaces, particularly in the February–April time period.

2.3. Methods

In this study, I investigated the patterns of SGL development on timescales ranging from subseasonal to decadal. I achieved this by integrating multiple satellite remote-sensing imagery sources. Each source provides unique observations, while together they build upon each other to inform us on their relative strengths and limitations. My methodology is broadly broken into a two-step process built around identifying SGLs in PlanetScope, Landsat, and Sentinel-2 imagery. I first developed a robust approach to delineating SGLs in high-temporal-resolution time series of PlanetScope imagery. From this dataset, I investigated the seasonal patterns in SGL variations over the 2017–2022 time period. I then used these high-spatial-resolution observations (3 m spatial resolution) as a validation dataset to optimize SGL identification in coarser-resolution Landsat and Sentinel-2 imagery, allowing us to investigate the decadal-scale trends in SGL evolution at coarser spatial scale (10 and 30 m). Direct field observations and uncrewed aerial system (UAS) surveys from May 2023 provided additional insight into the local-scale topography of these glaciers.

The use of high-resolution PlanetScope imagery allowed us to identify supraglacial streams and very small lakes which may be more appropriately referred to as “ponds”. There is no clear consensus in previous literature on the differentiation between terming a supraglacial feature a “lake” versus a “pond”, and without in situ observations it is difficult to differentiate between a supraglacial “stream” which is flowing and stagnant ponded water. Therefore, in this paper I use the term “supraglacial lake” (SGL) to refer to any supraglacial hydrologic feature which I identify from satellite imagery.

The area of investigation (AOI) was limited to the debris-covered tongue of each glacier. These outlines were created by manually adjusting the glacier extents from the Randolph Glacier Inventory Version 6.0 (RGI Consortium, 2017) to better match glacier margins in high-resolution satellite imagery in Google Earth Pro (sourced from Maxar imagery). Areas of exposed glacier ice were also manually excluded, as they were frequently misclassified as water. For this analysis, I separated Lhotse Shar and Imja into two glaciers, although they are classified as a single glacier in the Randolph Glacier Inventory Version 6.0. The outlines used for these two glaciers excluded the rapidly expanding terminal lake Imja Tsho for the entire time period, as the focus of this study was solely on SGLs.

2.3.1. SGL identification: Planet

I developed a semi-automated workflow to identify lakes on DCGs in PlanetScope images (Figure 15). Images of the study area from the October 2017 to April 2022 time period were searched for and downloaded using the Planet Orders API (Planet Team, 2017). Areas of cloud cover and terrain shadows were identified in each image and excluded from future analysis. See the Supplement for additional information on these steps.

SGLs were identified by separately classifying water and frozen lakes and then applying a pixel-wise temporal smoothing algorithm to ensure a consistent evolution of the glacier surface. An initial classification of water (Figure 15b) was performed by using a spatially varying threshold on the normalized difference water index (NDWI) (Gao, 1996), calculated using the reflectances in the green and near-infrared (NIR) bands.

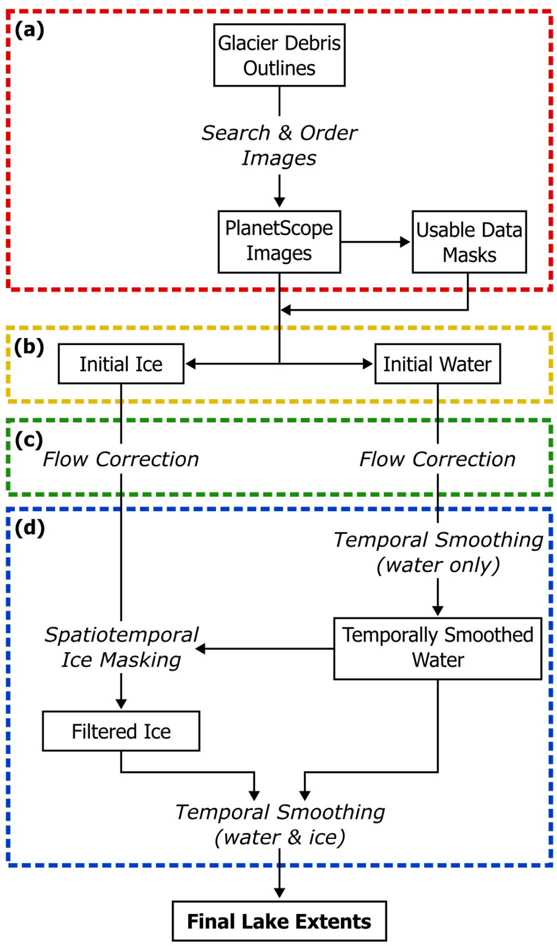

Figure 15: Workflow diagram for delineating supraglacial lakes in PlanetScope imagery. The boxed items indicate intermediate products in the workflow, while unboxed, italicized labels indicate processing steps which are referred to in the text.

Each pixel was then classified as water if its NDWI was at least 0.10 greater than the mean NDWI of surrounding pixels within 150 m (not including off-glacier areas, cloud cover, and terrain shadows) and with a minimum NDWI threshold of -0.15 (these thresholds were empirically determined). A final shadow-masking step was also applied at this point, with pixels with average surface reflectance across visible (RGB) bands less than 0.02 excluded from being classified as water.

An initial classification of frozen lake surfaces (Figure 15b) was performed using a similar spatially varying threshold on the NIR band. Each pixel was classified as frozen water (ice) if the NIR digital number was at least 1000 greater than the mean NIR of surrounding pixels within 150 m (not including off-glacier areas, cloud cover, and terrain shadows). In simple terms, areas of relatively high NDWI were initially classified as water, while areas of relatively high brightness in the NIR band were initially classified as lake ice. This initial ice classification does not differentiate between lake ice, glacier ice, and snow; however, I took precautions to avoid including glacier ice and snow in the final products. The study extent was delineated to purposefully exclude areas of the glaciers that were not completely debris-covered, reducing the possibility of glacier ice being misclassified as lake ice. Images with widespread snow cover were excluded. Additionally, in later steps I only allowed areas which were recently classified as water to be classified as frozen lakes, limiting the effects of mistakenly identifying snow drifts or exposed ice cliffs as SGLs. An ice flow correction was applied to each initial water and lake ice classification image to align them to a common date of 1 January 2020 (Figure 15c). This removes the effects of lake advection due to ice flow and allows multi-year tracking of individual lakes. Glacier flow velocities were taken from 1985–2022 composite ITS_LIVE velocity mosaics (Gardner and others, 2022) resampled to PlanetScope resolution.

Following initial lake identification, a series of filtering and smoothing approaches were applied to ensure a consistent temporal evolution of SGLs in these products and reduce noise caused by variable image quality, occasional snow and cloud cover, and inconsistent spectral response. See the Supplement for additional information on these steps.

2.3.2. SGL identification: Landsat and Sentinel-2

The Planet-derived SGL products were used as a training dataset for developing an optimized SGL identification approach for Landsat and Sentinel-2 imagery in this study area. All Landsat 5, 7, 8, and 9 and Sentinel-2 surface reflectance imagery, spanning the years 1988–2022, was downloaded from Google Earth Engine ($n = 1230$ per glacier). The same debris-covered AOIs were used for all images to facilitate a direct comparison between all satellite sources and across the entire 35-year time frame. Each image of each glacier was manually checked, and images with significant cloud cover, snow cover, or shadows over the majority of the glacier were discarded, resulting in an average of 940 images remaining for each glacier (Table B2). Shadowed areas in each image were masked using the Google Earth Engine ee.Terrain.hillShadow() function applied to the NASA Digital Elevation Model (NASADEM) (NASA JPL, 2020) with image-specific sun azimuth and elevation as input. Additional remaining shadows were removed by thresholding on surface reflectance values in the green band (using empirically determined values of 0.08 for Landsat images and 0.11 for Sentinel-2).

Persistent exposed glacier ice, which was frequently present in older Landsat imagery and misidentified as water, was masked as described in the Supplement.

2.3.2.1. Validation dataset creation

All Landsat 7, Landsat 8, and Sentinel-2 images with coincident Planet-derived lake extents were identified to be used as a training dataset. I defined suitable images as those which had at least three Planet-derived observations within the 9-day period centered on the Landsat/Sentinel-2 image date. For each of these training images, I resampled the corresponding Planet-derived lake extents to give a 30 m (Landsat) or 10 m (Sentinel-2) resolution product that indicated the percent of water cover within each Sentinel-2/Landsat pixel (Figure 16). For lake identification in Landsat and Sentinel-2 imagery, I focused on only unfrozen lakes, rather than also attempting to identify frozen lake surfaces as I did in PlanetScope imagery. Thus, the Planet-derived products used for the training dataset include only the lakes identified without employing the frozen lake identification (i.e., I used the temporally smoothed water product in Figure 15d).

2.3.2.2. NDWI optimization and lake identification

Using the Planet-derived training dataset, I identified the optimal NDWI threshold (calculated after scaling images to surface reflectance) to use for binary classification of SGLs in Landsat and Sentinel-2 imagery (Watson, King, and others, 2018). For each sensor (Landsat 7, Landsat 8, and Sentinel-2) a single NDWI threshold was identified that minimized the difference between Planet-derived and Landsat/Sentinel-derived total lake area across the entire training dataset. There were no Landsat 5 images in the training dataset because the Landsat 5 mission ended in 2012. Landsat 9 images were included in the analysis, but there were insufficient images overlapping the PlanetScope validation dataset to reliably constrain an optimized NDWI threshold. Thus, the same NDWI threshold for Landsat 7 was used for Landsat 5 images, and the same threshold for Landsat 8 and 9, because the sensor band wavelength ranges are identical.

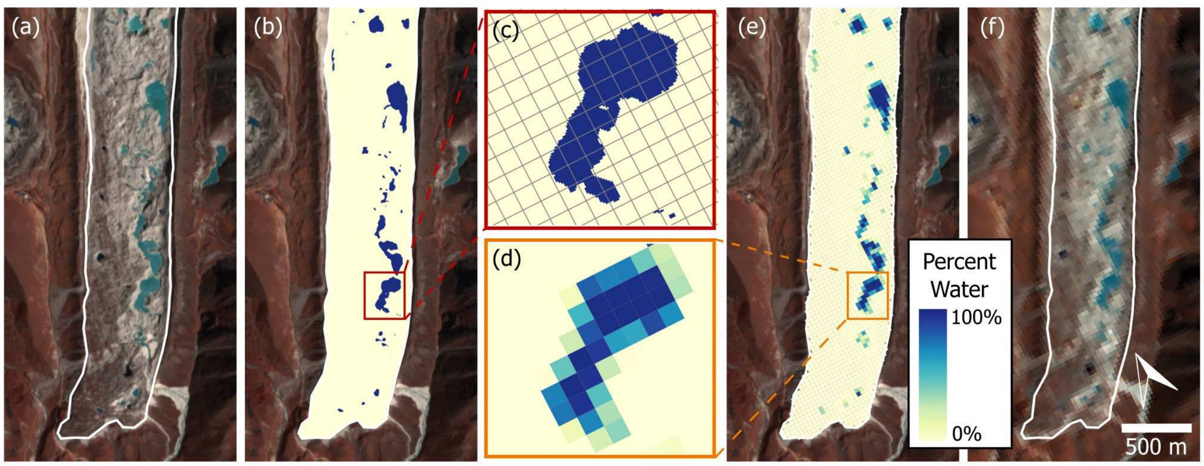

Figure 16: An example of the process of creating a Landsat-scale training dataset from Planet-derived lake extents. (a) shows an example PlanetScope image of the terminus of Khumbu Glacier on 24 October 2018, with the glacier extent outlined in black. (b) shows the lake extents in blue, from the automated PlanetScope workflow. (c) shows the Landsat pixel grid overlaid on the lake extents, for a subset of the glacier area. (d) shows the same area, resampled to Landsat pixel size and grid, colored by the percent of water cover within each pixel. (e) shows the full terminus area, resampled to the Landsat grid, colored by percent water coverage. (f) is a Landsat image from the same date (24 October 2018).

These optimized NDWI thresholds (Table 1) were then used to identify SGLs on the glacier surfaces across all available imagery after removing shadowed areas and exposed glacier ice. No additional smoothing was applied to these products, due to the limited temporal resolution compared to PlanetScope imagery.

2.3.3. Field observations

A field campaign was undertaken in May 2023 to collect in situ and drone-based observations of the study area. Perspective drone flights were flown on five glaciers (Lhotse Shar, Imja, Ambulapcha, Lhotse, and Lhotse Nup) to capture high-resolution videos and photos of the debris-covered surfaces using a DJI Mavic 2 Pro and DJI Mavic Air 2S. Additionally, grid surveys were flown near the termini of the Ambulapcha, Lhotse Nup, and Khumbu glaciers to create high-resolution structure from motion (SfM) and multi-view stereo (MVS) digital elevation models (DEMs) and orthomosaics. Grid surveys were flown ~60–90 m above ground level, with nadir camera positioning and at least 70 % overlap between images. SfM processing was completed in Agisoft Metashape. Ground control points (GCPs) were placed and surveyed for all three grid surveys; however, there were no nearby operational base stations to use for post-processing of these points, so they were not used in model creation. Thus, model generation was based on UAV GPS locations. The model creation resulted in DEMs with 0.08 m pixel spacing and orthomosaics with 0.04 m pixel spacing.

2.4. Validation

A validation set for the Planet-derived lake extents was created by manually delineating SGLs in a total of 28 PlanetScope images of the Lhotse, Nuptse, and Ambulapcha glaciers (Figure B1:). For each glacier, a series of cloud-free images spanning a range of approximately 1 year were selected, in order to capture the full annual cycle of SGL expansion and drainage. I used a ± 1 pixel (3 m) buffer for error estimation of these manual delineations (Gardelle and others, 2011). Further, the total SGL area on seven glaciers which were manually mapped by Watson and others (2016) was compared to my results from concurrent months. While there is no overlap in the years investigated between this study and theirs (the latest imagery used in Watson and others (2016), was from 2015), it provides a valuable constraint on the expected magnitude of SGL area.

2.5. Results

2.5.1. Lake delineation accuracy

2.5.1.1. Planet

The Planet-derived SGL extents resulted in physically realistic, accurate delineations of SGLs at high spatiotemporal resolution (Figure 17, Figure 21). The mean absolute error in total SGL area was $0.039\,km^2$ for Lhotse Glacier, $0.018\,km^2$ for Nuptse Glacier, and $0.004\,km^2$ for Ambulapcha Glacier. These are equal to errors of 0.8 %, 0.7 %, and 0.4 % of the total debris-covered area (from my AOIs) of each glacier, respectively (25 %, 33 %, and 13 % of the total lake-covered area). During the months with highest temporal density of suitable imagery (September–February), these errors are significantly lower (0.2 %, 0.4 %, and 0.3 % of the debris-covered area and 7.6 %, 19.1 %, and 8.3 % of the lake-covered area, respectively). A direct comparison between these products and those from Watson and others (2016), who derived SGL areas on these glaciers from high-resolution imagery over the 2000–2015 time period, is not possible, because there is no overlap in the observational years. However, my automated SGL areas from similar annual timing showed good agreement with theirs (Figure B1), with the majority of their results falling within the inter-annual range of my values (average difference of 17.3 % when discounting Imja and Lhotse Shar). The differences on Imja Glacier and Lhotse Shar Glacier (where I found smaller lake areas compared to Watson and others, (2016)) may be attributed to changes in subglacial hydrology as the proglacial lake Imja Tsho expands (Bolch and others, 2008).

2.5.1.2. Landsat and Sentinel-2

The optimized NDWI thresholds for lake identification were found to be 0.137 for Landsat 5 and 7, 0.188 for Landsat 8 and 9, and 0.250 for Sentinel-2 images (Table 1, Figure 18). The optimized value for Sentinel-2 is similar to the value found by Watson and others (2018a) of 0.22. The optimized value they found for Landsat 8 is not directly comparable to my results because they used the modified NDWI (Xu, 2006) which uses a short wave infrared band in place of the near-infrared band when calculating NDWI.

The median per-image glacier-wide error in SGL area, compared to the coincident Planet-derived lake area, was 37 % for Landsat and 34 % for Sentinel-2 (presented as a percentage of Planet-derived lake area), with values for individual glaciers ranging from 19 % (Lhotse) to 100 % (Imja) and 13 % (Ambulapcha) to 60 % (Imja), respectively (Table B3).

Table 1: The optimized NDWI threshold that was found for each Landsat and Sentinel-2 sensor.

Satellite	Optimized NDWI
Landsat 5 & 7	**0.137**
Landsat 8 & 9	**0.188**
Sentinel-2	**0.250**

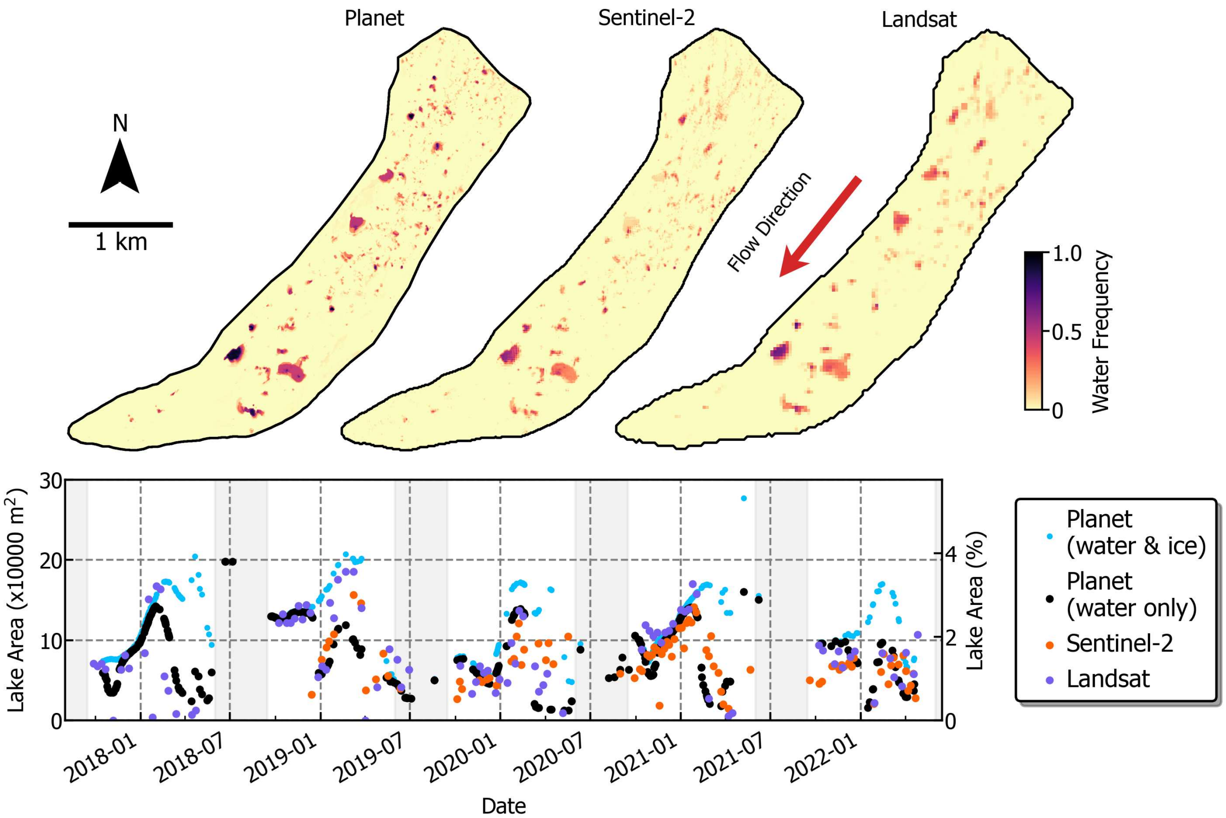

Figure 17: A comparison between the SGL extents and frequency in Planet, Sentinel-2 and Landsat imagery on Lhotse Glacier. The colorscale corresponds to the frequency each pixel was classified as water, with darker colors being more frequent. Only Landsat images from the 2018-2022 time period were used, to provide a more direct comparison with Planet and Sentinel-2. The time series plot shows the trend in total lake area for each sensor. Each point represents water identified in a single image. Planet-derived lake areas are shown for both the full methodology which includes frozen lake area (cyan) and the area if frozen lake area is excluded (black).

2.5.2. Short-term dynamics

2.5.2.1. Seasonality in glacier-wide lake area

A pronounced seasonal cycle in total SGL area was found in the Planet-derived lake datasets (Figure 19, Figure B1). On most glaciers, the maximum glacier-wide SGL area (both frozen and open water) occurred in March (during the pre-monsoon season), decreased throughout the monsoon with a minimum area occurring in September, and then increased steadily throughout the post-monsoon and winter months (October–February) (Figure 19). For each glacier, the annual maximum SGL area is approximately twice the annual minimum (Table B4–Table B8), highlighting the magnitude of short-term variability these features can exhibit. While this cycle is most clearly seen in the high-temporal-resolution Planet-derived dataset, it is also apparent in Sentinel-2 and Landsat-derived time series, although frequent lake surface freezing in winter months (which was not classified in Landsat/Sentinel-2) obscures this trend in many years (Figure 17).

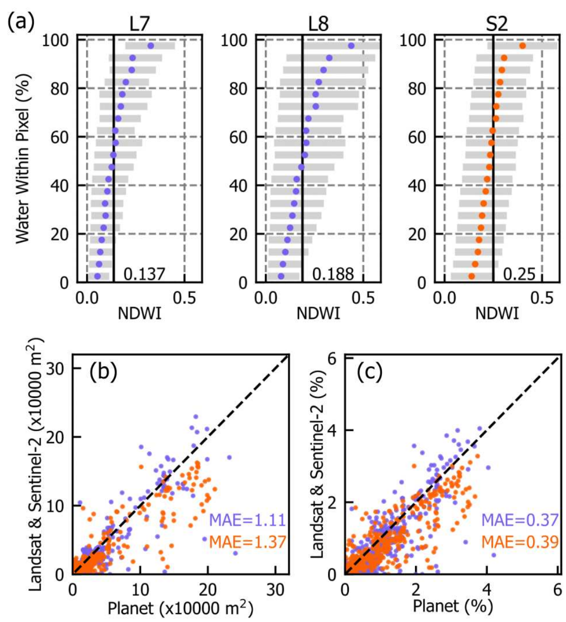

Figure 18: (a) NDWI optimization results for each satellite. Each horizontal bar shows the range of NDWI values for Landsat and Sentinel-2 pixels in the validation dataset with the indicated percent water cover (aggregated in 5% bins). Dots indicate the mean, grey bars show the range containing 90% of all observations. Vertical lines and the shown number indicate the optimized NDWI value for each sensor, which minimized the net error over the validation dataset. (b) and (c) compare the SGL area identified in PlanetScope imagery and in Landsat/Sentienel-2 coincident imagery using the optimized thresholds, with each point representing a single image. (b) shows these values as the total lake area, while (c) scales them by the total glacier debris-covered area. Mean absolute error (MAE) is shown for Landsat (purple) and Sentinel-2 (orange) results on each plot.

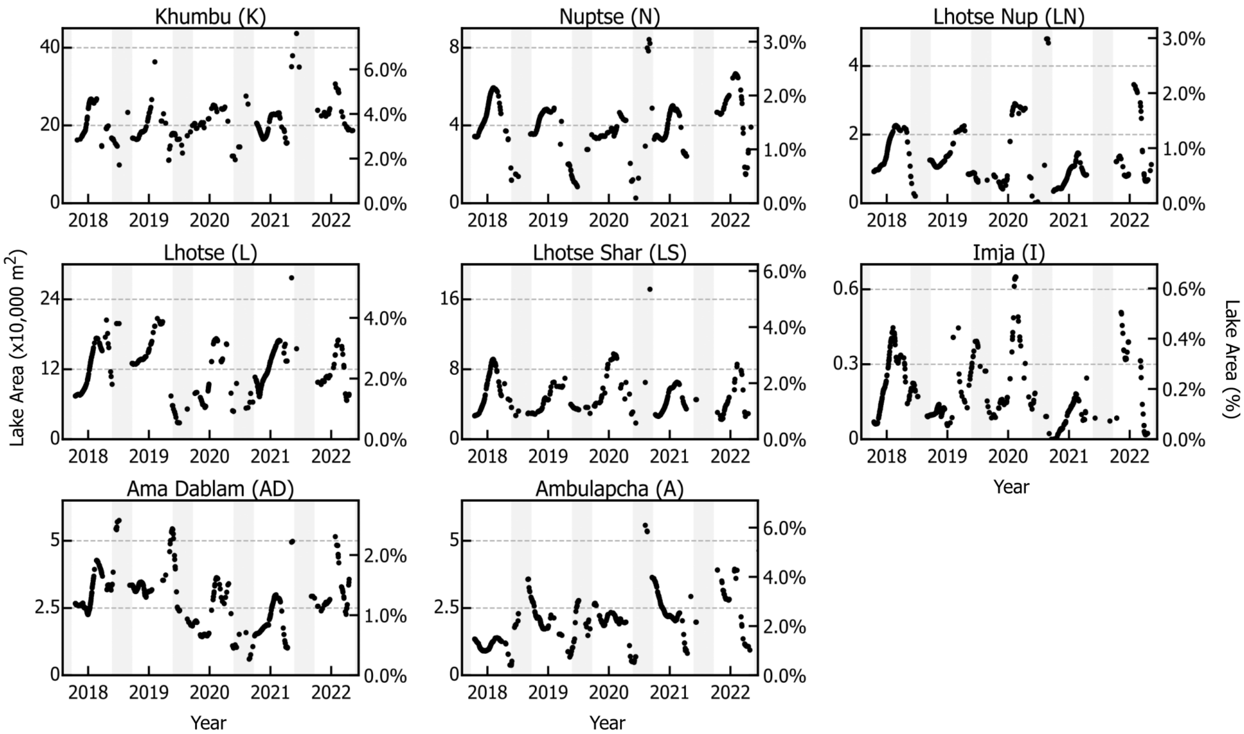

Figure 19: Time series of total SGL area on each glacier from PlanetScope imagery. Each point indicates the total lake area identified from the automated methodology. Grey shaded areas indicate the monsoon season (15 June–30 September). Left axis of each plot shows lake area, while right axis shows the values scaled to a percent of the total debris-covered area.

The wintertime increase in SGL area is not caused by an increase in the frozen SGL area (Figure B2). I find that the maximum frozen lake surface extent occurs in April, and minimal lake surface freezing occurs in the September–December time period during which unfrozen lake area is steadily increasing (Figure B2).

A detailed investigation of the 5-year Planet-derived SGL inventory shows that the seasonal cycle in total SGL area (both frozen and unfrozen) is driven by the regular appearance and expansion of small lakes and supraglacial streams throughout the post-monsoon and winter months in the upper debris-covered regions further from the glacier termini (Figure 20, Figure B4, Figure B5), rather than seasonal growth and/or shrinking of the larger lakes in the study region. Between October and February in each of the 5 years on Lhotse Glacier, lake area increase was greater in regions further from the terminus (Figure 20a). Similarly, the total number of lakes increases throughout these months each year, with this driven predominantly by the increasing number of small lakes (lakes between 45 and 450 m^2, or less than half of a single Landsat pixel) (Figure 20c). Lastly, the relative contribution of smaller lakes to the total lake area increases between October and February each year (Figure 20b). For example, lakes which are smaller in size than a single Landsat pixel (900 m^2) account for an average of 18% of total lake area on Lhotse Glacier in October but account for 34% of total lake area on average in February (Figure 20b). These same patterns are observed (to varying degrees) on most glaciers in this study area, particularly on the four glaciers with the greatest lake area (Khumbu, Nuptse, Lhotse, and Lhotse Shar) (Figure 20, Figure B5-Figure B12).

2.5.2.2. Individual lake dynamics

The high spatial and temporal resolution of PlanetScope imagery allows investigation of the pattern of individual lake filling and drainage events (Figure 21). Analysis of the pattern of individual lake dynamics reveals a complex system, where individual lakes may exhibit seasonal to multiannual patterns of surface area variations that greatly differ from the glacier-wide trends and even nearby lakes.

A total of 2131 unique lakes greater than or equal to 45 m^2 in area were identified in the Planet-derived lake inventory across the 5-year period, ranging in number from 48 to 619 across the eight glaciers (Table 2), with a total area of 1.57 km^2. Of these lakes, only 36 were permanent (never completely draining across the entire study period), representing 1.7% of the

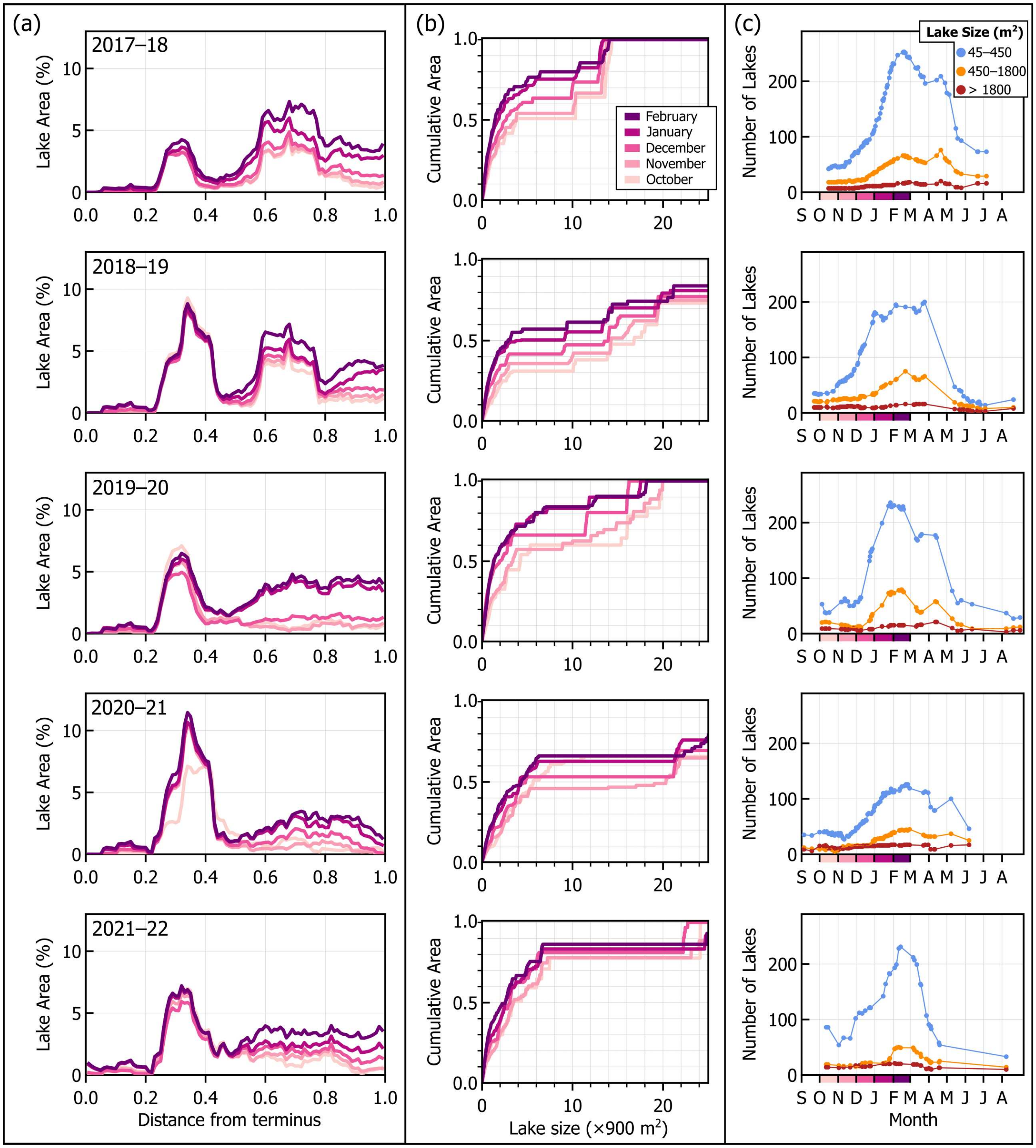

Figure 20: The October-February seasonality of SGLs on Lhotse Glacier, with each row showing a unique year. (a) shows the percent of the glacier area with SGL coverage (y-axis) as a function of the normalized distance form the terminus (x-axis). Each line showing the area in a single month. (b) shows the cumulative SGL area (y-axis) with increasing lake size (x-axis), in each month. The x-axis ticks are shown in 900 m² increments (the size of a single Landsat pixel). Areas are normalized to a 0–1 scale to allow direct comparison between months and years. (c) shows the changes in the number of individual lakes within each image, binned into three different sizes. Blue are smaller in size than half of a Landsat pixel, orange are between one half and two Landsat pixels, and red are greater than two Landsat pixels.

lakes by count and 23.9% by area (at their maximum extents). These permanent lakes tend to be closer to the terminus of their respective glaciers, with an average normalized distance of 0.47 (47% of the distance from the terminus to the upper debris-covered area) compared to 0.66 for all other lakes.

Table 2: Observations of lake count and area on individual glaciers over the 2017–2022 Planet observational period. Note that the number of lakes on a glacier at a single point in time (i.e. Max. #) may be greater than the total number of lakes identified on the glacier over the entire time period (Lake #) if individual lakes merge together to create a single, larger lake. Total lake area, minimum lake area, and maximum lake area are provided in absolute area (m^2) and as a percentage of the glacier's debris-covered area. Annual minimum and maximum lake area and count for each glacier are provided in the supplementary material.

Glacier	Lake #	Lake area (m^2, %)	Permanent lake # (%)	Min. #	Max. #	Min. area (m^2, %)	Max. area (m^2, %)
Ama Dablam	121	115974 (5.2%)	3 (2.48%)	10	112	7641 (0.3%)	57555 (2.6%)
Ambulapcha	48	61749 (6.8%)	0 (0%)	3	64	9081 (1.0%)	55755 (6.1%)
Imja	62	17964 (1.8%)	0 (0%)	0	31	0 (0.0%)	6498 (0.6%)
Khumbu	619	571734 (10.0%)	14 (2.26%)	88	690	162414 (2.8%)	436536 (7.6%)
Lhotse	589	423054 (8.1%)	8 (1.36%)	51	442	54405 (1.0%)	276912 (5.3%)
Lhotse Nup	123	64800 (4.1%)	1 (0.81%)	2	97	3465 (0.2%)	34578 (2.2%)
Lhotse Shar	368	197910 (6.2%)	4 (1.09%)	27	318	22626 (0.7%)	171522 (5.3%)
Nuptse	201	116073 (4.2%)	6 (2.99%)	22	138	32526 (1.2%)	84213 (3.0%)

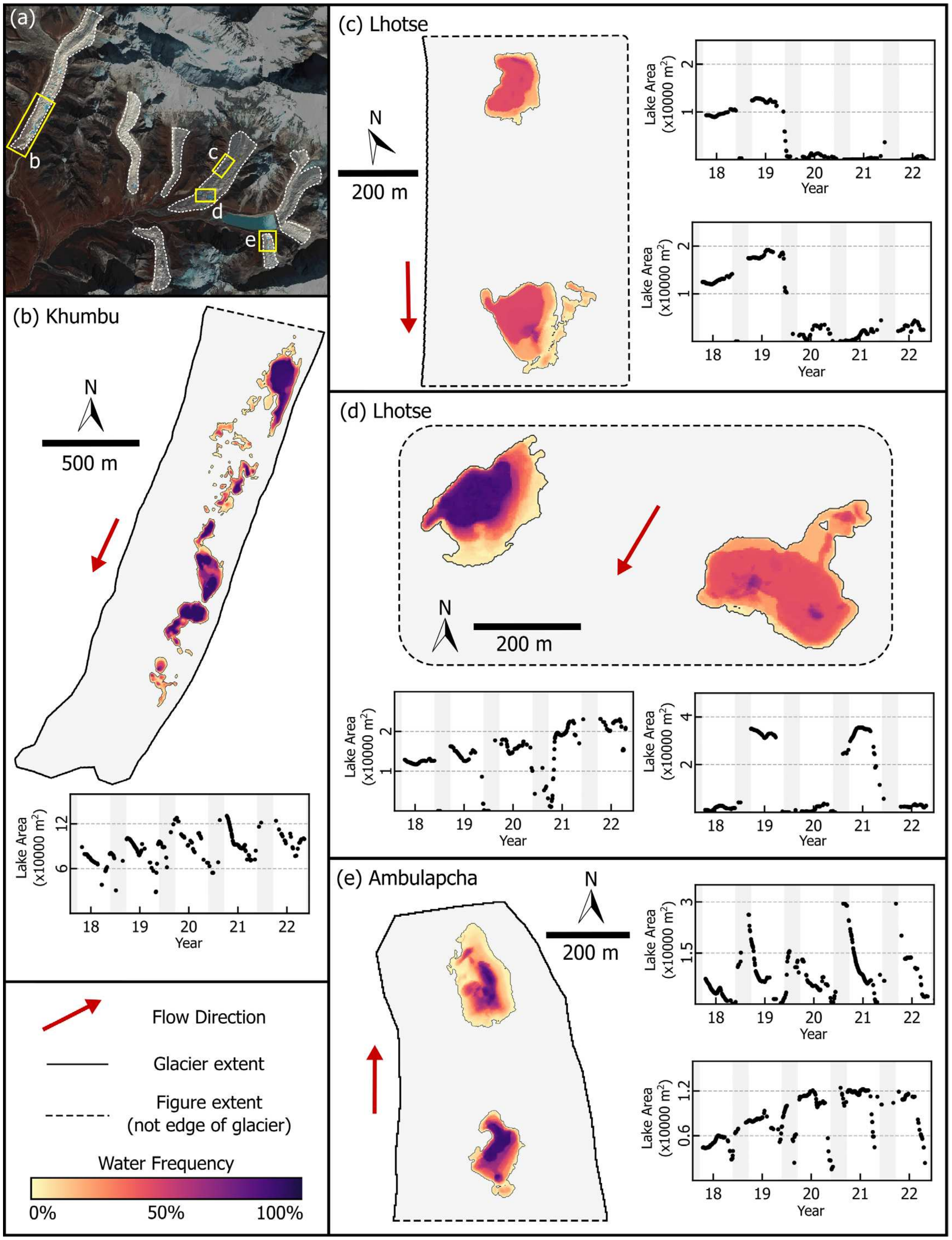

Figure 21: Water frequency maps and time series of select individual lakes or groups of lakes. Locations of each (b-e) are indicated in the top-left overview map. Lake maps are colored by water frequency (darker colors indicating more frequent water). The time series show the total area in individual Planet images. Grey shaded areas indicate monsoon season (15 June-30 September). Year tick-marks indicate the start of each year. Red arrows indicate the glacier flow direction.

The recurrence frequency of the ephemeral (non-permanent) lakes varied substantially based on their size, with larger lakes reappearing more frequently. Lakes smaller than a single Landsat pixel (900 m^2) appeared on average in 2.0 years out of the 5 years of Planet observations, while lakes larger than this threshold appeared in 4.5 years on average (calculated by separating years on 1 September). Only 355 (16.7%) of all lakes appeared in all 5 years, and the average size of these lakes was 3034 m^2 compared to an average size of 277 m^2 for all others.

In some instances (on the Khumbu and Ambulapcha glaciers) the number of lakes identified at a single point in time was greater than the total number of lakes identified on the glacier across the entire study period (Table 2). This may happen if unconnected lakes expand and eventually coalesce into a single lake, resulting in a greater lake area but smaller number of lakes.

I identified multiple lakes greater than 10000 m^2 which experienced rapid drainage events (e.g., Figure 21), which all occur near the onset of the monsoon season (May–June). Drainage events similar to these have been previously documented in this region and can cause significant impacts and damage to downstream communities and infrastructure (Rounce and others, 2017; Miles and others, 2018). In fact, the lake which I observed to rapidly drain twice (in 2019 and 2021) was also noted to be involved in the 2015 flood event documented by Rounce and others (Rounce and others, 2017). Further analysis of the Landsat archive reveals six additional instances of this lake filling and draining within the 2008–2016 time period (and none prior to 2008), and the lake area increased each time that it refilled.

The total SGL area on Ambulapcha Glacier is dominated by two large lakes near the terminus that have distinct and contrasting seasonal patterns (Figure 21). The lake nearest to the terminus rapidly fills during the monsoon season each year and slowly drains throughout the post-monsoon, winter, and pre-monsoon seasons (Figure 21). In contrast, the second lake further from the terminus was consistently present over the duration of the PlanetScope observations, expanded throughout the 5-year period, and completely drained during the onset of the monsoon season in 2022 (Figure 21).

These lakes were empty during the May 2023 field campaign, allowing detailed topographic mapping of the lake basins (Figure 22). Both lakes appeared to have drained englacially, as evidenced by the presence of small ponds and exposed ice at the bottom of each basin. I used UAV-derived DEMs of the basins to construct an area–volume scaling relationship for each by calculating the total surface area and volume with incrementally increasing water depths (0.2 m increments) to a maximum depth of 40 and 24 m (for the lower and upper lake, respectively). The volume of the pre-existing ponded areas in each basin was estimated according to the relationship presented by Watson and others (2018), which built on the findings of Cook and Quincey (2015). The results from the artificial filling of the two basins found that the area–volume relationships of each fall within the range of existing SGL observations (Watson, Quincey, and others, 2018) (Figure 22).

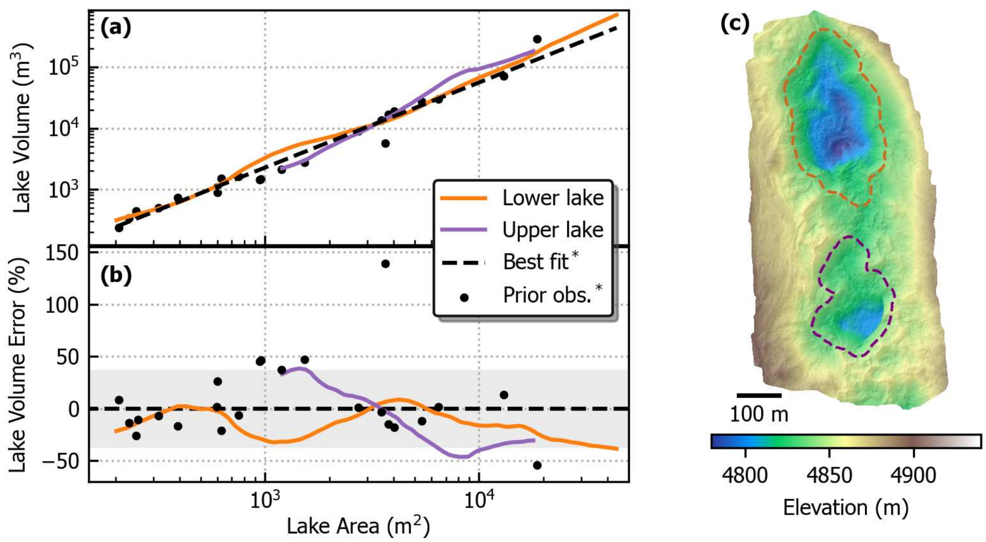

Figure 22: The area-volume scaling relationship for the two large lake basins on Ambulapcha Glacier (purple and orange lines). Black points show previous observations of SGL areas and volumes on Khumbu Glacier by Watson and others (2018b), and the black dashed line is the best-fit relationship presented in the study. (a) shows the area-volume relationship (in log-log scale). (b) shows the percent error that results from using the best-fit equation for estimating volume from an observed area. Grey shaded area shows the 37% mean error from all observations in Watson and others (2018). (c) shows the UAS-derived DEM (hillshade with elevation overlaid) and approximate extents of the two lake basins.

2.5.3. Long-term trends

Complex patterns and trends in SGL evolution over decadal timescales are revealed by the Landsat-derived products, with notable differences being observed between different glaciers, between different parts of individual glaciers, and through time. Over the 1988–2022 period, two of the eight glaciers (Khumbu and Ambulapcha) showed a statistically significant ($P < 0.05$) positive trend in glacier-wide SGL area in Landsat-derived observations, based on a linear regression of the average annual lake area (Figure 23, Figure B13, Table B9). Two glaciers (Imja and Lhotse Shar) showed a statistically significant negative trend, while the remaining four did not have a statistically significant trend. Limiting the time period to only 2013–2022 (after the launch of Landsat 8), I find that only Khumbu has a statistically significant positive trend in SGL area, while the seven other glaciers have no statistically significant trend (Figure 23 and Figure B13).

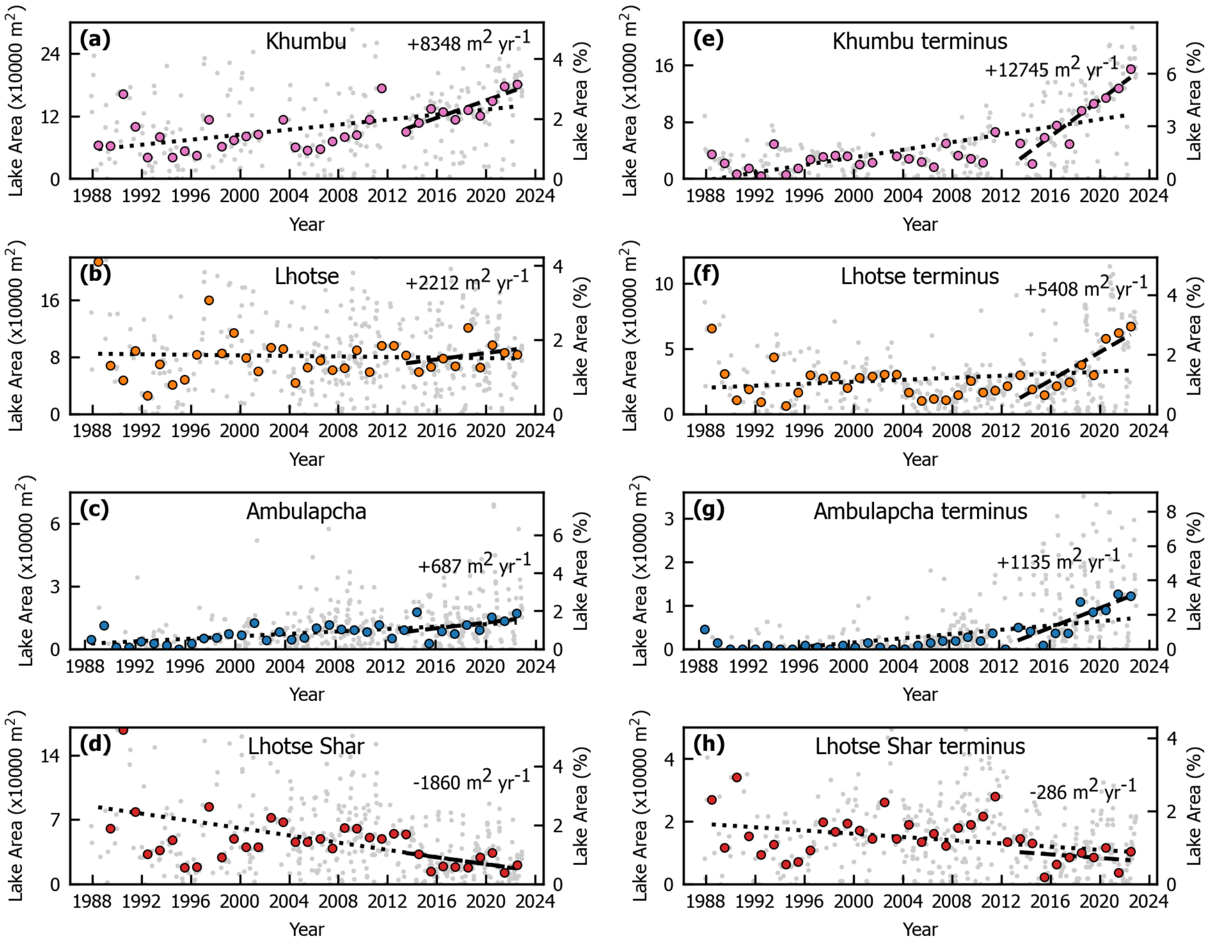

Figure 23: Long term trends in SGL area on four glaciers as derived from Landsat imagery. Light grey dots show the lake area in individual Landsat images, while larger colored dots show the mean SGL area within each calendar year. (a-d) shows the SGL area over the entire glacier surface, while (e-h) show the lake area only on the near-terminus area (defined as the lower 50% of the glacier). Dotted and dashed lines show the linear regression of the annual averages for the entire time period (dotted) and only the 2013–2022 time period (dashed). Labeled slopes correspond to the 2013–2022 linear regression. All slopes and P-values are provided in Table B9.

If I limit the area of investigation of each glacier to include only the lower half of the debris-covered area, where lake area shows less seasonal variation, then I find similar temporal trends. Three glaciers (Khumbu, Nuptse, and Ambulapcha) show an increasing trend over the

1988–2022 period, two (Imja and Lhotse Shar) show a decreasing trend, and the remaining three show no significant trend. In the more recent (2013–2022) period, three glaciers show a statistically significant increasing trend (Khumbu, Lhotse, and Ambulapcha), and one (Ama Dablam) shows a decreasing trend (Figure 23, Figure B13, Table B9). The remaining glaciers show no statistically significant trend over the 2013–22 period, although increasing lake area on Nuptse is significant at the $P < 0.1$ level.

Looking at the decadal-scale changes in spatial distribution of SGLs better illustrates the contrasting patterns among the studied glaciers. The development and expansion of SGLs near the terminus of Khumbu Glacier is clearly visible, while at the same time there is a decrease in the frequency of lakes further up-glacier (Figure 24). Similarly complex patterns of SGL changes are apparent on all glaciers (Figure B14-Figure B20) and offer complementary data to the time series investigation.

2.6. Discussion

2.6.1. Comparison with previous SGL studies

The results of this study highlight how the high temporal resolution of PlanetScope imagery can be leveraged to advance our understanding of supraglacial lake dynamics. Prior analyses of the seasonal cycle of SGLs (Miles and others, 2017; Narama and others, 2017) have largely relied on coarser-resolution Landsat imagery aggregated over decadal time periods in order to identify seasonal trends. While my results show a gradual increase in total lake areas throughout the winter leading up to the onset of the monsoon season, these analyses (neither of which focus on the Khumbu region) have found that SGLs initially appear and fill in the pre-monsoon months (March to April) and then drain throughout the monsoon. A study by Wendleder and others (2021) synthesized Sentinel-2, PlanetScope, and SAR datasets to construct a time series of SGL area over the summer months (April–September) on Baltoro Glacier (Pakistan). Similarly to the previous studies, Wendleder and others (2021) also found that lakes appeared and expanded rapidly in the spring months and drained throughout the summer.

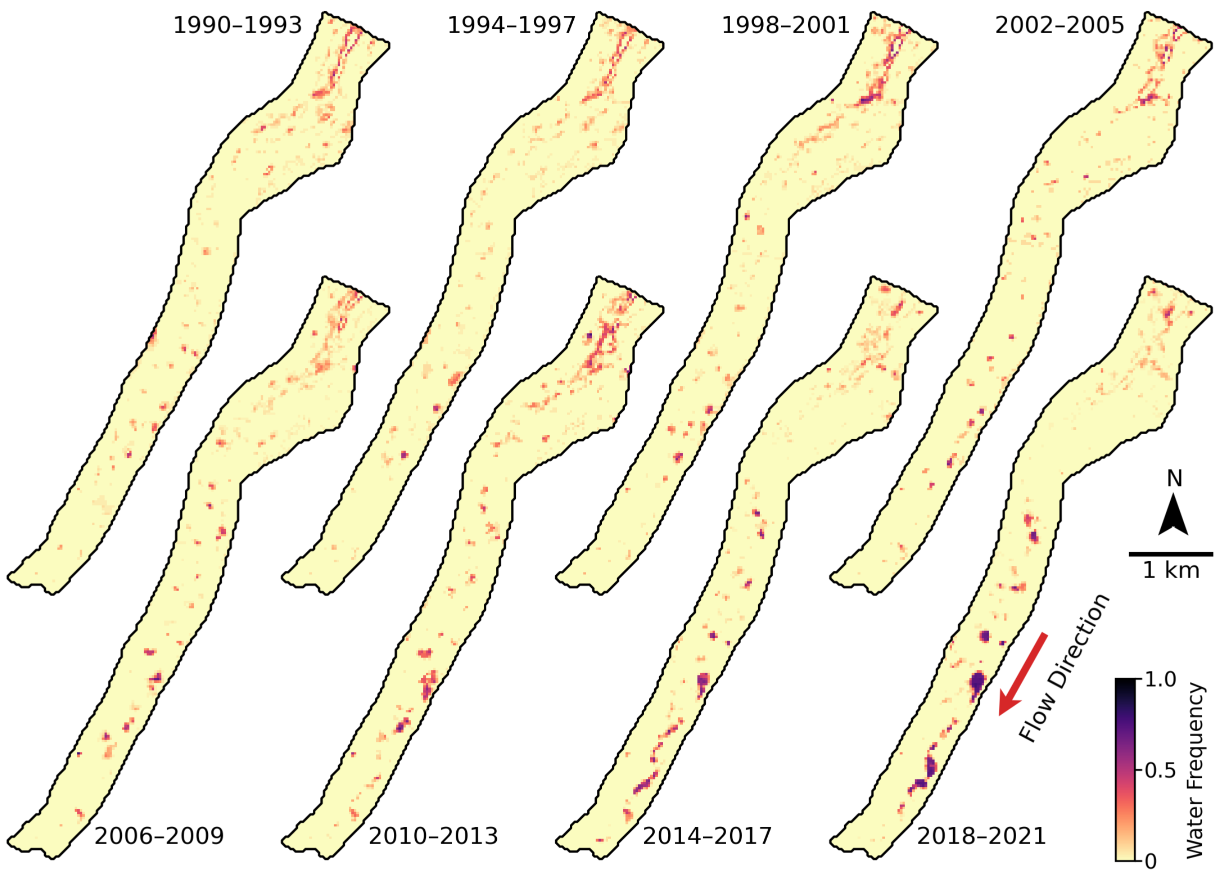

Figure 24: SGL frequency maps of Khumbu Glacier as derived from Landsat imagery. Each figure shows the water distribution aggregated within four-year intervals. Colors show the frequency with which each pixel was identified as water, with darker colors indicating more frequent water.

The differences between these previous studies and my findings showing wintertime lake expansion may be due to differences in regional climate causing different seasonal patterns of lake development, methodological differences (such as minimum lake size identifiable in Landsat images being 225 m^2 if the image is pansharpened), or not including frozen lakes in their inventories. The debris-covered areas of the glaciers in this study region generally do not have continuous snow cover for the entire winter, making SGL identification possible during these months. A study by Taylor and others (2022) found wintertime (December to February) increases in SGL area on two of the three debris-covered glaciers they investigated on the Bhutan–Tibet border and attributed this to variations in efficiency of supraglacial drainage systems between different glaciers and between seasons.

The seasonal variation in SGL area on individual glaciers that I find with the Planet-derived products is of higher magnitude than decadal-scale trends in lake area change from the Landsat record. Many previous studies which use higher-resolution imagery to investigate SGLs on the same glaciers as this study have used a series of images that may cover a wide range of years (up to multiple decades) but are captured at irregular seasonal timings (Watson and others, 2016; Steiner and others, 2019; Mohanty and Maiti, 2021). These results suggest that such study designs are likely to be insufficient for differentiating between the regular annual cycle and the long-term evolution of SGLs described here without controlling for seasonality (i.e., using only images captured during the same month across all years).

Watson and others (2016) investigated the dynamics of SGLs on seven of the eight glaciers in this study (all but Ambulapcha) by using high-resolution (0.5–2 m) imagery over the

2000–2015 time period, with approximately four images of each glacier used. There was no direct overlap between their observations and the PlanetScope-derived products (which are the closest in spatial resolution), but it provides an important opportunity to compare and validate the findings of each. The total area of SGLs identified on each glacier by Watson and others (2016) was similar in magnitude to my results when comparing images from similar times of year (Figure B1). The limited image sample size in their study made it difficult to differentiate between the impacts of long-term SGL evolution and seasonal to annual SGL evolution, although they identified substantial inter- and intra-annual variability in SGL area. For glaciers other than Khumbu Glacier, the main findings were based on a series of three images from October 2011, December 2013, and January 2015. They found that total lake area increased on each glacier over this image series with the largest increases occurring in zones further from the terminus and a trend towards smaller lakes accounting for a larger area (Watson and others, 2016). These results are identical to the annual pattern of wintertime lake development which I observed in the PlanetScope-derived dataset, providing validation of these findings while confirming that the trends observed by Watson and others (2016) on these glaciers can likely be attributed to regular seasonal variations in SGL area rather than longer-term evolution of these glaciers.

Watson and others (2018) presented in situ observations on SGLs near the terminus of Khumbu Glacier over the 2015–2016 year. They found that these lakes reached an annual maximum during the summer monsoon season, followed by continuous shrinkage throughout the following post-monsoon and winter months. These results largely supported the findings by

Miles and others (2017) and Narama and others (2017) (which investigated SGLs in different basins within High Mountain Asia) of the maximum SGL area occurring during the monsoon season and shrinking in the post-monsoon and winter months. My analysis showed a similar annual pattern of lake area in this same area of Khumbu Glacier (Figure 21b), where the maximum lake area is observed at the end of the monsoon season (September) each year, and the area decreases throughout the post-monsoon, winter, and pre-monsoon seasons. The discrepancy between the patterns seen in these lakes and the pattern of total glacier-wide SGL area increasing throughout the post-monsoon and winter seasons (Figure 21) shows that caution is warranted when extrapolating observations across the entire glacier, to other lakes, or to other glaciers, as individual lakes and/or portions of a glacier often have unique spatiotemporal patterns.

The limited availability of cloud-free imagery in the monsoon months limits the ability to draw conclusions about the specific timing and rate of drainage from the automated SGL identification approach. An approach focused on manual lake delineation during the monsoon and pre-monsoon time periods or approaches using SAR data (Wendleder and others, 2021) would be more capable of answering these questions.

These findings highlight how, while satellite remote-sensing platforms are capable of tracking changes in SGL area, they are not able to identify the specific processes which cause lakes to fill and drain. Detailed in situ observations such as those by Watson and others (2018) are needed to complement remotely sensed observations.

2.6.2. Winter lake expansion

Our results showing an increase in total SGL area throughout the winter months are counter-intuitive, as the cold temperatures, limited precipitation, and minimal snow and ice melt would seemingly limit the availability of liquid water and suppress lake formation (Miles and others, 2017). I hypothesize that absorption of solar radiation and conduction to underlying ice in areas with thin debris cover (Rounce and others, 2021; Miles and others, 2022) may lead to meltwater production during winter months, while inefficient drainage systems result in this water pooling at the surface (Miles and others, 2020). This hypothesis is supported by the observation that wintertime lake appearance and expansion are most prominent in the upper debris-covered regions of the glaciers (Figure 21), where debris cover is thinnest, rather than at lower regions where thicker debris cover provides an insulating effect (Rounce and others, 2021). The inconsistent snow cover on the debris-covered tongues of these glaciers (particularly during the early winter months) would increase the potential solar radiation reaching their surface, particularly on the glaciers with more southerly aspects which also show the most consistent wintertime lake expansion (Figure 19). This phenomenon may not be observed on glaciers in other regions with more consistent wintertime snow cover or in regions with climates that are not dominated by the summer monsoon season.

2.6.3. Long-term trends

Our findings highlight many of the difficulties associated with monitoring the long-term evolution of SGLs. The seasonal variations in glacier-wide lake area are of a magnitude similar to or greater than the long-term changes (Figure 19, Figure 23, and Figure B13). The long-term trends in lake area are variable depending on the time period and the specific area of the glacier investigated. I found that SGL area increased near the terminus on four of the glaciers investigated (Khumbu, Lhotse, Ambulapcha, and Nuptse) over the 2013–2022 time period (Fig. 7, Table B9). This observed expansion and possible future coalescing of near-terminus lakes on these glaciers suggest that they should be closely monitored for future outburst flood risk (Benn and others, 2012).

An efficient supraglacial stream network on the surface of Lhotse Shar, combined with a highly incised notch in the terminal moraine, as observed from field observations, has likely prevented large lakes from persisting on its surface. In contrast, Khumbu Glacier has a similarly efficient supraglacial stream network near its terminus, which also flows off the glacier through a deep notch in the terminal moraine, but has nevertheless developed many large SGLs that have been continuously expanding and coalescing in recent years (Naito and others, 2000). This contrasting behavior, compared to Lhotse Shar, may be due to a slightly lower surface gradient and greater number of ice cliffs on Khumbu Glacier. However, the presence of the outlet stream deeply incised into the moraine on Khumbu Glacier may help to limit future SGL expansion.

The recent SGL expansion on Lhotse Glacier is unique within this study region. The lower section of the glacier, downstream from the area of lake expansion, is relatively steep (up to 5° near the terminus), has a well-established stream drainage network, and has little to no terminal moraine. The lake expansion has occurred predominantly in an area $\sim 2\,\mathrm{km}$ from the terminus, at a point where the surface gradient lowers to 2° and maintains that slope for $\sim 3\,\mathrm{km}$ up-glacier. The steep slope and lack of a well-defined terminal moraine suggests that Lhotse

Glacier may not follow the same evolutionary trajectory of terminal lake development as the nearby Imja Tsho. However, sudden drainage of the large SGLs englacially and through the existing supraglacial stream network remains possible (Rounce and others, 2017).

Our long-term time series of SGLs on the Imja and Lhotse Shar glaciers show only a portion of the lakes that are present throughout the time period because a static glacier outline was used. These glaciers were significantly larger in the late 1980s and have been retreating rapidly due to the expansion of their proglacial lake (Imja Tsho). Their transition to lake-terminating glaciers has likely inhibited the growth of supraglacial lakes due to increasing surface velocities. The expansion of Imja Tsho is certain to have further significant effects and feedback on the subglacial, englacial, and supraglacial hydrologic systems of the glacier (Watanabe and others, 2009), but those are not investigated in this paper.

2.6.4. Methodological limitations

The semi-automated approaches used for SGL delineation in Landsat, Sentinel, and PlanetScope imagery substantially increase the amount of data which can be efficiently analyzed relative to manual identification methods. However, it is important to understand the limitations of these automated methods in order to appropriately use the derived products.

The geolocation accuracy of PlanetScope imagery can be poor (up to 10 m RMSE at the 90th percentile), particularly in complex and steep terrain such as the Himalayas, resulting in multi-pixel misalignment between images or between individual bands within the same image. This can inhibit the ability to track spatial and temporal evolution of features as small as SGLs and introduce substantial noise into the data. Differences in the sensors on individual satellites can further add noise. Taking advantage of the high temporal resolution of PlanetScope imagery allows the filtering out of much of the noise and increased confidence in the results. However, significant cloud cover during the pre-monsoon and monsoon seasons, in addition to consistently frozen lake surfaces in the February–April months, lowers the confidence of the results during those times (Figure B1, Figure B2). The decrease in total SGL area that I see on many glaciers between March and June each year is likely due to these cloud and ice limitations, rather than a true decrease in lake area.

Higher geolocation accuracy of Landsat and Sentinel-2 images was observed compared to PlanetScope images relative to their spatial resolution, both between images and between bands in single images. This accuracy, combined with a high degree of consistency in the spectral quality of images, allows Landsat and Sentinel-2 to overcome many of the limitations inherent to using PlanetScope imagery. However, the lower spatial and temporal resolution (particularly for Landsat) means that smaller SGLs and short-term variations are difficult or impossible to identify. Additionally, identifying lakes with frozen surfaces is more difficult without the dense temporal resolution that was used for the Planet-derived dataset, further obscuring wintertime changes in lake area.

2.6.5. Comparison with regional-scale databases

A comparison between the SGL extents produced in this study with regional- or global-scale glacier lake inventories (Wang and others, 2020; Shugar and others, 2020; Chen and others, 2021; Racoviteanu and others, 2021) suggests that existing datasets do not capture the full behavior of SGLs through space and time (Figure 25). I found that three time-varying inventories (Wang and others, 2020; Shugar and others, 2020; Chen and others, 2021) considerably underestimated the extent of modern SGLs on these eight glaciers. The Shugar and others dataset, which used the full Landsat archive to map glacial lakes across the entire globe in 5-year time intervals, does not include any SGLs on these glaciers due to the minimum size threshold of 50000 m^2 that was used. Additionally, two areas of glacial ice were misclassified as lakes in the 2020 product (not shown in Figure 25 because they are up-glacier from the study region). The Chen and others Hi-MAG dataset provides annual glacial lake outlines in the High Mountain Asia region for the 2008–2017 time period derived from Landsat imagery and using a 8100 m^2 minimum size threshold. On these glaciers a single lake was identified on Lhotse Glacier in 1 year, seven total lakes on Khumbu Glacier across 4 years, and no lakes on the other glaciers in this study area. The Wang and others dataset provides glacial lake outlines in the High Mountain Asia region for two timesteps (1990 and 2018) using manual delineation of Landsat imagery and a 5400 m^2 minimum size threshold. Their 2018 data found five SGLs on Lhotse Glacier, two on Ama Dablam Glacier, and five on Khumbu Glacier (and no lakes on the others).

In contrast, Racoviteanu and others (2021) used a spectral unmixing model on Landsat 8 imagery to identify supraglacial ponds on debris-covered glaciers in the Himalayas during the post-monsoon season (September–November) in 2015. Their spectral unmixing approach allowed for identification of ponds that were smaller than a single Landsat pixel. The derived dataset shows a comparable magnitude (falling within the range of the PlanetScope-derived products) and spatial distribution of SGLs to my findings but only provides data for a single time step.

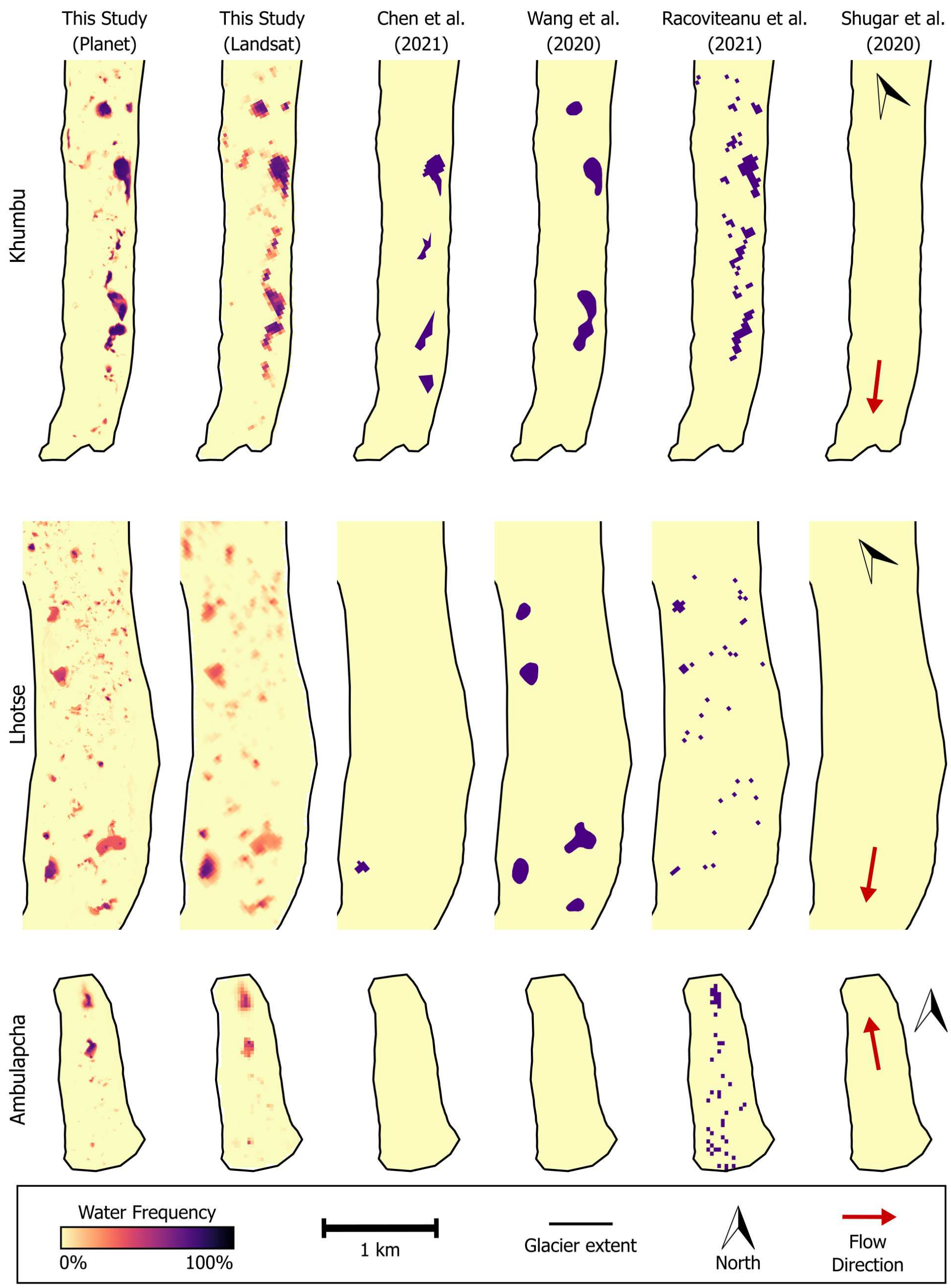

Figure 25: A comparison between the Planet-derived and Landsat-derived lake extents and publicly available regional-scale inventories.

While the differences in SGL number and area of these datasets (Wang and others, 2020; Shugar and others, 2020; Chen and others, 2021) relative to my findings are due primarily to the minimum size threshold used (and the overall aims of their studies), these comparisons highlight how our current understanding of SGL dynamics over regional or global scales is very limited. Studies which focus primarily on the unique spatial and temporal characteristics of SGLs (Racoviteanu and others, 2021) are needed to better characterize these features.

2.7. Conclusions

In this paper, I presented an automated approach to identifying SGLs on debris-covered glaciers from PlanetScope, Sentinel-2, and Landsat imagery. Lake identification in Landsat and Sentinel-2 was optimized using coincident Planet observations. These methods were used to map lake extents on eight glaciers in the Khumbu region of Nepal over the 1988–2022 time period.

A regular annual cycle in SGL development was found, with the annual minimum in glacier-wide lake area occurring at the end of the monsoon season followed by a gradual increase throughout the winter season and a maximum in February and March, followed by drainage throughout the monsoon season. The magnitude of seasonal variations was considerable, with the annual maximum being approximately double the annual minimum. This annual cycle is driven by the appearance and gradual expansion of small lakes in the upper debris-covered regions of these glaciers throughout the winter months, while larger lakes near the glacier termini tended to be more stable or slowly drain during the winter. Over decadal timescales, near-terminus lakes were observed to be expanding and coalescing on four of the glaciers (Khumbu, Lhotse, Ambulapcha, and Nuptse), highlighting the need for continued observation to evaluate the evolving glacier lake outburst flood hazards they present.

The annual cycle in SGL area which I identified has important implications for interpreting prior observations of SGLs. The intra-annual timing of observations must be considered in order to differentiate long-term trends from seasonal variability. A comparison between my results and existing regional-scale glacier lake inventories showed that the complex spatiotemporal patterns are not fully captured in these datasets. These findings highlight the unique capabilities of satellite remote-sensing platforms to track changes in SGL area over time. However, detailed in situ observations are needed to complement these remotely sensed observations to better understand the processes controlling SGL evolution.

2.8. Data availability

All Sentinel-2 and Landsat imagery are available and were accessed via the Google Earth Engine Data Catalogue at https://developers.google.com/earth-engine/datasets/catalog (Google Earth Engine, 2024). Derived products (image-specific lake extents, DEMs, and orthomosaics) and analytical scripts are available via Zenodo (https://doi.org/10.5281/zenodo.10463250; Zeller and others, 2024b).

CHAPTER 3: 21ST CENTURY EXPANSION OF SUPRAGLACIAL LAKES IN HIGH MOUNTAIN ASIA[3]

3.1. Introduction

High Mountain Asia (HMA) in the geographic region encompassing the Tibetan Plateau and surrounding mountains, including the Tien Shan, Karakoram, Hindu Kush, Himalaya, and Nyainqêntanglha ranges (Figure 26). This vast region is host to the largest concentration of mountain glaciers outside of the polar regions, and serves as the headwaters for the major river systems in Asia (Pfeffer and others, 2014; Bolch and others, 2019; Farinotti and others, 2019). Spatial variability in recent glacier mass changes have been observed across the region, ranging from substantial mass loss in the Himalayas to near-zero mass change or even positive mass gain in the Karakoram and Kunlun Shan (Shean and others, 2020; Hugonnet and others, 2021). Changes in these glacial and hydrologic systems have important consequences for downstream communities, ecosystems, and infrastructure (Immerzeel and others, 2020; Li, Lu, and others, 2022).

Supraglacial debris (rock, dirt, and dust) is prevalent on HMA glaciers (Scherler and others, 2018; Herreid and Pellicciotti, 2020), and when this debris cover is continuous across

[3] Chapter 3 has been submitted for publication under the title "21st Century Expansion of Supraglacial Lakes in High Mountain Asia"

much of the ablation zone then the glacier is termed a 'debris-covered glacier' (DCGs) (Miles and others, 2020). Compared to clean-ice glaciers, the presence of debris cover causes significant and complex differences in glacier topography, hydrology, and evolution (Brun and others, 2019), such as increased or decreased ablation rates depending on the supraglacial debris thickness (Rounce and others, 2021) and complex routing of meltwater through supraglacial features (Miles and others, 2020). Supraglacial lakes (SGLs) are an important part of the hydrologic systems of these glaciers. They can increase glacier ablation rates (Miles and others, 2022), provide conduits between the supraglacial, englacial, and subglacial systems (Miles and others, 2019), regulate the timing and magnitude of glacier runoff (Irvine-Fynn and others, 2017), and can pose a hazard to downstream communities by sudden drainage or coalescence into large, proglacial lakes (Watanabe and others, 2009; Rounce and others, 2017).

Previous studies have shown that the characteristic lower surface slopes and slower flow velocities on DCGs enable the formation of SGLs, but these studies have generally focused on the single glacier or catchment scale and used variable methodologies for identifying and investigating the appearance of SGLs (Reynolds, 2000; Watson and others, 2016; Miles and others, 2017; Mertes and others, 2017; Narama and others, 2017; Steiner and others, 2019; Racoviteanu and others, 2021; Zeller and others, 2024b). Many regional- to global-scale glacial lake inventories exist which investigate lake variability at multiple timesteps, but these are focused primarily on proglacial lakes, rather than on supraglacial hydrology (Wang and others, 2020; Shugar and others, 2020; Chen and others, 2021; Zhang and others, 2023).

Despite the important role of SGLs in these high mountain hydrologic systems, there exist substantial knowledge gaps regarding their spatial and temporal prevalence, as well as their decadal-scale evolution (Miles and others, 2020). These knowledge gaps can largely be attributed to the inaccessibility of these regions, the dynamic variability that SGLs exhibit over seasonal-, annual-, and decadal-scales, and the wide range of lake sizes relative to commonly used satellite remote sensing products (Racoviteanu and others, 2022).

The goal of this study is to fill in these knowledge gaps in order to better understand the spatiotemporal dynamics of SGLs across HMA. To do so, I derive a 1988–2023 near-annual inventory of SGL extent across the entire HMA region at 30 m resolution derived from the Landsat archive. I leverage this dataset to investigate the spatial, temporal, and topographic patterns of SGL development to better understand these dynamic features.

3.2. Study Area

All glaciers within the Randolph Glacier Inventory (RGI) regions 13 (Central Asia), 14 (South Asia West), and 15 (South Asia East) which were larger than 2 km^2 and had complete debris cover near their terminus (500 m or more of debris spanning the glacier width) were included in this study, resulting in a total of 769 debris-covered glaciers. Glacier outlines from version 7 of the RGI (RGI Consortium, 2023), which were created in the GAMDAM inventory (Sakai, 2019) were used to define the glacier extents. I manually delineated the predominant debris-covered area within each glacier outline using high resolution ESRI and Google Earth imagery basemaps, cloud-free and snow-free Sentinel-2 imagery, and the debris-cover extents from Herreid and Pellicciotti (2020) as references. I excluded narrow longitudinal bands of debris cover and debris-covered areas adjacent to exposed glacier ice from the analysis, as areas with mixed debris and ice can frequently be misclassified as water.

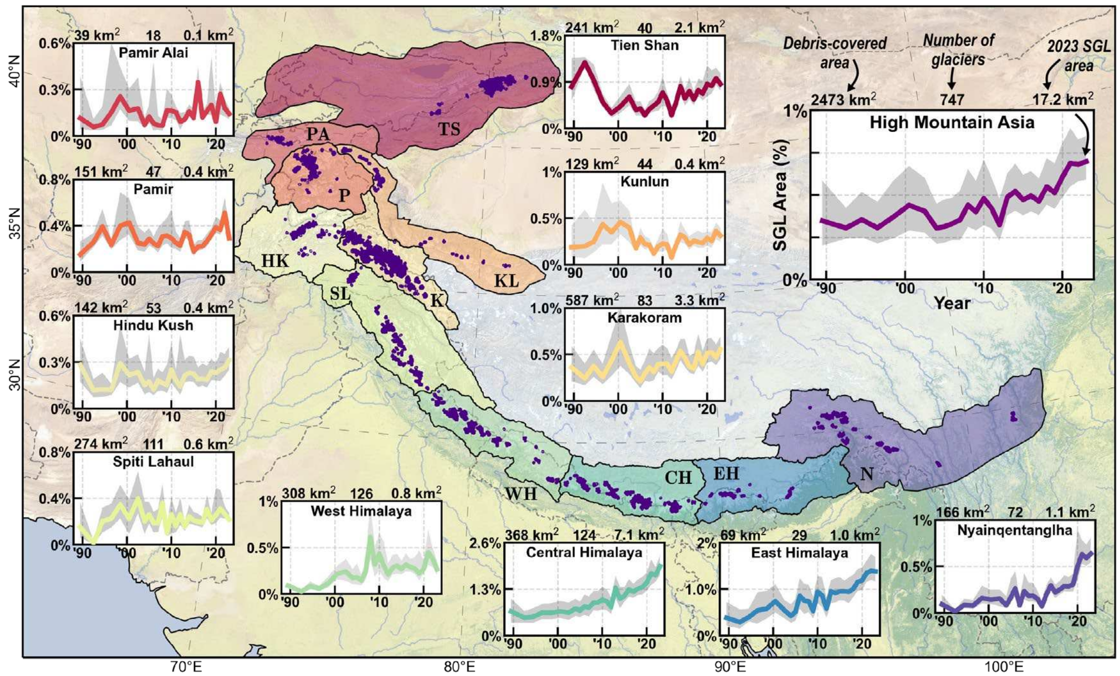

Figure 26: The locations of glaciers included in this study (purple), and the extent of the 11 subregions used. Each subplot shows the time series SGL cover within each subregion, as a percentage of debris-covered area. , as a percentage of debris-covered area. The grey shaded area indicates the range of estimates derived from the variable NDWI thresholds used.

The 769 selected glaciers represent 10% of all glaciers larger than 2 km^2, and the surface area of 18,700 km^2 is 29% of total surface area of HMA glaciers larger than 2km^2 (RGI Consortium, 2023). These glaciers contain a total of 2500 km^2 of debris-covered area which is included in this study, which is 43% of total debris cover on glaciers >2km^2 in the region (Herreid and Pellicciotti, 2020). Twenty-two of the study glaciers were identified as being lake-terminating, with the terminal lakes having expanded into the RGI outlines in the later years of the study. Unless specified otherwise, I do not include these 22 glaciers in the following analyses and instead focus on the 747 remaining, as the terminal lakes should not be considered part of the supraglacial hydrologic system which this study focuses on.

I used 11 subregions defined by Kääb and others (2015) to present regional-scale aggregations and trends (Figure 26). These regions were renamed following Shean and others (2020). Slight adjustments were made to better cluster specific glacier regions, with 19 glaciers added to the Nyainqêntanglha region instead of their original Hengduan Shan/East Himalaya regions.

3.3. Methods

I identified SGL extent on the debris-covered regions of the 769 study glaciers at near-annual timesteps using a fully-automated approach applied to the entire 1988–2023 Landsat 5, 7, 8, and 9 archive.

Usable areas in each Landsat Collection 2, Level 1 surface reflectance image were identified by masking out areas of terrain shadows and cloud cover in Google Earth Engine (GEE) (Gorelick and others, 2017). Terrain shadows were physically modeled using the GEE terrainShadow() algorithm, with the Copernicus WorldDEM-30 (GLO-30 DEM) (European Space Agency and Airbus, 2022) and image-specific sun azimuth and elevation angles as input. Clouds were identified using a combination of the Landsat-provided QA band (which identifies clouds using the CFMask algorithm) and the Automated Cloud Cover Assessment (ACCA) cloud masking approach (Irish, 2000; Zhu and others, 2015). I found that both cloud identification approaches tended to overestimate cloud cover on debris-covered glacier surfaces in different ways. The CFMask routinely identified entire cloud-free and snow-free glaciers as cloud cover, while the ACCA approach misclassified light-colored debris as cloud cover. Therefore, I classified pixels as clouds if they were classified as cloud cover by both the CFMask and ACCA approaches. Areas of exposed glacier ice were identified using the approach described in Zeller and others (2024). These areas, with a buffer of 60 m, were also masked out, as they were frequently mis-classified as water.

SGLs were identified in the remaining usable areas of each image using a thresholding approach on the normalized difference water index (NDWI). A range of thresholds from 0.13–0.25, which have previously been identified as the optimal NDWI thresholds for identifying SGLs from satellite imagery (Watson and others, 2018; Zeller and others, 2024b) were used. Each of the following steps discussed below were repeated for each of the 13 thresholds, and the range of results used to provide an error estimate (described in greater detail below).

The annual water frequency was calculated for each pixel each year by dividing the total number of water observations by the total number of usable observations. SGL extents were extracted from these annual water frequency maps using variable thresholds to account for spatial, seasonal, and inter-annual variability in lake appearance, lake surface freezing, and snow cover. Otsu's method (Otsu, 1979) was used to find the optimal threshold to divide the glacier into "foreground" SGLs and the debris-covered "background". A preliminary threshold was found for each glacier in each year after removing pixels with five or fewer usable observations or zero water observations (these pixels were classified as non-SGL). For years/glaciers where the preliminary threshold was greater than or equal to 0.1 (classified as water in 10% or more of usable observations), this preliminary threshold was taken as the optimal threshold. For other years, the average threshold across all years for each glacier was used as the optimal threshold. In cases where this value was still less than 0.1, a global average of all optimal thresholds (~0.14) was used.

Image availability was notably lower for the 1988 to 2003 years (eight usable observations per year per pixel on average, compared to 28 in 2004–2023), resulting in substantial variability in SGL identification relative to the later years with more frequent imagery. Therefore, I combined multiple years of observations for these earlier periods to increase the number of usable observations. The same processing steps were used to extract SGLs from these multi-year periods, and gave SGL extents for a single four-year timestep from 1988–1991, two-year timesteps from 1992–2003, and annual SGL extents for the 2004–2023 years. This resulted in an average of 16 usable images per glacier per interval from 1988–2003 (Figure 27).

A final SGL extent product was created by combining the results from each of the 13 NDWI thresholds tested (0.13–0.25) by taking pixels which were identified as water in at least 50% of these products. Similarly, maximum and minimum extent estimations were made by using pixels which were identified as water by at least 25% and 75% of the thresholds.

Glacier centerlines were taken from the RGI v7.0, with some manual modifications to better fit the debris-covered geometry. I divided each glacier surface into segments that were 500 m in length along their centerlines. For glaciers with complex branching geometries, unique segments were created along each branch. These glacier segments were used to investigate the factors controlling the formation of SGLs.

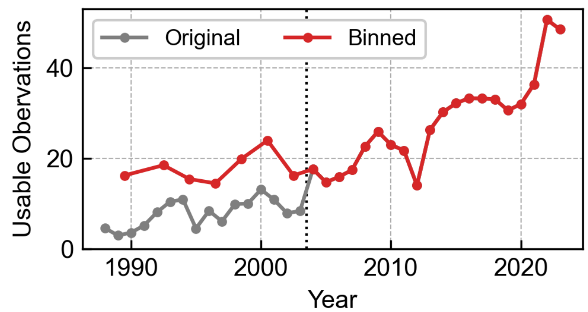

Figure 27: Average number of usable observations per glacier in each year (grey) and when binning the pre-2004 data across multiple years (red).

3.4. Results

Our inventory produced realistic and accurate SGL extents over the study region and study period (Figure 26, Figure 28). The total SGL area across the study region in 2023 was 17.2 km^2, representing 0.7% of total debris-covered area. A substantial increase in SGL extent was found, with the modern SGL area being approximately double the SGL area in both 1988–92 (8.6 km^2) and 2004 (7.5 km^2) (Figure 29). In contrast, the SGL area remained relatively consistent in the 1988–2004 period, although with a substantial increase and subsequent decrease from 1996/1997 to 2004.

The spatial and temporal SGL patterns were variable across the 11 subregions (Figure 26, Figure 29). More than 40% of the modern (2023) SGL area is found in the Central Himalaya region (7.1 km^2), which is more than twice that of the next-largest region (Karakoram). Additionally, SGLs within the Central Himalaya region increased in area more than any other region, nearly tripling in size relative to their 1988–1991 area of 2.5 km^2. The Karakoram and

Tien Shan regions account for substantial portions of the modern SGL area (3.3 km^2 and 2.1 km^2) but have shown relatively little increase over the 35-year study period (2.1 km^2 and 1.9 km^2 in 1988–1991).

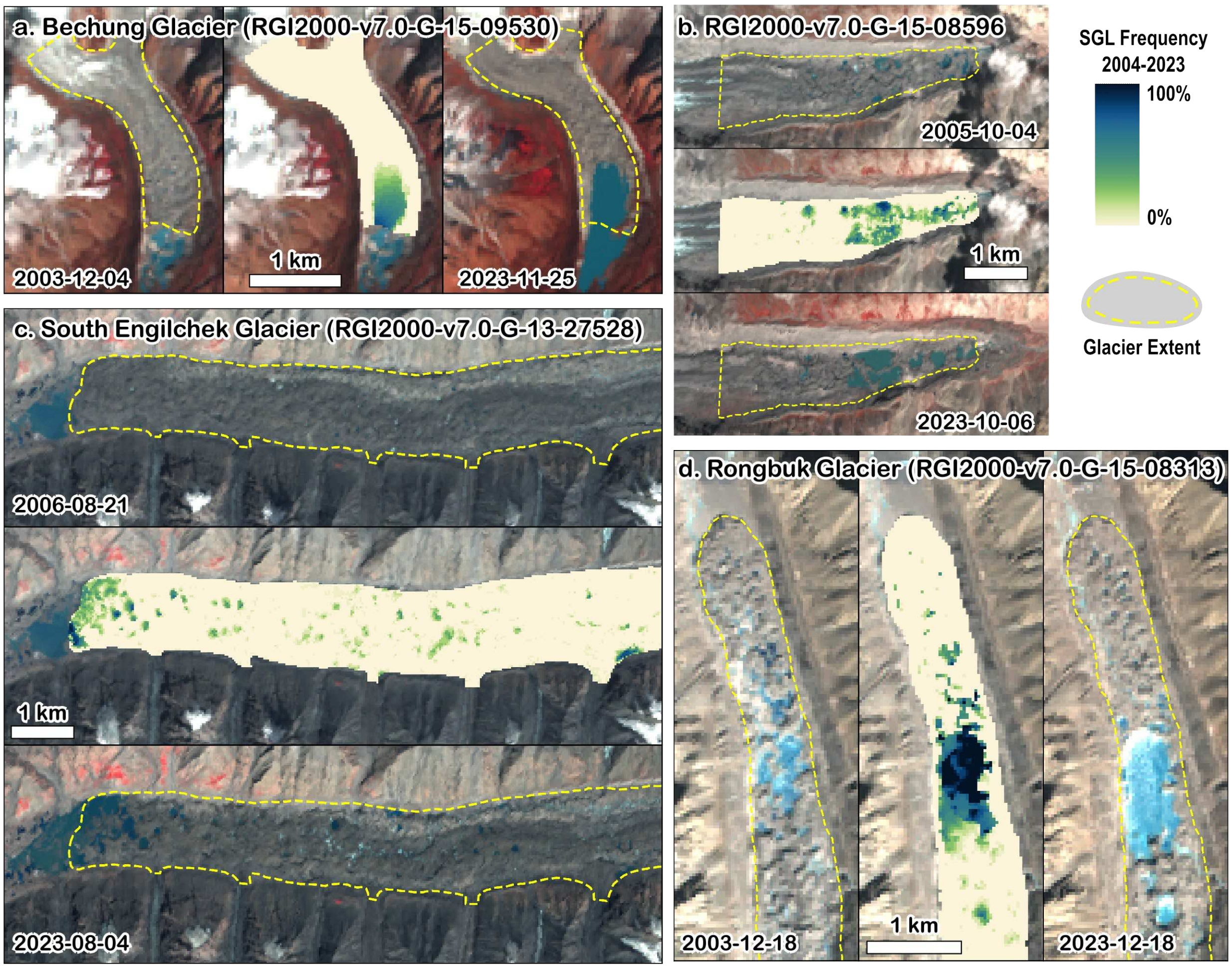

Figure 28: Examples of the 2004–2023 frequency of SGL observations on select glaciers, along with Landsat images showing the glacier near the beginning and end of the period. Images are displayed using near-infrared, red, and green bands. Yellow dashed lines indicate the debris-covered area of each glacier which was used in this study.

A notable southeast/northwest divergence in long-term trends was found, with the more southeastern regions (Spiti Lahaul, the Himalayas, and Nyainqêntanglha) showing consistently increasing SGL areas throughout the entire 35-year period. In contrast, the more northwestern regions had more inconsistent trends with larger inter-annual variability and extended periods of decreasing SGL area (Figure 26), which matches with previous observations of divergent trends in glacial lake evolution in these regions (Gardelle and others, 2011).

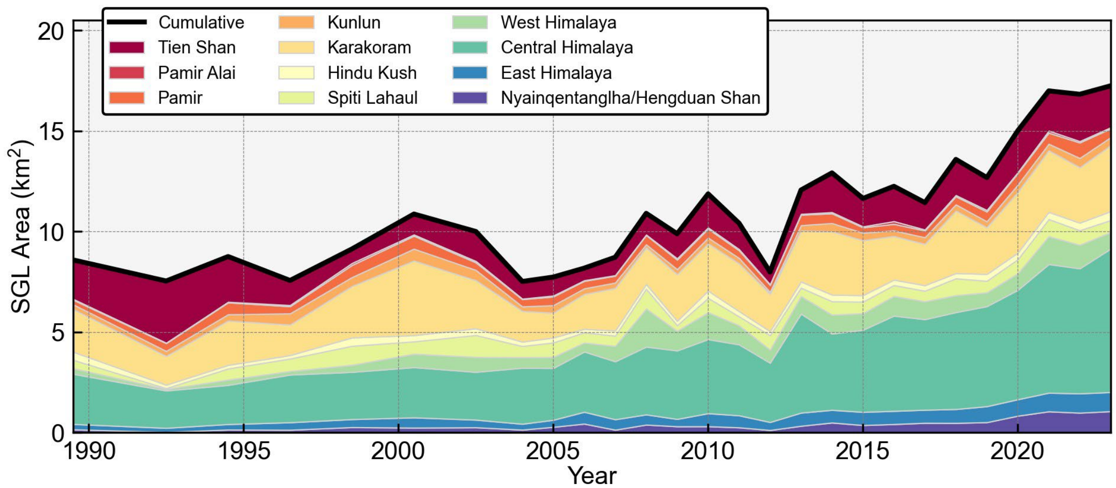

Figure 29: Trend of total SGL area across all glaciers, excluding the lake terminating glaciers. Each color indicates the SGL area within an individual subregion, with colors corresponding to Figure 26.

Of the non-lake-terminating study glaciers, I found that only 111 had a region of substantial SGL concentration. I define "substantial" to be at least 5% SGL cover within a 500 m along-centerline segment of the glacier averaged across multiple years (2005–2009, 2010–2014, 2015–2019, or 2020–2023). 80 of these glaciers had a region of substantial SGL cover in the most recent (2020–2023) period, while 31 did so in one of the previous periods but no longer do. The remaining 636 have not had substantial SGL coverage at any point in the post-2004 period.

This relatively small subset of glaciers (representing 14% by count of all studied glaciers and 33% by debris-covered area) contains approximately 67% of the modern total SGL area, and their relative contribution has been increasing in the 21st century (Figure 30b). These glaciers with substantial SGL cover are predominantly found in the Central Himalaya, Eastern

Himalaya, and Nyainqêntanglha mountain regions (Figure 29), which correspond with regions that have experienced the highest rates of glacier mass loss in HMA in the 21st century (Brun and others, 2017; Shean and others, 2020; Hugonnet and others, 2021).

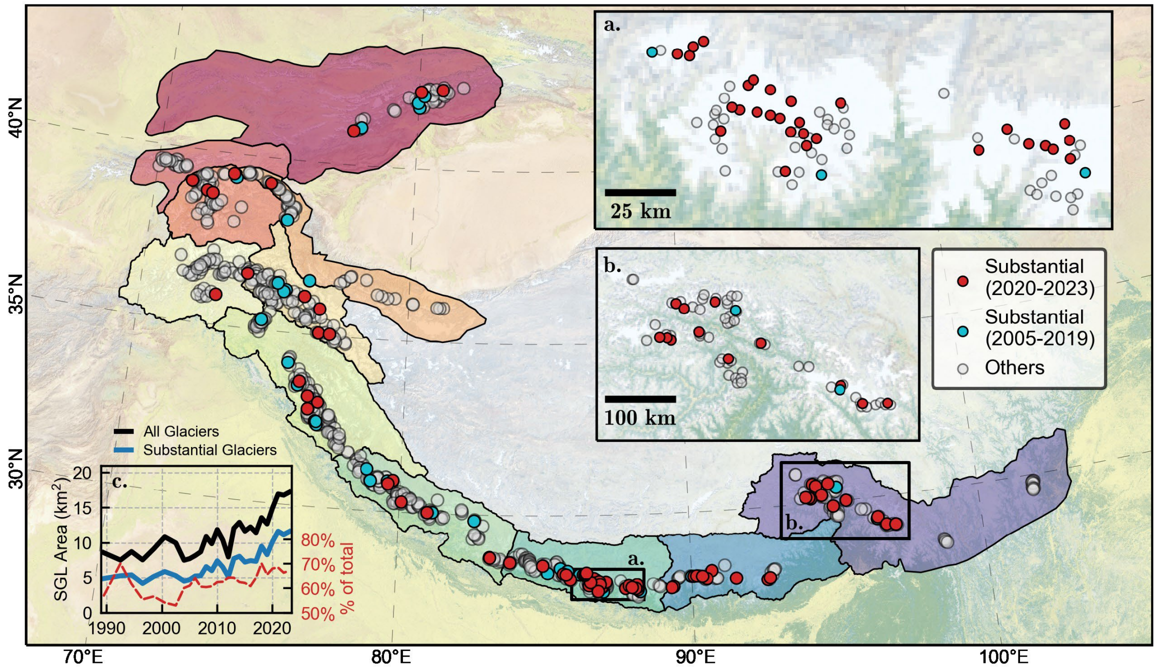

Figure 30: Locations of glaciers with an area of substantial SGL cover at some point in the 2005–2023 period. Red dots indicate glaciers with substantial cover in the 2020–2023 period (n=80), and blue dots indicate glaciers which had substantial cover previously but no longer do (n=31). Gray dots show all other glaciers (n=636). Inset axes show the Everest (a) and Nyainqêntanglha (b) regions with the highest density of these glaciers. (c) shows the total SGL area on the 111 "substantial" glaciers through time.

3.5. Discussion

3.5.1. Comparison to existing glacier lake inventories

I compared these SGL extents to five other inventories of glacial lakes which overlap either the entire study region (Wang and others, 2020; Shugar and others, 2020; Chen and others, 2021) or large portions (Racoviteanu and others, 2021; Zhang and others, 2023). These coincident inventories are variable in terms of the timeframes which they consider, the temporal frequency with which they derived lake extents, the area they cover, and the methodologies which they used. Wang and others (2020) presented a glacial lake inventory across all of HMA at two timesteps, representing 1980 and 2018. Chen and others (2021) presented an inventory of glacial lakes across all of HMA at an annual timescale from 2008–2017. Zhang and others (2023) and Shugar and others (2020) presented glacier lake inventories for five timesteps (1990–2000, 2000–2005, 2005–2010, 2010–2015, and 2015–2020), with Shugar and others deriving global-scale lake extents while Zhang and others derived glacial lakes in the Hindu Kush, Karakoram, Western Himalaya, Central Himalaya, Eastern Himalaya, and Nyainqêntanglha regions. Racoviteanu and others presented an inventory focused specifically on supraglacial lakes in the Himalaya regions at high spatial resolution (minimum lake size of 900 m^2, compared to 3600–50000 m^2 in the other studies) but only a single timestep.

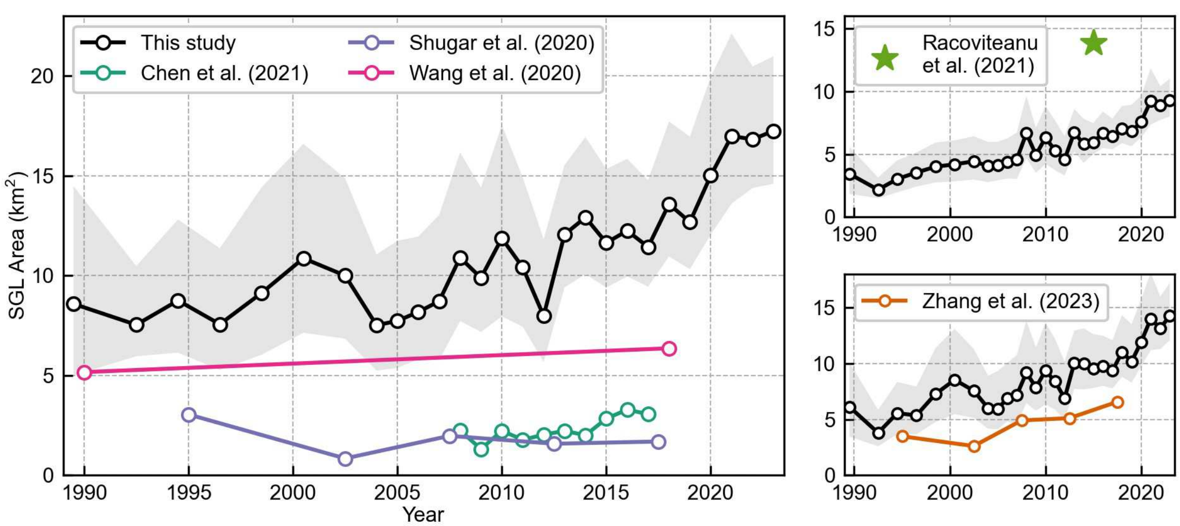

Figure 31: Comparison between my results and other glacier lake inventories (Wang and others, 2020; Shugar and others, 2020; Chen and others, 2021; Racoviteanu and others, 2021; Zhang and others, 2023). Only non-lake-terminating glaciers are included, and each external dataset is subset to only the debris-covered regions of the study glaciers. The inventories presented in Racoviteanu and others and Zhang and others do not overlap with the entire study region, and so I first subset my data to their respective regions prior to comparing.

I find that, relative to my results, the four multi-timestep inventories underestimate the extent of SGLs by approximately 30–90% (Figure 31). Three of those inventories capture the long-term increase in SGLs, while the Shugar and others (2020) inventory does not. These differences are due to the minimal mapping unit which was used in each of these studies (ranging from 4 to 55 Landsat pixels) which precludes the inclusion of the many SGLs which are smaller than this, and the greater focus of these inventories on identifying proglacial lake evolution. This highlights the value of inventories such as ours which shed light on the less well documented supraglacial hydrologic systems. In contrast, my results find a SGL area that is ~50% smaller than Racoviteanu and others (2021) over coincident glaciers and years, which may be attributable to their approach identifying more smaller transient SGLs or misclassification of dark debris and crevassed areas as water.

3.5.2. Near-terminus SGL expansion

An investigation of the longitudinal distribution of SGLs (how far from the glacier terminus that lakes are found) shows that the decadal-scale SGL expansion has occurred almost entirely near glacier termini (Figure 32). Averaging over all glaciers in the 1990–1999 time period, the SGL prevalence was nearly constant along the glacier longitudinal profile, with SGLs covering ~0.2–0.3% of debris-covered area with a slight increase to ~0.5% near the glacier terminus. In later time periods the average SGL fraction has substantially increased in the lower debris-covered extents, rising to 2.1% near the glacier terminus in 2020–2023, a 400% increase. Further, the rate of expansion has increased in recent years, with near-terminus lake expansion rates of 0.11% per year in the 2010–2023 period compared to 0.02% per year for 1990–2009.

This pattern is consistent across the study area, with near-terminus lake expansion found within the majority of the eleven subregions, but most pronounced in the Himalayas, Spiti Lahaul, and Nyainqêntanglha regions (Figure C1). However, it is not consistent across every glacier. If I use only those glaciers that were identified to not have any region with substantial SGL appearance (n=636) (as in Figure 30), then I do not find a clear trend of near-terminus lake expansion, but the pattern is clear and amplified for those with substantial lake development (n=111) (Figure 32). These findings highlight how the spatial and temporal trends of SGL expansion across HMA is driven by only a handful of glaciers, and how SGL development remains relatively uncommon, even on these glaciers that have substantial debris cover.

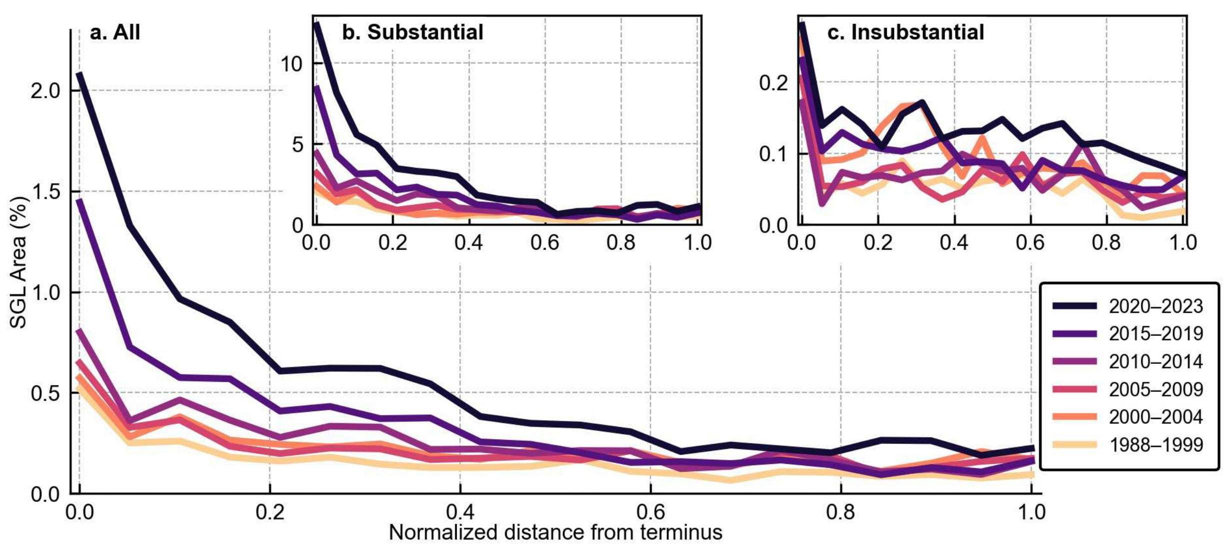

Figure 32: Percent SGL cover (y-axis) as a function of distance from terminus (x-axis). 0 is the glacier terminus, and 1 is the upper limit of the investigated debris-covered area. Each line shows the mean value within each distance bin of all non-lake-terminating glaciers in the study, binned by the years indicated in the legend. Subplot (a) shows the trend for all glaciers in the study, while (b) and (c) show the trends for the 111 "substantial" and 636 non-substantial glaciers.

3.5.3. Drivers of SGL formation

Our spatially and temporally consistent inventory of SGL locations allowed a detailed investigation into the factors controlling the location of SGLs formation. To do so, I compared the average along-centerline glacier surface slope (calculated from the GLO-30 DEM), ice flow velocity (from the 1985–2018 composite ITS_LIVE velocity mosaics (Gardner and others, 2022)), and supraglacial debris thickness (Rounce and others, 2021) for each 500 m glacier segment in this study. I compared the distribution of each of these variables in segments which have substantial SGL cover (greater than or equal to 5%) with the segments that have no SGLs. I found that areas with lower slopes, lower glacier velocity, and thicker supraglacial debris cover are more likely to have substantial SGL cover (Figure 33). These findings support a wide range of previous work which have come to similar conclusions (Reynolds, 2000; Watson and others, 2016; Miles and others, 2017; Mertes and others, 2017; Narama and others, 2017; Steiner and others, 2019; Racoviteanu and others, 2021; Zeller and others, 2024b) but confirm that these patterns hold true at the continental scale. Notably, I am considering only areas of glaciers which have been pre-selected as having significant debris-covered area, and are thus dominated by low slopes and slow velocities. The finding that these differences between SGL-bearing and non-SGL bearing glaciers are evident even within this select subpopulation of glaciers lends credence to the importance of even small variations of slope, velocity, and debris thickness for controlling the formation of SGLs.

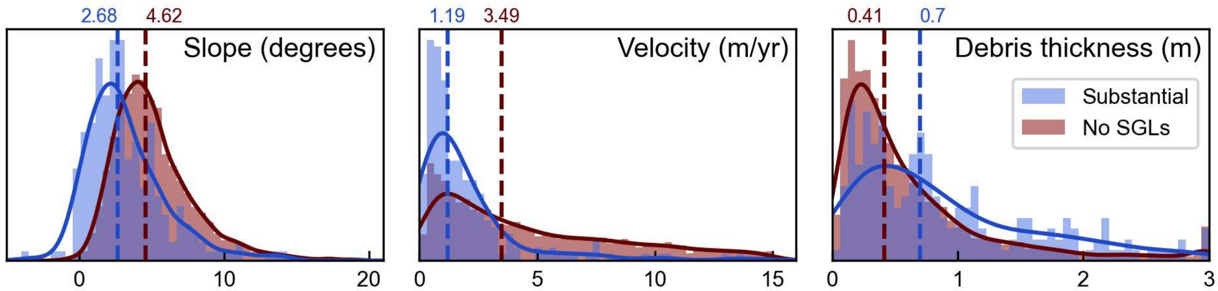

Figure 33: Comparison of the slope, velocity, and debris thickness of the glacier segments which have substantial SGL cover (>5%) and all others. Bar plots show the relative frequency of each variable in each glacier population (scaled to the relative frequency), and the overlain smoothed plots are kernel density estimates of those distributions. Dashed lines and labels indicate the median value of each distribution.

In addition to identifying these topographic signatures at the precise locations where SGL formation is common, I found distinct differences in the geometry of the entire debris-covered regions of these glaciers. The 111 glaciers I identified with substantial SGL formation tend to have lower and more consistent slopes across their entire debris-covered areas compared to the other DCGs in this study, and thus more concave geometries (Figure 34). These geometries are in turn driven by differences in longitudinal thinning patterns. Both populations of DCGs (SGL-bearing and not) exhibit increased rates of thinning at greater distances from the terminus (Figure 34), but this pattern is more exaggerated on the DCGs with substantial SGL formation and has remained constant throughout the 21st century. This thinning pattern is conducive to SGL formation as it lowers the glacier slope, reduces driving stress and glacier velocities, and thus enhances SGL formation. In contrast, glaciers without SGL formation are found to have less exaggerated increases in thinning rates with distance from the terminus (Figure 34). The more consistent rates of thinning throughout maintains the higher slopes and velocities which inhibit SGL formation. However, the average thinning profiles of these non-

SGL-bearing glaciers have shown substantial changes throughout the 21st century, with the thinning profiles in 2015–2020 more closely matching those of SGL-bearing glaciers, suggesting that these glaciers' geometry are trending towards being more conducive to SGL formation in the future.

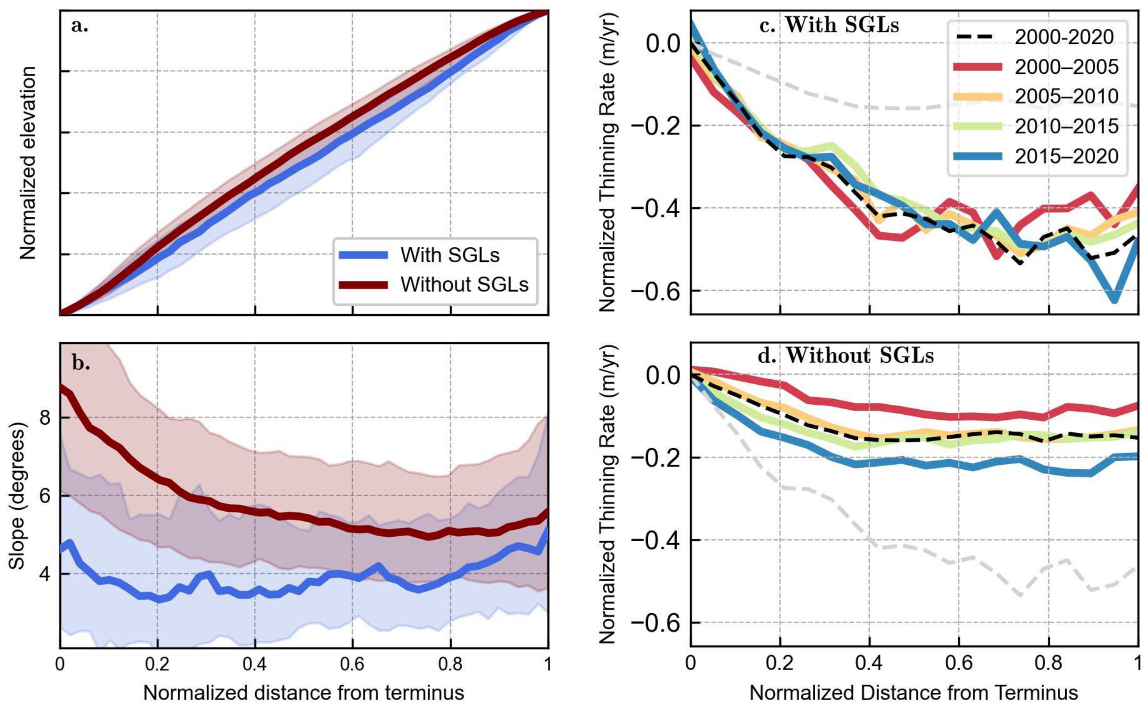

Figure 34: (a) Normalized longitudinal elevation profiles for glaciers with and without substantial SGL formation and (b) the longitudinal slope of those glaciers. The central lines indicate the median value in each longitudinal band across all glaciers, and shaded areas indicate the interquartile range. (c) and (d) show the longitudinal thinning rates of these groups of glaciers. Lower thinning rates indicate a greater rate of surface elevation loss. Each colored line represents a 5-year interval, the black dashed line indicates the average 2000–2020 profile, and the light gray dashed line is the 2000–2020 line from the opposite plot, provided for reference. Data for each glacier is normalized by subtracting the glacier's 2000-2020 average thinning rate at the terminus prior to computing the average across all glaciers.

3.6. Conclusions

In this study I presented an automated methodology to delineate the extent of SGLs on 769 of the largest debris-covered glaciers across all of High Mountain Asia from the entire

Landsat imagery archive (from 1988 to 2023). This inventory shows that the total SGL area has been increasing throughout the study period, but that there is substantial spatial and temporal variability in this expansion. The Himalaya and Nyainqêntanglha regions account for the majority of this increasing SGL area, corresponding to the greatest rates of 21st century glacier mass loss. This expansion of SGLs is concentrated near the termini of glaciers, raising the possibility of future expansion and coalescence into hazardous pro-glacial lakes. Furthermore, only 16% (111) of the studied glaciers account for 67% of the total SGL area, showing how widespread SGL formation is still a relatively rare phenomenon, even on these glaciers with the greatest magnitude of debris cover. Lower surface slopes, slow ice flow velocity, and thicker debris cover were found to be conducive to SGL formation. The typical longitudinal thinning pattern of glaciers with and without substantial SGL cover were distinct, with more exaggerated increases in thinning rates with greater distances from the terminus found for glaciers with substantial SGL cover. The longitudinal thinning pattern was more consistent throughout the entire debris-covered region for other glaciers, but in recent years have become more similar to those of the SGL-bearing glaciers, suggesting that SGL formation may become more frequent in the coming years.

3.7. Data availability

All Landsat imagery and the Copernicus WorldDEM-30 are available and were accessed via the Google Earth Engine Data Catalog at https://developers.google.com/earth-engine/datasets/catalog. Glacier velocity data are available at https://doi.org/10.5067/6II6VW8LLWJ7. Debris thickness data are available at https://doi.org/10.5067/8DQKWY03KJWT. Glacier elevation change products are available at https://doi.org/10.6096/13. All code developed for this study is available through a public GitHub repository: https://github.com/lucas-zeller/HMA_supraglacial_hydrology.

CONCLUSIONS

Glaciers are important components of mountain ecosystems, mountain hydrological systems, and the global water cycle. They are a dynamic part of the earth's surface, and they exhibit variations across wide-ranging spatial and temporal scales. But because of their large sizes, ruggedness, and general inaccessibility there is much that we still do not understand about them. As the global climate continues to change and glaciers continue to retreat and lose mass, it is imperative that we continue to advance our knowledge and improve our ability to estimate future glaciological changes.

With this dissertation, I have demonstrated novel approaches to using satellite-based remote sensing observations to study mountain glaciers. In chapter one, I developed an automated methodology to map the end-of-summer snow cover on over 3,000 glaciers in Alaska and northwest Canada from Sentinel-2 imagery. The fraction of the glacier surface which is snow-covered at the end of the summer melt season can be used as a proxy for the glacier's "health". Greater snow cover (at higher elevations) indicates the glacier is accumulating more mass over the course of a single year that can balance out ice melt at lower elevations, whereas less snow cover indicates that it has less accumulation and therefore may be out of balance with the magnitude of ice melt at lower elevations. From this dataset, I was able to illustrate how these glaciers exist in a state of disequilibrium with modern climate, and must continue to retreat and lose mass in order to reach a more stable geometry. The degree of disequilibrium with both modern and future (end-of-century) climate is variable across the region, with the glaciers in the southernmost regions and smaller glaciers on the exterior of their mountain ranges expected to undergo the most extreme changes in the coming decades.

In chapters two and three I shifted focus to debris-covered glaciers in High Mountain Asia (the mountain ranges surrounding the Tibetan Plateau). The processes controlling the mass balance and evolution of these glaciers are distinct from the more "typical" clean-ice glaciers that are found in Alaska. I investigated the supraglacial hydrology of these glaciers (supraglacial lakes or "SGLs"), as they represent an important and poorly constrained part of these glacial systems. I used high resolution PlanetScope imagery to show how there is a distinct and predictable cycle in the size and distribution of SGLs on eight well-studied glaciers in the Khumbu region of Nepal. The seasonal variability in SGL area which I found was of comparable magnitude to decadal-scale evolution of these features, showing how failing to account for this seasonality may cause misleading conclusions of how the supraglacial systems on these glaciers are changing. Furthermore, the high spatial and temporal resolution patterns of SGL formation which I found were poorly captured in existing regional-scale datasets, highlighting how there is limited understanding of the prevalence of these features across both space and time.

I then showed how the high-resolution PlanetScope imagery could be used to inform best-approaches for utilizing coarser resolution (but freely accessible) Sentinel-2 and Landsat satellite imagery to identify SGLs on debris-covered glaciers. Using these approaches, I developed an automated methodology to delineate the extent of SGLs on 769 of the largest debris-covered glaciers across all of High Mountain Asia from the entire Landsat imagery archive (from 1988 to 2023). This novel inventory shows that the total area of SGLs have been growing in recent years, but that there is substantial spatial and temporal variability in this expansion. The Himalaya and Nyainqêntanglha regions account for the majority of this increasing SGL area, corresponding to the greatest rates of 21st century glacier mass loss. This expansion of SGLs is concentrated near the termini of glaciers, raising the possibility of future expansion and coalescence into hazardous proglacial lakes. Furthermore, only 16% (111) of the studied glaciers account for 67% of the total SGL area, showing how widespread SGL formation is still a relatively rare phenomenon, even on these glaciers with the greatest magnitude of debris cover. I identified the topographic factors which are conducive to SGL formation, with low surface slopes, slow ice flow velocity, and thicker debris cover being important factors. By analyzing the longitudinal patterns of thinning, I showed how these conditions have become more common in recent years, suggesting that SGL formation may become more frequent in the coming years.

Taken together, these studies show how improvements in the availability of satellite-based remote sensing observations can be leveraged to advance our understanding of mountain glaciers at wide-ranging spatial and temporal scales. As earth observation datasets and computational power/techniques continue to improve, there will be ever increasing opportunities to use these tools to expand our understanding of the spatial and temporal characteristics of mountain glacier evolution.

There is still a need to combine these remotely-sensed datasets with in situ observations in order to provide more in situ calibration and validation data to ensure that remotely-sensed observations are accurate and trustworthy, as well as to investigate processes happening at smaller spatial and temporal scales which satellite observations cannot capture. This is particularly true of debris-covered glaciers and their hydrologic systems, as shown in the work I have presented here. Implementing field campaigns which investigate the changes that supraglacial lakes and streams undergo over daily-to-monthly timescales would provide much needed insight on how the seasonal evolution of these systems observed from PlanetScope imagery manifests in term of the magnitude of transient water storage and energy balances and transfers between the water and glacial ice. Increasing the number of SGL bathymetric surveys, and implementing repeated surveys of the same lakes, would improve our assessment of the risks of sudden drainage of these features and their potential to increase glacier melt rates.

The continued development of remotely-sensed and in situ datasets that are both independent and complementary can facilitate integrated approaches to studying mountain glaciers and better prepare society for the effects of their changing landscapes over the coming decades.

REFERENCES

Alexander D, Shulmeister J and Davies T (2011) High basal melting rates within high-precipitation temperate glaciers. *Journal of Glaciology* 57(205), 789–795. doi:10.3189/002214311798043726.

Beamer JP, Hill DF, McGrath D, Arendt A and Kienholz C (2017) Hydrologic impacts of changes in climate and glacier extent in the G ulf of A laska watershed. *Water Resources Research* 53(9), 7502–7520. doi:10.1002/2016WR020033.

Benn DI and others (2012) Response of debris-covered glaciers in the Mount Everest region to recent warming, and implications for outburst flood hazards. *Earth-Science Reviews* 114(1–2), 156–174. doi:10.1016/j.earscirev.2012.03.008.

Benn DI, Wiseman S and Hands KA (2001) Growth and drainage of supraglacial lakes on debris-mantled Ngozumpa Glacier, Khumbu Himal, Nepal. *Journal of Glaciology* 47(159), 626–638. doi:10.3189/172756501781831729.

Bolch T and others (2019) Status and Change of the Cryosphere in the Extended Hindu Kush Himalaya Region. Wester P, Mishra A, Mukherji A, and Shrestha AB eds. *The Hindu Kush Himalaya Assessment*. Springer International Publishing, Cham, 209–255. doi:10.1007/978-3-319-92288-1_7.

Bolch T, Buchroithner MF, Peters J, Baessler M and Bajracharya S (2008) Identification of glacier motion and potentially dangerous glacial lakes in the Mt. Everest region/Nepal using spaceborne imagery. *Natural Hazards and Earth System Sciences* 8(6), 1329–1340. doi:10.5194/nhess-8-1329-2008.

Breiman L (2001) Random Forests. *Machine Learning* 45(1), 5–32. doi:10.1023/A:1010933404324.

Brun F and others (2019) Heterogeneous Influence of Glacier Morphology on the Mass Balance Variability in High Mountain Asia. *Journal of Geophysical Research: Earth Surface* 124(6), 1331–1345. doi:10.1029/2018JF004838.

Brun F, Berthier E, Wagnon P, Kääb A and Treichler D (2017) A spatially resolved estimate of High Mountain Asia glacier mass balances from 2000 to 2016. *Nature Geoscience* 10(9), 668–673. doi:10.1038/ngeo2999.

Carturan L, Rastner P and Paul F (2020) On the disequilibrium response and climate change vulnerability of the mass-balance glaciers in the Alps. *Journal of Glaciology* 66(260), 1034–1050. doi:10.1017/jog.2020.71.

Cauvy-Fraunié S and Dangles O (2019) A global synthesis of biodiversity responses to glacier retreat. *Nature Ecology & Evolution* 3(12), 1675–1685. doi:10.1038/s41559-019-1042-8.

Chen F and others (2021) Annual 30 m dataset for glacial lakes in High Mountain Asia from 2008 to 2017. *Earth System Science Data* 13(2), 741–766. doi:10.5194/essd-13-741-2021.

Ciracì E, Velicogna I and Swenson S (2020) Continuity of the Mass Loss of the World's Glaciers and Ice Caps From the GRACE and GRACE Follow-On Missions. *Geophysical Research Letters* 47(9), e2019GL086926. doi:10.1029/2019GL086926.

Cogley JG and others (2010) Glossary of glacier mass balance and related terms. *IHP-VII Technical Documents in Hydrology No. 86, IACS Contribution No. 2.*

Colgan W and others (2016) Glacier crevasses: Observations, models, and mass balance implications. *Reviews of Geophysics* 54(1), 119–161. doi:10.1002/2015RG000504.

Cook SJ and Quincey DJ (2015) Estimating the volume of Alpine glacial lakes. *Earth Surface Dynamics* 3(4), 559–575. doi:10.5194/esurf-3-559-2015.

Copernicus Climate Change Service (2019) ERA5-Land monthly averaged data from 2001 to present. doi:10.24381/CDS.68D2BB30.

Davaze L, Rabatel A, Dufour A, Hugonnet R and Arnaud Y (2020) Region-Wide Annual Glacier Surface Mass Balance for the European Alps From 2000 to 2016. *Frontiers in Earth Science* 8, 149. doi:10.3389/feart.2020.00149.

Deline P and others (2021) Ice loss from glaciers and permafrost and related slope instability in high-mountain regions. *Snow and Ice-Related Hazards, Risks, and Disasters*. Elsevier, 501–540. doi:10.1016/B978-0-12-817129-5.00015-9.

Dozier J (1989) Spectral signature of alpine snow cover from the landsat thematic mapper. *Remote Sensing of Environment* 28, 9–22. doi:10.1016/0034-4257(89)90101-6.

Edwards TL and others (2021) Projected land ice contributions to twenty-first-century sea level rise. *Nature* 593(7857), 74–82. doi:10.1038/s41586-021-03302-y.

European Space Agency and Airbus (2022) Copernicus DEM. doi:10.5270/ESA-c5d3d65.

Evans SG and others (2009) Catastrophic detachment and high-velocity long-runout flow of Kolka Glacier, Caucasus Mountains, Russia in 2002. *Geomorphology* 105(3–4), 314–321. doi:10.1016/j.geomorph.2008.10.008.

Eyring V and others (2016) Overview of the Coupled Model Intercomparison Project Phase 6 (CMIP6) experimental design and organization. *Geoscientific Model Development* 9(5), 1937–1958. doi:10.5194/gmd-9-1937-2016.

Farinotti D and others (2019) A consensus estimate for the ice thickness distribution of all glaciers on Earth. *Nature Geoscience* 12(3), 168–173. doi:10.1038/s41561-019-0300-3.

Florentine C, Sass L, McNeil C, Baker E and O'Neel S (2023) How to handle glacier area change in geodetic mass balance. *Journal of Glaciology*, 1–7. doi:10.1017/jog.2023.86.

Florentine C, Harper J and Fagre D (2020) Parsing complex terrain controls on mountain glacier response to climate forcing. *Global and Planetary Change* 191, 103209. doi:10.1016/j.gloplacha.2020.103209.

Florentine C, Harper J, Fagre D, Moore J and Peitzsch E (2018) Local topography increasingly influences the mass balance of a retreating cirque glacier. *The Cryosphere* 12(6), 2109–2122. doi:10.5194/tc-12-2109-2018.

Fountain AG, Hoffman MJ, Granshaw F and Riedel J (2009) The 'benchmark glacier' concept – does it work? Lessons from the North Cascade Range, USA. *Annals of Glaciology* 50(50), 163–168. doi:10.3189/172756409787769690.

Frederikse T and others (2020) The causes of sea-level rise since 1900. *Nature* 584(7821), 393–397. doi:10.1038/s41586-020-2591-3.

Furian W, Maussion F and Schneider C (2022) Projected 21st-Century Glacial Lake Evolution in High Mountain Asia. *Frontiers in Earth Science* 10, 821798. doi:10.3389/feart.2022.821798.

Gao B (1996) NDWI—A normalized difference water index for remote sensing of vegetation liquid water from space. *Remote Sensing of Environment* 58(3), 257–266. doi:10.1016/S0034-4257(96)00067-3.

Gao J and Liu Y (2001) Applications of remote sensing, GIS and GPS in glaciology: a review. *Progress in Physical Geography: Earth and Environment* 25(4), 520–540. doi:10.1177/030913330102500404.

Gardelle J, Arnaud Y and Berthier E (2011) Contrasted evolution of glacial lakes along the Hindu Kush Himalaya mountain range between 1990 and 2009. *Global and Planetary Change* 75(1–2), 47–55. doi:10.1016/j.gloplacha.2010.10.003.

Gardner A, Fahnestock M and Scambos T (2022) MEASURES ITS_LIVE Regional Glacier and Ice Sheet Surface Velocities, Version 1. doi:10.5067/6II6VW8LLWJ7.

Geck J, Hock R, Loso MG, Ostman J and Dial R (2021) Modeling the impacts of climate change on mass balance and discharge of Eklutna Glacier, Alaska, 1985–2019. *Journal of Glaciology* 67(265), 909–920. doi:10.1017/jog.2021.41.

Gorelick N, Hancher M, Dixon M, Ilyushchenko S, Thau D and Moore R (2017) Google Earth Engine: Planetary-scale geospatial analysis for everyone. *Remote Sensing of Environment* 202, 18–27. doi:10.1016/j.rse.2017.06.031.

Guo Z, Geng L, Shen B, Wu Y, Chen A and Wang N (2021) Spatiotemporal Variability in the Glacier Snowline Altitude across High Mountain Asia and Potential Driving Factors. *Remote Sensing* 13(3), 425. doi:10.3390/rs13030425.

Herreid S and Pellicciotti F (2020) The state of rock debris covering Earth's glaciers. *Nature Geoscience* 13(9), 621–627. doi:10.1038/s41561-020-0615-0.

Hock R and others (2019) GlacierMIP – A model intercomparison of global-scale glacier mass-balance models and projections. *Journal of Glaciology* 65(251), 453–467. doi:10.1017/jog.2019.22.

Hugonnet R and others (2021) Accelerated global glacier mass loss in the early twenty-first century. *Nature* 592(7856), 726–731. doi:10.1038/s41586-021-03436-z.

Huss M and others (2017) Toward mountains without permanent snow and ice. *Earth's Future* 5(5), 418–435. doi:10.1002/2016EF000514.

Huss M (2013) Density assumptions for converting geodetic glacier volume change to mass change. *The Cryosphere* 7(3), 877–887. doi:10.5194/tc-7-877-2013.

Huss M (2012) Extrapolating glacier mass balance to the mountain-range scale: the European Alps 1900–2100. *The Cryosphere* 6(4), 713–727. doi:10.5194/tc-6-713-2012.

Huss M, Hock R, Bauder A and Funk M (2012) Conventional versus reference-surface mass balance. *Journal of Glaciology* 58(208), 278–286. doi:10.3189/2012JoG11J216.

Huss M and Hock R (2018) Global-scale hydrological response to future glacier mass loss. *Nature Climate Change* 8(2), 135–140. doi:10.1038/s41558-017-0049-x.

Immerzeel WW and others (2020) Importance and vulnerability of the world's water towers. *Nature* 577(7790), 364–369. doi:10.1038/s41586-019-1822-y.

Irish RR (2000) Landsat 7 automatic cloud cover assessment. Shen SS and Descour MR eds. Orlando, FL, 348. doi:10.1117/12.410358.

Irvine-Fynn TDL and others (2017) Supraglacial Ponds Regulate Runoff From Himalayan Debris-Covered Glaciers: Supraglacial Ponds Regulate Runoff. *Geophysical Research Letters* 44(23), 11,894-11,904. doi:10.1002/2017GL075398.

Jakob L and Gourmelen N (2023) Glacier Mass Loss Between 2010 and 2020 Dominated by Atmospheric Forcing. *Geophysical Research Letters* 50(8), e2023GL102954. doi:10.1029/2023GL102954.

Kääb A and others (2021) Sudden large-volume detachments of low-angle mountain glaciers – more frequent than thought? *The Cryosphere* 15(4), 1751–1785. doi:10.5194/tc-15-1751-2021.

Kääb A, Treichler D, Nuth C and Berthier E (2015) Brief Communication: Contending estimates of 2003–2008 glacier mass balance over the Pamir–Karakoram–Himalaya. *The Cryosphere* 9(2), 557–564. doi:10.5194/tc-9-557-2015.

Kavan J and Haagmans V (2021) Seasonal dynamics of snow ablation on selected glaciers in central Spitsbergen derived from Sentinel-2 satellite images. *Journal of Glaciology* 67(265), 961–966. doi:10.1017/jog.2021.36.

Kern Z and László P (2010) Size specific steady-state accumulation-area ratio: an improvement for equilibrium-line estimation of small palaeoglaciers. *Quaternary Science Reviews* 29(19–20), 2781–2787. doi:10.1016/j.quascirev.2010.06.033.

Kienholz C, Herreid S, Rich JL, Arendt AA, Hock R and Burgess EW (2015) Derivation and analysis of a complete modern-date glacier inventory for Alaska and northwest Canada. *Journal of Glaciology* 61(227), 403–420. doi:10.3189/2015JoG14J230.

Klug C and others (2018) Geodetic reanalysis of annual glaciological mass balances (2001–2011) of Hintereisferner, Austria. *The Cryosphere* 12(3), 833–849. doi:10.5194/tc-12-833-2018.

Kochtitzky W and others (2022) The unquantified mass loss of Northern Hemisphere marine-terminating glaciers from 2000–2020. *Nature Communications* 13(1), 5835. doi:10.1038/s41467-022-33231-x.

Kulp SA and Strauss BH (2019) New elevation data triple estimates of global vulnerability to sea-level rise and coastal flooding. *Nature Communications* 10(1), 4844. doi:10.1038/s41467-019-12808-z.

Lane SN, Bakker M, Gabbud C, Micheletti N and Saugy J-N (2017) Sediment export, transient landscape response and catchment-scale connectivity following rapid climate warming and Alpine glacier recession. *Geomorphology* 277, 210–227. doi:10.1016/j.geomorph.2016.02.015.

Larsen CF, Burgess E, Arendt AA, O'Neel S, Johnson AJ and Kienholz C (2015) Surface melt dominates Alaska glacier mass balance. *Geophysical Research Letters* 42(14), 5902–5908. doi:10.1002/2015GL064349.

Li D and others (2022) High Mountain Asia hydropower systems threatened by climate-driven landscape instability. *Nature Geoscience* 15(7), 520–530. doi:10.1038/s41561-022-00953-y.

Li X, Wang N and Wu Y (2022) Automated Glacier Snow Line Altitude Calculation Method Using Landsat Series Images in the Google Earth Engine Platform. *Remote Sensing* 14(10), 2377. doi:10.3390/rs14102377.

Lorrey AM and others (2022) Southern Alps equilibrium line altitudes: four decades of observations show coherent glacier–climate responses and a rising snowline trend. *Journal of Glaciology* 68(272), 1127–1140. doi:10.1017/jog.2022.27.

Mahony CR, Wang T, Hamann A and Cannon AJ (2022) A global climate model ensemble for downscaled monthly climate normals over North America. *International Journal of Climatology* 42(11), 5871–5891. doi:10.1002/joc.7566.

McGrath D, Sass L, O'Neel S, Arendt A and Kienholz C (2017) Hypsometric control on glacier mass balance sensitivity in Alaska and northwest Canada. *Earth's Future* 5(3), 324–336. doi:10.1002/2016EF000479.

McNabb RW and Hock R (2014) Alaska tidewater glacier terminus positions, 1948–2012. *Journal of Geophysical Research: Earth Surface* 119(2), 153–167. doi:10.1002/2013JF002915.

Mertes JR, Thompson SS, Booth AD, Gulley JD and Benn DI (2017) A conceptual model of supra-glacial lake formation on debris-covered glaciers based on GPR facies analysis: GPR Facies Analysis of Spillway Lake, Ngozumpa Glacier, Nepal. *Earth Surface Processes and Landforms* 42(6), 903–914. doi:10.1002/esp.4068.

Miles ES, Steiner JF, Buri P, Immerzeel WW and Pellicciotti F (2022) Controls on the relative melt rates of debris-covered glacier surfaces. *Environmental Research Letters* 17(6), 064004. doi:10.1088/1748-9326/ac6966.

Miles KE, Hubbard B, Irvine-Fynn TDL, Miles ES, Quincey DJ and Rowan AV (2020) Hydrology of debris-covered glaciers in High Mountain Asia. *Earth-Science Reviews* 207, 103212. doi:10.1016/j.earscirev.2020.103212.

Miles KE, Hubbard B, Quincey DJ, Miles ES, Irvine-Fynn TDL and Rowan AV (2019) Surface and subsurface hydrology of debris-covered Khumbu Glacier, Nepal, revealed by dye tracing. *Earth and Planetary Science Letters* 513, 176–186. doi:10.1016/j.epsl.2019.02.020.

Miles ES and others (2018) Glacial and geomorphic effects of a supraglacial lake drainage and outburst event, Everest region, Nepal Himalaya. *The Cryosphere* 12(12), 3891–3905. doi:10.5194/tc-12-3891-2018.

Miles ES, Willis IC, Arnold NS, Steiner J and Pellicciotti F (2017) Spatial, seasonal and interannual variability of supraglacial ponds in the Langtang Valley of Nepal, 1999–2013. *Journal of Glaciology* 63(237), 88–105. doi:10.1017/jog.2016.120.

Millan R, Mouginot J, Rabatel A and Morlighem M (2022) Ice velocity and thickness of the world's glaciers. *Nature Geoscience* 15(2), 124–129. doi:10.1038/s41561-021-00885-z.

Millan R, Dehecq A, Trouve E, Gourmelen N and Berthier E (2015) Elevation changes and X-band ice and snow penetration inferred from TanDEM-X data of the Mont-Blanc area. *2015 8th International Workshop on the Analysis of Multitemporal Remote Sensing Images (Multi-Temp)*. IEEE, Annecy, France, 1–4. doi:10.1109/Multi-Temp.2015.7245753.

Milner AM and others (2017) Glacier shrinkage driving global changes in downstream systems. *Proceedings of the National Academy of Sciences* 114(37), 9770–9778. doi:10.1073/pnas.1619807114.

Mohanty LK and Maiti S (2021) Regional morphodynamics of supraglacial lakes in the Everest Himalaya. *Science of The Total Environment* 751, 141586. doi:10.1016/j.scitotenv.2020.141586.

Naito N, Nakawo M, Kadota T and Raymond CF (2000) Numerical simulation of recent shrinkage of Khumbu Glacier, Nepal Himalayas. , 11.

Narama C and others (2017) Seasonal drainage of supraglacial lakes on debris-covered glaciers in the Tien Shan Mountains, Central Asia. *Geomorphology* 286, 133–142. doi:10.1016/j.geomorph.2017.03.002.

NASA JPL (2020) NASADEM Merged DEM Global 1 arc second V001. doi:10.5067/MEASURES/NASADEM/NASADEM_HGT.001.

O'Neel S and others (2019) Reanalysis of the US Geological Survey Benchmark Glaciers: long-term insight into climate forcing of glacier mass balance. *Journal of Glaciology* 65(253), 850–866. doi:10.1017/jog.2019.66.

O'Neel S and others (2015) Icefield-to-Ocean Linkages across the Northern Pacific Coastal Temperate Rainforest Ecosystem. *BioScience* 65(5), 499–512. doi:10.1093/biosci/biv027.

O'Neill BC and others (2016) The Scenario Model Intercomparison Project (ScenarioMIP) for CMIP6. *Geoscientific Model Development* 9(9), 3461–3482. doi:10.5194/gmd-9-3461-2016.

Otsu N (1979) A Threshold Selection Method from Gray-Level Histograms. *IEEE Transactions on Systems, Man, and Cybernetics* 9(1), 62–66. doi:10.1109/TSMC.1979.4310076.

Pedregosa F and others Scikit-learn: Machine Learning in Python. *MACHINE LEARNING IN PYTHON*.

Pelto M (2019) Exceptionally High 2018 Equilibrium Line Altitude on Taku Glacier, Alaska. *Remote Sensing* 11(20), 2378. doi:10.3390/rs11202378.

Pelto M (2011) Utility of late summer transient snowline migration rate on Taku Glacier, Alaska. *The Cryosphere* 5(4), 1127–1133. doi:10.5194/tc-5-1127-2011.

Pelto MS (2010) Forecasting temperate alpine glacier survival from accumulation zone observations. *The Cryosphere* 4(1), 67–75. doi:10.5194/tc-4-67-2010.

Perry LB and others (2020) Precipitation Characteristics and Moisture Source Regions on Mt. Everest in the Khumbu, Nepal. *One Earth* 3(5), 594–607. doi:10.1016/j.oneear.2020.10.011.

Pfeffer WT and others (2014) The Randolph Glacier Inventory: a globally complete inventory of glaciers. *Journal of Glaciology* 60(221), 537–552. doi:10.3189/2014JoG13J176.

Piermattei L and others (2023) Observing glacier elevation changes from spaceborne optical and radar sensors – an inter-comparison experiment using ASTER and TanDEM-X data. doi:10.5194/egusphere-2023-2309.

Planet Team (2017) Planet Application Program Interface: In Space for Life on Earth. San Francisco, CA. https://api.planet.com.

Prieur C, Rabatel A, Thomas J-B, Farup I and Chanussot J (2022) Machine Learning Approaches to Automatically Detect Glacier Snow Lines on Multi-Spectral Satellite Images. *Remote Sensing* 14(16), 3868. doi:10.3390/rs14163868.

Pritchard HD (2019) Asia's shrinking glaciers protect large populations from drought stress. *Nature* 569(7758), 649–654. doi:10.1038/s41586-019-1240-1.

Purdie H, Gomez C and Espiner S (2015) Glacier recession and the changing rockfall hazard: Implications for glacier tourism. *New Zealand Geographer* 71(3), 189–202. doi:10.1111/nzg.12091.

Rabatel A and others (2012) Can the snowline be used as an indicator of the equilibrium line and mass balance for glaciers in the outer tropics? *Journal of Glaciology* 58(212), 1027–1036. doi:10.3189/2012JoG12J027.

Rabatel A, Dedieu J-P, Thibert E, Letréguilly A and Vincent C (2008) 25 years (1981–2005) of equilibrium-line altitude and mass-balance reconstruction on Glacier Blanc, French Alps, using remote-sensing methods and meteorological data. *Journal of Glaciology* 54(185), 307–314. doi:10.3189/002214308784886063.

Racoviteanu AE, Nicholson L, Glasser NF, Miles E, Harrison S and Reynolds JM (2022) Debris-covered glacier systems and associated glacial lake outburst flood hazards: challenges and prospects. *Journal of the Geological Society* 179(3), jgs2021-084. doi:10.1144/jgs2021-084.

Racoviteanu AE, Nicholson L and Glasser NF (2021) Surface composition of debris-covered glaciers across the Himalaya using linear spectral unmixing of Landsat 8 OLI imagery. *The Cryosphere* 15(9), 4557–4588. doi:10.5194/tc-15-4557-2021.

Racoviteanu AE, Rittger K and Armstrong R (2019) An Automated Approach for Estimating Snowline Altitudes in the Karakoram and Eastern Himalaya From Remote Sensing. *Frontiers in Earth Science* 7, 220. doi:10.3389/feart.2019.00220.

Rastner P and others (2019) On the Automated Mapping of Snow Cover on Glaciers and Calculation of Snow Line Altitudes from Multi-Temporal Landsat Data. *Remote Sensing* 11(12), 1410. doi:10.3390/rs11121410.

Reynolds JM (2000) On the formation of supraglacial lakes on debris-covered glaciers. *Debris-Covered Glaciers*. IAHS-AISH, Seattle, WA, USA, 153–161.

RGI Consortium (2023) Randolph Glacier Inventory - A Dataset of Global Glacier Outlines, Version 7. doi:10.5067/F6JMOVY5NAVZ.

RGI Consortium (2017) Randolph Glacier Inventory - A Dataset of Global Glacier Outlines, Version 6. doi:10.7265/4M1F-GD79.

Rick B, McGrath D, McCoy S and Armstrong W (2022) Decreasing hazards from glacial lakes in Alaska since the 1960s. preprint In Review. doi:10.21203/rs.3.rs-1859425/v1.

Rizzoli P and others (2017) Generation and performance assessment of the global TanDEM-X digital elevation model. *ISPRS Journal of Photogrammetry and Remote Sensing* 132, 119–139. doi:10.1016/j.isprsjprs.2017.08.008.

Rizzoli P, Martone M, Rott H and Moreira A (2017) Characterization of Snow Facies on the Greenland Ice Sheet Observed by TanDEM-X Interferometric SAR Data. *Remote Sensing* 9(4), 315. doi:10.3390/rs9040315.

Roberts-Pierel BM, Kirchner PB, Kilbride JB and Kennedy RE (2022) Changes over the Last 35 Years in Alaska's Glaciated Landscape: A Novel Deep Learning Approach to Mapping Glaciers at Fine Temporal Granularity. *Remote Sensing* 14(18), 4582. doi:10.3390/rs14184582.

Rounce DR and others (2023) Global glacier change in the 21st century: Every increase in temperature matters. *Science* 379(6627), 78–83. doi:10.1126/science.abo1324.

Rounce DR and others (2021) Distributed Global Debris Thickness Estimates Reveal Debris Significantly Impacts Glacier Mass Balance. *Geophysical Research Letters* 48(8). doi:10.1029/2020GL091311.

Rounce DR, Byers AC, Byers EA and McKinney DC (2017) Brief communication: Observations of a glacier outburst flood from Lhotse Glacier, Everest area, Nepal. *The Cryosphere* 11(1), 443–449. doi:10.5194/tc-11-443-2017.

Sakai A (2019) Brief communication: Updated GAMDAM glacier inventory over high-mountain Asia. *The Cryosphere* 13(7), 2043–2049. doi:10.5194/tc-13-2043-2019.

Sass LC, Loso MG, Geck J, Thoms EE and McGrath D (2017) Geometry, mass balance and thinning at Eklutna Glacier, Alaska: an altitude-mass-balance feedback with implications for water resources. *Journal of Glaciology* 63(238), 343–354. doi:10.1017/jog.2016.146.

Scherler D, Wulf H and Gorelick N (2018) Global Assessment of Supraglacial Debris-Cover Extents. *Geophysical Research Letters* 45(21). doi:10.1029/2018GL080158.

Shea JM, Menounos B, Moore RD and Tennant C (2013) An approach to derive regional snow lines and glacier mass change from MODIS imagery, western North America. *The Cryosphere* 7(2), 667–680. doi:10.5194/tc-7-667-2013.

Shean DE, Bhushan S, Montesano P, Rounce DR, Arendt A and Osmanoglu B (2020) A Systematic, Regional Assessment of High Mountain Asia Glacier Mass Balance. *Frontiers in Earth Science* 7, 363. doi:10.3389/feart.2019.00363.

Shugar DH and others (2021) A massive rock and ice avalanche caused the 2021 disaster at Chamoli, Indian Himalaya. *Science* 373(6552), 300–306. doi:10.1126/science.abh4455.

Shugar DH and others (2020) Rapid worldwide growth of glacial lakes since 1990. *Nature Climate Change* 10(10), 939–945. doi:10.1038/s41558-020-0855-4.

Steiner JF, Buri P, Miles ES, Ragettli S and Pellicciotti F (2019) Supraglacial ice cliffs and ponds on debris-covered glaciers: spatio-temporal distribution and characteristics. *Journal of Glaciology* 65(252), 617–632. doi:10.1017/jog.2019.40.

Stoffel M and Huggel C (2012) Effects of climate change on mass movements in mountain environments. *Progress in Physical Geography: Earth and Environment* 36(3), 421–439. doi:10.1177/0309133312441010.

Taylor CJ, Carr JR and Rounce DR (2022) Spatiotemporal supraglacial pond and ice cliff changes in the Bhutan–Tibet border region from 2016 to 2018. *Journal of Glaciology* 68(267), 101–113. doi:10.1017/jog.2021.76.

Trüssel BL, Motyka RJ, Truffer M and Larsen CF (2013) Rapid thinning of lake-calving Yakutat Glacier and the collapse of the Yakutat Icefield, southeast Alaska, USA. *Journal of Glaciology* 59(213), 149–161. doi:10.3189/2013J0G12J081.

U.S. Geological Survey Benchmark Glacier Program and others (2016) Glacier-Wide Mass Balance and Compiled Data Inputs. doi:10.5066/F7HD7SRF.

Veh G, Korup O and Walz A (2020) Hazard from Himalayan glacier lake outburst floods. *Proceedings of the National Academy of Sciences* 117(2), 907–912. doi:10.1073/pnas.1914898117.

Wang X and others (2020) Glacial lake inventory of high-mountain Asia in 1990 and 2018 derived from Landsat images. *Earth System Science Data* 12(3), 2169–2182. doi:10.5194/essd-12-2169-2020.

Watanabe T, Lamsal D and Ives JD (2009) Evaluating the growth characteristics of a glacial lake and its degree of danger of outburst flooding: Imja Glacier, Khumbu Himal, Nepal. *Norsk Geografisk Tidsskrift - Norwegian Journal of Geography* 63(4), 255–267. doi:10.1080/00291950903368367.

Watson CS, King O, Miles ES and Quincey DJ (2018) Optimising NDWI supraglacial pond classification on Himalayan debris-covered glaciers. *Remote Sensing of Environment* 217, 414–425. doi:10.1016/j.rse.2018.08.020.

Watson CS, Quincey DJ, Carrivick JL, Smith MW, Rowan AV and Richardson R (2018) Heterogeneous water storage and thermal regime of supraglacial ponds on debris-covered glaciers: Water storage and thermal regime of supraglacial ponds. *Earth Surface Processes and Landforms* 43(1), 229–241. doi:10.1002/esp.4236.

Watson CS, Quincey DJ, Carrivick JL and Smith MW (2016) The dynamics of supraglacial ponds in the Everest region, central Himalaya. *Global and Planetary Change* 142, 14–27. doi:10.1016/j.gloplacha.2016.04.008.

Welling JT, Árnason Þ and Ólafsdottír R (2015) Glacier tourism: a scoping review. *Tourism Geographies* 17(5), 635–662. doi:10.1080/14616688.2015.1084529.

Wendleder A, Schmitt A, Erbertseder T, D'Angelo P, Mayer C and Braun MH (2021) Seasonal Evolution of Supraglacial Lakes on Baltoro Glacier From 2016 to 2020. *Frontiers in Earth Science* 9, 725394. doi:10.3389/feart.2021.725394.

Wouters B, Gardner AS and Moholdt G (2019) Global Glacier Mass Loss During the GRACE Satellite Mission (2002-2016). *Frontiers in Earth Science* 7, 96. doi:10.3389/feart.2019.00096.

Xu H (2006) Modification of normalised difference water index (NDWI) to enhance open water features in remotely sensed imagery. *International Journal of Remote Sensing* 27(14), 3025–3033. doi:10.1080/01431160600589179.

Zandler H, Haag I and Samimi C (2019) Evaluation needs and temporal performance differences of gridded precipitation products in peripheral mountain regions. *Scientific Reports* 9(1), 15118. doi:10.1038/s41598-019-51666-z.

Zekollari H, Huss M and Farinotti D (2020) On the Imbalance and Response Time of Glaciers in the European Alps. *Geophysical Research Letters* 47(2), e2019GL085578. doi:10.1029/2019GL085578.

Zeller L, McGrath D, Sass L, Florentine C, and Downs J (2024a) Equilibrium line altitudes, accumulation areas, and the vulnerability of glaciers in Alaska. *Journal of Glaciology*

Zeller L, McGrath D, McCoy SW and Jacquet J (2024b) Seasonal to decadal dynamics of supraglacial lakes on debris-covered glaciers in the Khumbu region, Nepal. *The Cryosphere* 18(2), 525–541. doi:10.5194/tc-18-525-2024.

Zeller L, McGrath D, Sass L, Florentine C, and Downs J (2024c) Annual End-of-Summer Snow Cover on Glaciers in Alaska and Northwest Canada: U.S. Geological Survey data release (doi: 10.5066/P1QHST6F)

Zeller L, McGrath D, Sass L, O'Neel S, McNeil C and Baker E (2023) Beyond glacier-wide mass balances: parsing seasonal elevation change into spatially resolved patterns of accumulation and ablation at Wolverine Glacier, Alaska. *Journal of Glaciology* 69(273), 87–102. doi:10.1017/jog.2022.46.

Zemp M and others (2019) Global glacier mass changes and their contributions to sea-level rise from 1961 to 2016. *Nature* 568(7752), 382–386. doi:10.1038/s41586-019-1071-0.

Zemp M, Hoelzle M and Haeberli W (2009) Six decades of glacier mass-balance observations: a review of the worldwide monitoring network. *Annals of Glaciology* 50(50), 101–111. doi:10.3189/172756409787769591.

Zhang G and others (2023) Underestimated mass loss from lake-terminating glaciers in the greater Himalaya. *Nature Geoscience* 16(4), 333–338. doi:10.1038/s41561-023-01150-1.

Zhu Z, Wang S and Woodcock CE (2015) Improvement and expansion of the Fmask algorithm: cloud, cloud shadow, and snow detection for Landsats 4–7, 8, and Sentinel 2 images. *Remote Sensing of Environment* 159, 269–277. doi:10.1016/j.rse.2014.12.014.

Zupanc A (2017) Improving Cloud Detection with Machine Learning. https://medium.com/sentinel-hub/improving-cloud-detection-with-machine-learning-c09dc5d7cf13.

APPENDIX A: SUPPLEMENT TO CHAPTER 1

Table A1: The list of all features (bands) used in the random forest classifier. For each row, values from the top-of-atmosphere reflectance of the image, the value from the snow-on mosaic, and the image reflectance divided by the snow-on mosaic were used.

Feature	**Description**
Coastal (raw, snow-on, normalized)	Band 1 in Sentinel-2 TOA reflectance product
Blue (raw, snow-on, normalized)	Band 2 in Sentinel-2 TOA reflectance product
Green (raw, snow-on, normalized)	Band 3 in Sentinel-2 TOA reflectance product
Red (raw, snow-on, normalized)	Band 4 in Sentinel-2 TOA reflectance product
Red_edge_1 (raw, snow-on, normalized)	Band 5 in Sentinel-2 TOA reflectance product
Red_edge_2 (raw, snow-on, normalized)	Band 6 in Sentinel-2 TOA reflectance product
Red_edge_3 (raw, snow-on, normalized)	Band 7 in Sentinel-2 TOA reflectance product
Red_edge_4 (raw, snow-on, normalized)	Band 8a in Sentinel-2 TOA reflectance product
NIR (raw, snow-on, normalized)	Band 8 in Sentinel-2 TOA reflectance product
Vapor (raw, snow-on, normalized)	Band 9 in Sentinel-2 TOA reflectance product
SWIR_1 (raw, snow-on, normalized)	Band 11 in Sentinel-2 TOA reflectance product
SWIR_2 (raw, snow-on, normalized)	Band 12 in Sentinel-2 TOA reflectance product
NDSI (raw, snow-on, normalized)	Normalized difference snow index, calculated as the normalized difference between SWIR 1 and Green bands
NDWI (raw, snow-on, normalized)	Normalized difference water index, calculated as the normalized difference between the NIR and Green bands

Table A2: The modern and future ELA and AAR of each region within this study. Values for the entire study are (region '"All"), O2 subregions, and O3 subregions are included. Modern AAR values are provided both at the AAR found from two-dimensional average snow cover maps as well as the AAR found using the hypsometric method.

Region	Modern ELA (m)	Modern AAR	Modern AAR (hypsometric)	Future ELA (m)	Future AAR (hypsometric)
All	1750	0.41	0.44	1936	0.33
O2-02	1880	0.37	0.39	2025	0.28
O2-03	1410	0.26	0.26	1560	0.14
O2-04	1380	0.39	0.43	1521	0.3
O2-05	2040	0.45	0.48	2160	0.42
O2-06	1750	0.4	0.44	1968	0.24
O3-01	1410	0.26	0.26	1560	0.14
O3-02	1482	0.31	0.33	1658	0.14
O3-03	1840	0.31	0.33	1998	0.23
O3-04	1830	0.33	0.34	1966	0.27
O3-05	2040	0.3	0.34	2166	0.25
O3-06	2380	0.49	0.51	2522	0.41
O3-07	2015	0.38	0.41	2137	0.21
O3-08	1198	0.41	0.48	1330	0.3
O3-09	1170	0.41	0.47	1301	0.3
O3-10	1530	0.38	0.41	1667	0.31
O3-11	1844	0.35	0.37	2000	0.3
O3-12	2160	0.48	0.51	2262	0.45
O3-13	1464	0.38	0.41	1640	0.29
O3-14	1660	0.48	0.52	1882	0.27
O3-15	1820	0.42	0.45	2064	0.22
O3-16	1800	0.28	0.3	2030	0.08

Table A3: The ELA and AAR of each region in each of the five study years.

Region	ELA 2018 (m)	AAR 2018	ELA 2019 (m)	AAR 2019	ELA 2020 (m)	AAR 2020	ELA 2021 (m)	AAR 2021	ELA 2022 (m)	AAR 2022
All	1800	0.37	1940	0.25	1660	0.45	1568	0.49	1660	0.47
O2-02	1755	0.43	2140	0.24	1860	0.38	1860	0.39	1815	0.39
O2-03	1375	0.25	1275	0.31	1430	0.23	1090	0.39	1370	0.26
O2-04	1410	0.38	1496	0.27	1363	0.4	1320	0.45	1200	0.49
O2-05	2010	0.42	2160	0.31	1966	0.49	1915	0.49	1932	0.51
O2-06	1870	0.26	1960	0.15	1640	0.47	1480	0.58	1670	0.48
O3-01	1375	0.25	1275	0.31	1430	0.23	1090	0.39	1370	0.26
O3-02	1453	0.38	1540	0.27	1530	0.26	1440	0.38	1460	0.34
O3-03	1700	0.39	2148	0.21	1940	0.28	1770	0.34	1759	0.36
O3-04	1720	0.38	2073	0.22	1832	0.32	1760	0.36	1780	0.35
O3-05	1900	0.39	2424	0.12	1930	0.38	2142	0.26	2005	0.33
O3-06	2250	0.55	2686	0.31	2260	0.54	2390	0.5	2387	0.5
O3-07	1910	0.55	2350	0.02	1965	0.42	2035	0.38	1960	0.5
O3-08	1208	0.4	1262	0.32	1270	0.38	1030	0.51	1035	0.49
O3-09	1170	0.42	1280	0.32	1220	0.38	1070	0.49	860	0.58
O3-10	1581	0.36	1702	0.25	1460	0.41	1470	0.42	1391	0.47
O3-11	1850	0.32	1928	0.24	1725	0.39	1788	0.37	1665	0.41
O3-12	2134	0.45	2310	0.33	2071	0.52	2070	0.53	2086	0.53
O3-13	1660	0.24	1834	0.12	1374	0.41	1160	0.56	1280	0.51
O3-14	1762	0.34	1950	0.17	1580	0.55	1430	0.62	1640	0.53
O3-15	1930	0.25	2010	0.2	1710	0.5	1570	0.59	1760	0.48
O3-16	1920	0.17	1980	0.1	1680	0.39	1540	0.55	1760	0.32

APPENDIX B: SUPPLEMENT TO CHAPTER 2

B1. Planet: Data access and cleanup

Imagery covering the AOI was searched for and downloaded using the Planet Orders API (Planet Team 2017). For each glacier, I selected images that (1) captured the entire glacier extent, (2) had less than 15% cloud cover across the entire image, and (3) contained four-band (RGB and near-infrared (NIR)), ortho-rectified, surface-reflectance data (the "ortho_analytic_4b_sr" asset type). I additionally included pairs of images which were taken by the same satellite on the same day that, when combined, captured the entire glacier surface and each met criteria (2) and (3). A full list of all images meeting these criteria was compiled for the eight study glaciers. The 'harmonize' tool was used when ordering these images using the Planet Orders API. This tool brings the spectral response of each image in line with coincident Sentinel-2 imagery, ensuring a consistent spectral response across the multitude of individual sensors.

This entire image collection was downloaded to a local computer for additional processing and lake identification. For each glacier, images were merged together (if needed) and then clipped to the AOI extent. Each image was then manually inspected to ensure suitable data quality. Images with considerable cloud cover or snow cover, anomalous spectral responses, or poor band coregistration were discarded.

Areas of cloud cover and terrain shadows were identified in each image and excluded from future analysis. Cloud-covered areas were classified using the Planet-provided usable data mask. I developed an approach to identify terrain shadows within PlanetScope images as dark, spatially-continuous areas (described in detail below).

B2. Planet: Shadow masking

A novel texture-based approach was developed to identify and mask out terrain shadowing in PlanetScope images. Shadows were identified on the glacier surface as large, continuous areas that were dark and had little spatial variation in brightness. These areas were identified using a multi-step process. First, areas of very high confidence shadow (shadow "seeds") were identified. These were identified if it met the following criteria:

1. The average surface brightness in visible bands was less than 1000 (using the image digital numbers).
2. At least 75% of on-glacier pixels within 99 meters had surface brightness less than 1000
3. The standard deviation of surface brightness of pixels within 99 meters was less than 50

These areas of shadow seeds were then iteratively expanded to include the continuous regions surrounding them with pixel brightness below the 1000 DN threshold in visible bands, with small voids and gaps filled.

B3. Planet: Filtering and smoothing

A pixel-wise temporal smoothing algorithm was applied to the initial water classification images to prevent individual pixels from rapidly switching between being classified as water and non-water. For each pixel, I collated the time series of all observations across the 2017–2022 period. Individual observations were assigned a value of 1 if the pixel was identified as water and 0 if it was not. A Gaussian filter was then applied to this time series, using a Gaussian kernel with a standard deviation of 14 days. For each point, if the resulting smoothed value was greater than or equal to 50% of the potential maximum value (the value it would be if all observations were initially classified as water) then that pixel in that image was given a "smoothed" classification of water. All other observations were classified as non-water. The products at the end of this smoothing process (Figure 15d, Temporally Smoothed Water) represent the spatiotemporal distribution of unfrozen SGLs.

The temporally smoothed water products were then used to further constrain the classification of frozen lake surfaces (Figure 15d, Spatiotemporal Ice Masking). Each pixel which was initially classified as lake ice remained as a lake ice pixel only if it was also classified as water at any point within the preceding or following 60 days (resulting in the Filtered Ice product). This limited the misclassification of snow drifts and ice cliffs as SGLs.

Finally, the filtered ice dataset was combined with the temporally smoothed water dataset, and the same Gaussian temporal smoothing was applied to this combined dataset, resulting in the final lake extent dataset. This provides the extent of all lakes, including frozen and unfrozen, within each image.

B4. Landsat Glacier Ice Masking

Continuously exposed areas of glacier ice in Landsat images were identified using thresholding on the normalized difference snow index (NDSI) and blue band surface reflectance.

As a first step, areas of snow/ice were identified as pixels with an NDSI value greater than 0.2 and blue reflectance greater than 0.35. In order to avoid mis-classifying temporary snow cover, ice cliffs, or frozen lake surfaces as glacier ice I then applied a temporal smoothing to these products. For each Landsat image, pixels were given a final classification of glacier ice if that pixel was identified as ice using the aforementioned thresholds in greater than 60% of all Landsat images captured within the surrounding four years (two years before and after). These final glacier ice extents were then excluded from being classified as water. A final filtering step was also applied to remove occasional linear artifacts in Landsat 5 near-infrared bands. Pixels where the difference between the green and near infrared reflectance (green minus near-infrared) was greater than 0.2 were masked out and not included in the analysis.

B5. Supplementary tables

Table B1: Physical characteristics of each of the eight glaciers investigated. Note that all columns, other than "Total Glacier Size" refer to only the areas of investigation (AOI) used in this study. Ice flow velocities are given by the mean plus/minus one standard deviation. Note that Imja and Lhotse Shar (*) are considered a single glacier in RGI 6.0 (RGI Consortium, 2017). Debris thicknesses were taken from Rounce and others (2021), and flow velocities were taken from NASA ITS_LIVE velocity mosaics

Glacier	Debris-covered Area (km^2, within AOI)	Total Glacier Size (km^2, RGI 6.0)	Glacier Length (km, within AOI)	Average debris thickness (m, within AOI)	Flow velocity (m yr^{-1}, within AOI)
Ama Dablam	2.23	4.82	3.87	1.04	0.76 ±0.96
Ambulapcha	0.91	1.92	1.72	0.51	0.82 ±0.40
Imja	1.01	14.27*	1.59	0.20	1.38 ±1.39
Khumbu	5.74	19.10	8.09	0.82	1.53 ±2.97
Lhotse	5.21	6.83	5.81	0.13	3.30 ±6.06
Lhotse Nup	1.60	2.84	3.54	0.44	1.02 ±1.25
Lhotse Shar	3.21	14.27*	3.41	0.43	3.35 ±4.40
Nuptse	2.77	3.69	5.20	0.33	3.05 ±4.07

Table B2: Number of images for each glacier from each source, after manual filtering of images with cloud cover, snow cover, or poor image quality.

Glacier	Planet	Landsat 5	Landsat 7	Landsat 8	Landsat 9	Sentinel-2
Pre-filtering		**324**	**394**	**204**	**20**	**288**
Ama Dablam	**495**	**148**	**174**	**91**	**6**	**83**
Ambulapcha	**467**	**139**	**169**	**98**	**10**	**95**
Imja	**411**	**167**	**190**	**113**	**12**	**111**
Khumbu	**306**	**174**	**0**	**104**	**9**	**108**
Lhotse	**371**	**153**	**181**	**89**	**10**	**101**
Lhotse Nup	**468**	**162**	**209**	**97**	**12**	**112**
Lhotse Shar	**338**	**160**	**183**	**96**	**13**	**116**
Nuptse	**422**	**160**	**173**	**92**	**9**	**115**

Table B3: Error statistics for Landsat and Sentinel-2 SGL identification on each glacier. Presented as the median per-image difference in SGL area across all validation imagery for each glacier (MAE, in m^2), and then normalized by image-specific SGL (as %). Bias is computed by subtracting Landsat/Sentinel-2 derived SGL area from PlanetScope-derived area.

	Landsat 7 & 8		Sentinel-2	
Glacier	**MAE (m^2 and %)**	**Bias (m^2 and %)**	**MAE (m^2 and %)**	**Bias (m^2 and %)**
Ama Dablam	**4752 (49.7%)**	**-207 (-1.3%)**	**2915 (26.3%)**	**648 (4.1%)**
Ambulapcha	**1994 (21.2%)**	**-572 (-4.3%)**	**2505 (13.0%)**	**-1996 (-11.4%)**
Imja	**940 (100.0%)**	**-828 (-61.7%)**	**264 (59.9%)**	**-233 (-23.2%)**
Khumbu	**31797 (19.8%)**	**-22950 (-14.2%)**	**48391 (30.7%)**	**-48391 (-30.1%)**
Lhotse	**11475 (19.2%)**	**4149 (+4.4%)**	**17441 (25.7%)**	**-5562 (-6.1%)**
Lhotse Nup	**3285 (55.1%)**	**-3285 (-36.8%)**	**2223 (38.1%)**	**-1371 (-19.7%)**
Lhotse Shar	**11016 (36.8%)**	**-10809 (-28.1%)**	**14422 (44.0%)**	**-12512 (-31.5%)**
Nuptse	**10143 (35.6%)**	**-10143 (-30.8%)**	**11345 (40.1%)**	**-11345 (-40.7%)**
Overall	**5436 (36.8%)**	**-2079 (-23.6%)**	**5796 (34.3%)**	**-2618 (-21.6%)**

Table B4: Lake number and area minimums (min.) and maximums (max.) for each glacier in 2018.

Glacier	2018 min. (#)	2018 max. (#)	2018 min. (area)	2018 max (area)
Ama Dablam	**18**	**72**	**22563**	**57555**
Ambulapcha	**4**	**35**	**9081**	**35658**
Imja	**4**	**23**	**612**	**4464**
Khumbu	**176**	**646**	**162414**	**268362**
Lhotse	**82**	**402**	**74124**	**204399**
Lhotse Nup	**17**	**65**	**9189**	**22626**
Lhotse Shar	**44**	**272**	**26739**	**91449**
Nuptse	**33**	**125**	**34047**	**59337**

Table B5: Lake number and area minimums (min.) and maximums (max.) for each glacier in 2019.

Glacier	2019 min. (#)	2019 max. (#)	2019 min. (area)	2019 max (area)
Ama Dablam	**31**	**85**	**29016**	**54441**
Ambulapcha	**6**	**42**	**17244**	**35739**
Imja	**3**	**18**	**549**	**4455**
Khumbu	**157**	**690**	**163863**	**363519**
Lhotse	**86**	**399**	**128691**	**207162**
Lhotse Nup	**18**	**67**	**10494**	**22554**
Lhotse Shar	**43**	**285**	**28710**	**69687**
Nuptse	**34**	**118**	**35406**	**48906**

Table B6: Lake number and area minimums (min.) and maximums (max.) for each glacier in 2020.

Glacier	2020 min. (#)	2020 max. (#)	2020 min. (area)	2020 max (area)
Ama Dablam	**30**	**92**	**14382**	**36279**
Ambulapcha	**12**	**64**	**17262**	**55755**
Imja	**1**	**31**	**855**	**6498**
Khumbu	**165**	**572**	**183492**	**275481**
Lhotse	**103**	**442**	**54405**	**172557**
Lhotse Nup	**14**	**97**	**4131**	**29007**
Lhotse Shar	**48**	**318**	**29547**	**97596**
Nuptse	**30**	**138**	**33264**	**84213**

Table B7: Lake number and area minimums (min.) and maximums (max.) for each glacier in 2021.

Glacier	2021 min. (#)	2021 max. (#)	2021 min. (area)	2021 max (area)
Ama Dablam	**10**	**73**	**7641**	**49788**
Ambulapcha	**9**	**33**	**20304**	**36405**
Imja	**0**	**18**	**0**	**2448**
Khumbu	**115**	**405**	**164619**	**436536**
Lhotse	**79**	**292**	**63693**	**276912**
Lhotse Nup	**9**	**54**	**3465**	**14625**
Lhotse Shar	**45**	**188**	**26190**	**171522**
Nuptse	**22**	**112**	**32526**	**82215**

Table B8: Lake number and area minimums (min.) and maximums (max.) for each glacier in 2022.

Glacier	2022 min. (#)	2022 max. (#)	2022 min. (area)	2022 max (area)
Ama Dablam	**40**	**112**	**23940**	**51534**
Ambulapcha	**18**	**44**	**27927**	**46323**
Imja	**3**	**26**	**729**	**5076**
Khumbu	**218**	**563**	**223605**	**306729**
Lhotse	**120**	**340**	**94023**	**170064**
Lhotse Nup	**29**	**82**	**7803**	**34578**
Lhotse Shar	**64**	**242**	**22626**	**85770**
Nuptse	**39**	**138**	**45765**	**66618**

Table B9: Long-term trends in SGL area on each glacier, as seen in Landsat-derived SGL products. Trends are presented as the lake area change per year from linear regression analysis of the entire timeframe (1988-2022) as well as only for the 2013-2022 period. Results are further broken down by glacier-wide lake area trends near-terminus (lower 50% by distance from terminus) trends. P-values are provided for each.

Glacier	Full Glacier 1988–2022 m^2 yr^{-1} (P-value)	Full Glacier 2013–2022 m^2 yr^{-1} (P-value)	Terminus only 1988–2022 m^2 yr^{-1} (P-value)	Terminus only 2013–2022 m^2 yr^{-1} (P-value)
Ama Dablam	**128 (0.355)**	**-1156 (0.117)**	**34 (0.587)**	**-1143 (0.025)**
Ambulapcha	**294 (0.000)**	**687 (0.204)**	**249 (0.000)**	**1135 (0.003)**
Imja	**-109 (0.004)**	**25 (0.500)**	**-112 (0.001)**	**0 (1.000)**
Khumbu	**2413 (0.000)**	**8348 (0.001)**	**2678 (0.000)**	**12745 (0.000)**
Lhotse	**-192 (0.740)**	**2212 (0.302)**	**382 (0.152)**	**5408 (0.002)**
Lhotse Nup	**-118 (0.107)**	**-104 (0.757)**	**-15 (0.587)**	**-155 (0.340)**
Lhotse Shar	**-1971 (0.001)**	**-1860 (0.194)**	**-258 (0.025)**	**-286 (0.538)**
Nuptse	**155 (0.227)**	**674 (0.271)**	**329 (0.000)**	**1045 (0.084)**

B6. Supplementary figures

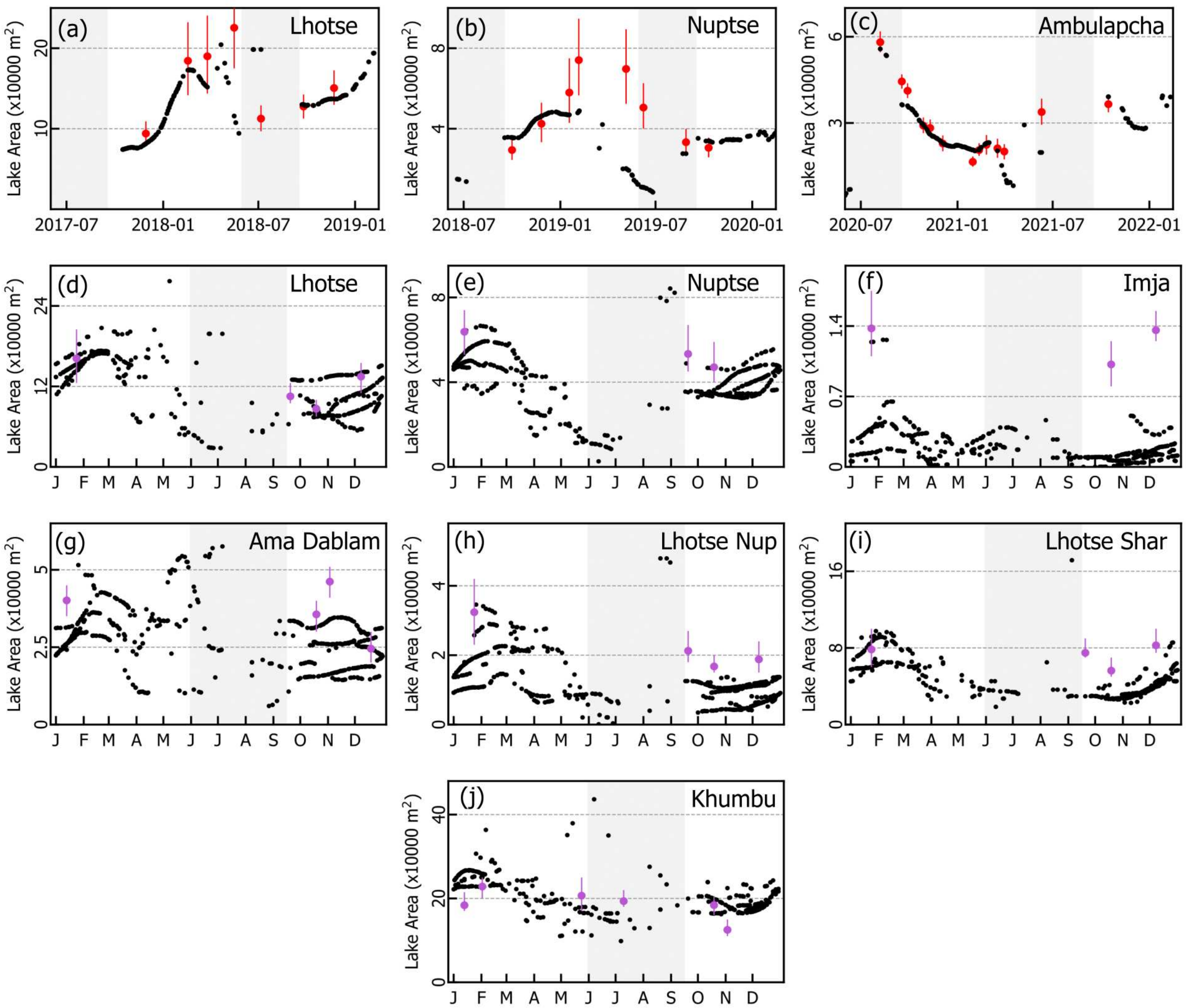

Figure B1: (a-c) A comparison of automated lake areas (black dots) to the manually-delineated validation images on Lhotse, Nuptse, and Ambulapcha Glaciers (red). (d-j) Comparison between automated lake areas and results from Watson and others (2016, purple). Comparisons with Watson and others are presented with results plotted by day of year (tick labels indicating the beginning of each month), as there was no temporal overlap between my observations and theirs. Grey shaded areas indicate monsoon months. Red and purple bars indicate error estimates from a ±1 pixel buffering.

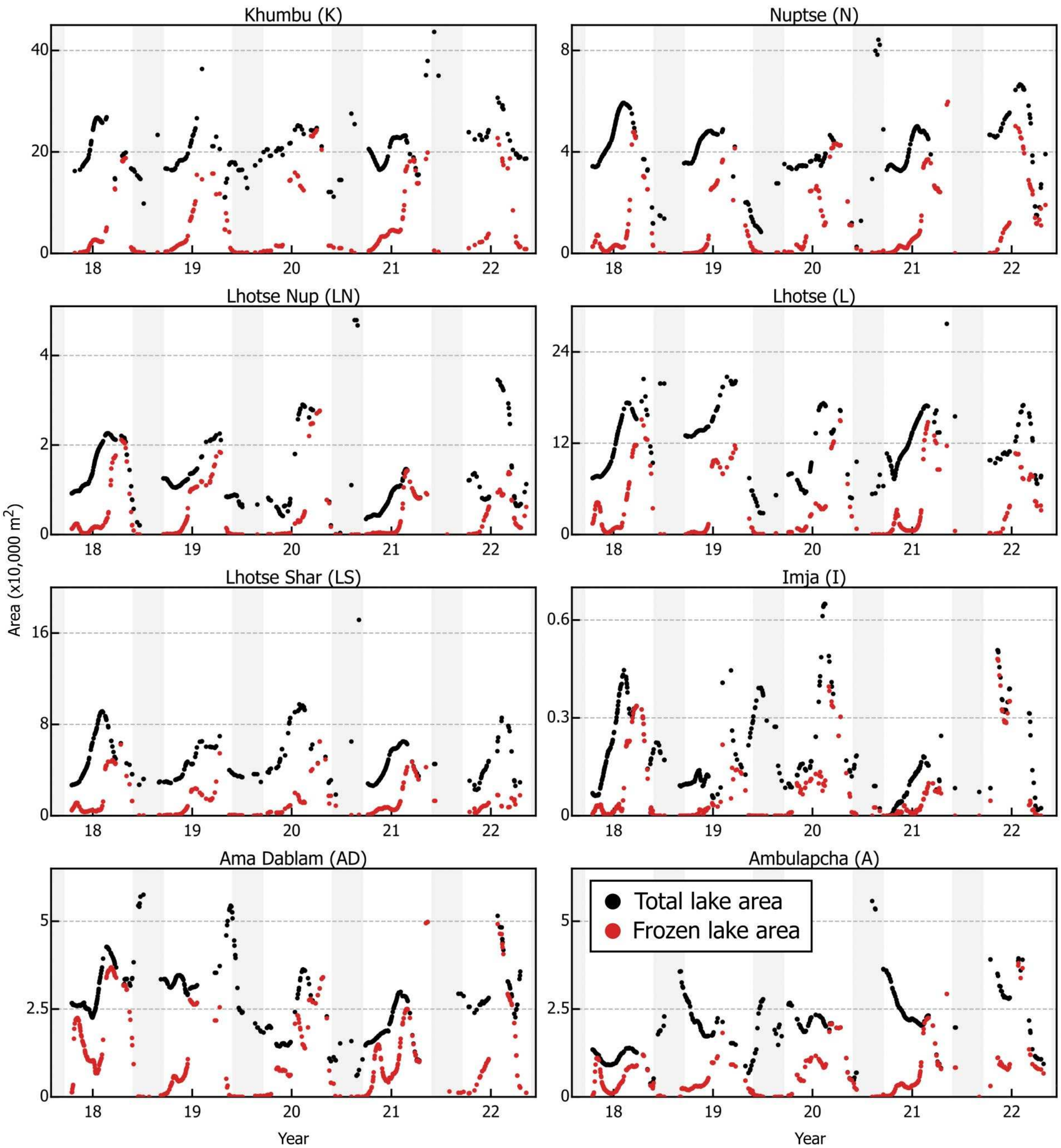

Figure B2: Comparison of the timeseries of total lake area (black points) and the total area of lake surface which are frozen (red points) for each glacier across the five-year study period.

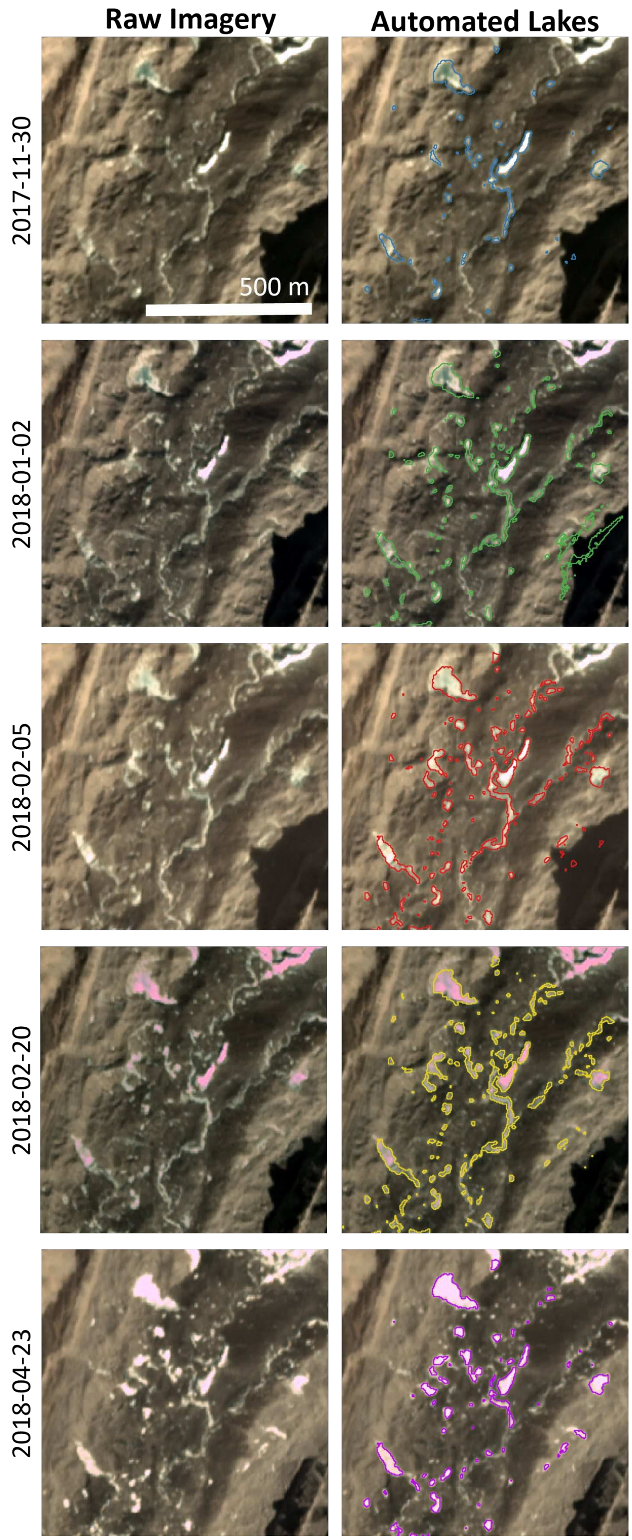

Figure B3: An example of the SGL changes in the upper region of Khumbu Glacier between November 2017 and April 2018. Outlines show the automated SGL identification.

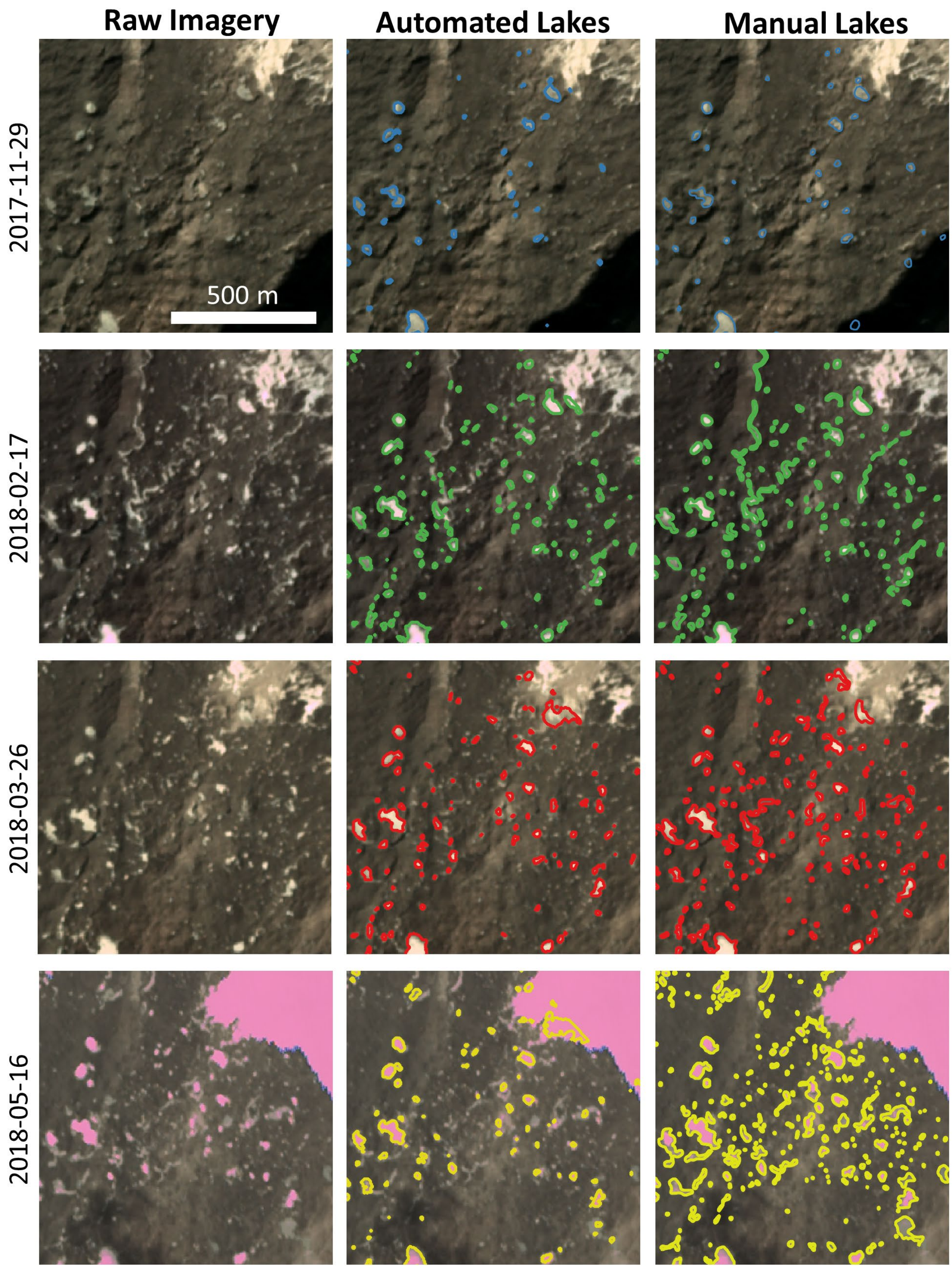

Figure B4: An example of the SGL changes in the upper region of Lhotse Glacier between November 2017 and May 2018. Center outlines show the automated SGL identification, left outlines show the manual validation dataset outlines.

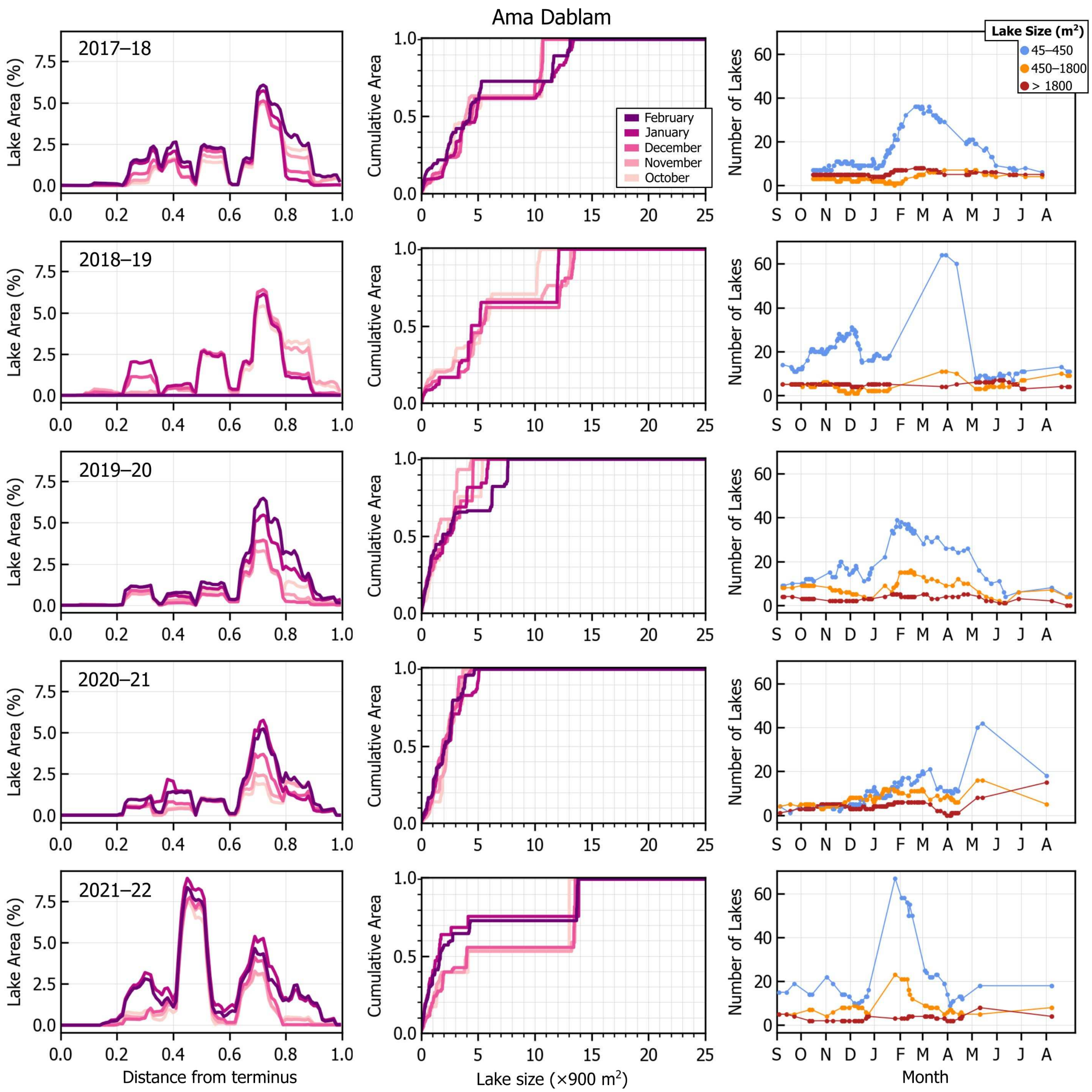

Figure B5: Seasonality in lake area and count on Ama Dablam Glacier, presented identically as Figure 20.

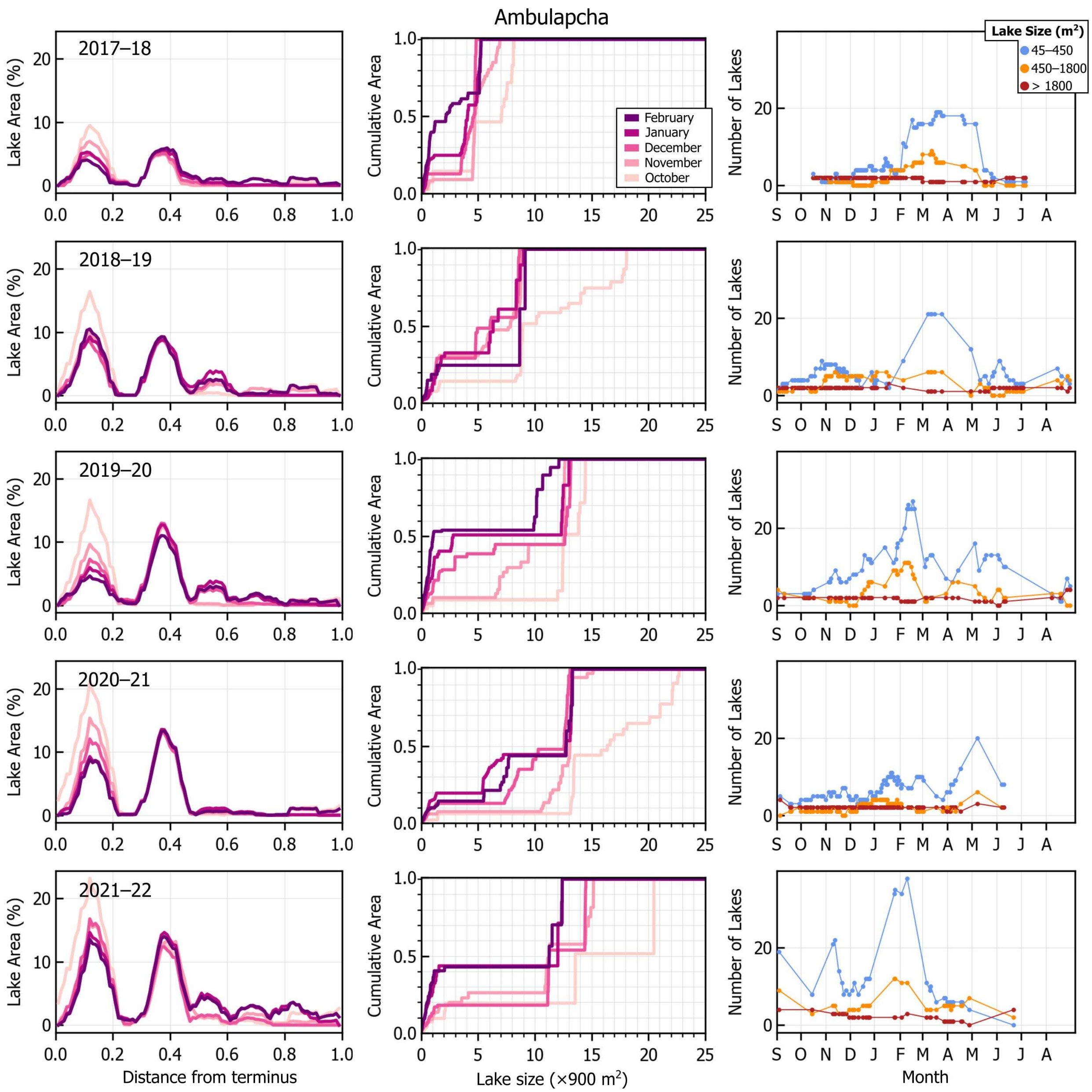

Figure B6: Seasonality in lake area and count on Ambulapcha Glacier, presented identically as Figure 20.

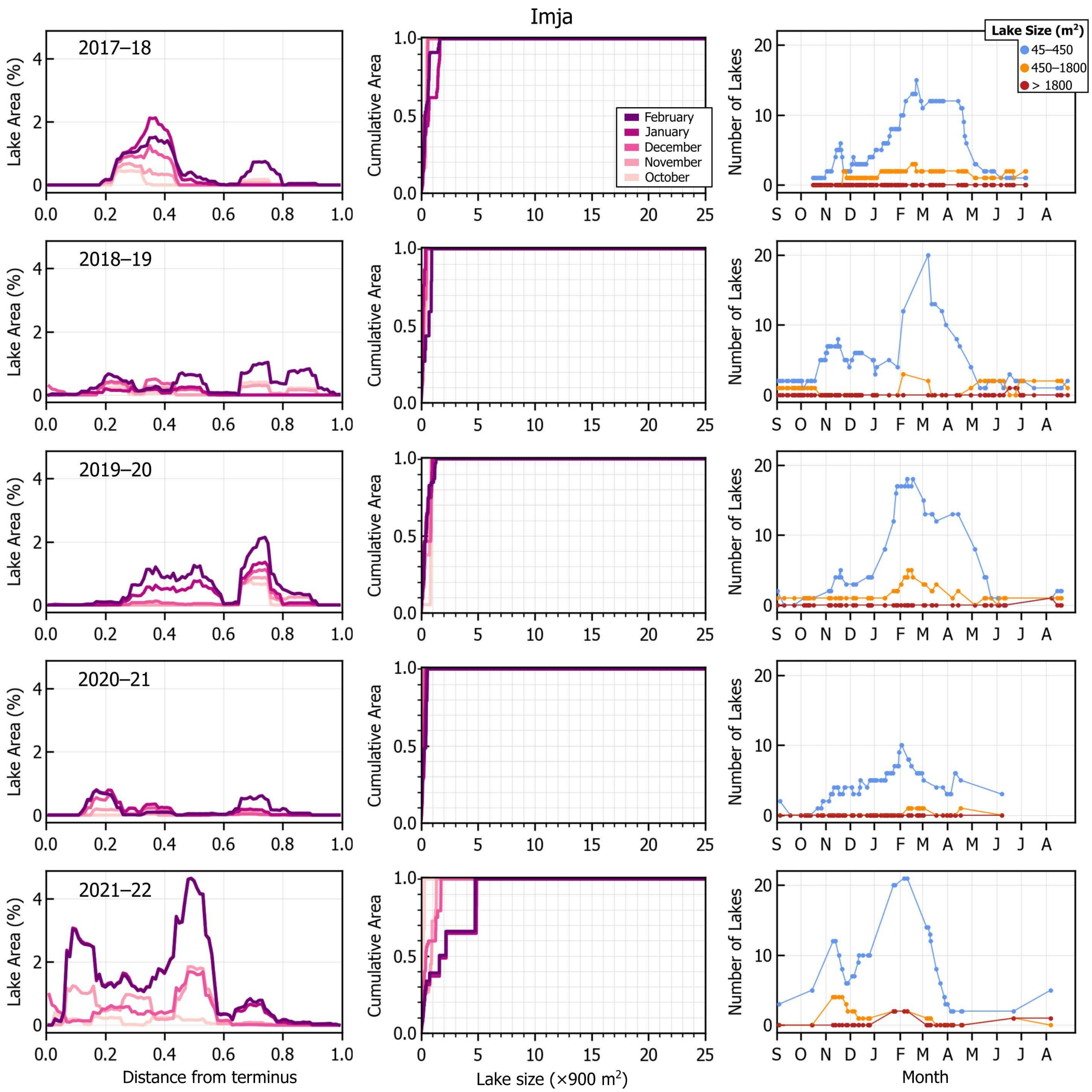

Figure B7: Seasonality in lake area and count on Imja Glacier, presented identically as Figure 20.

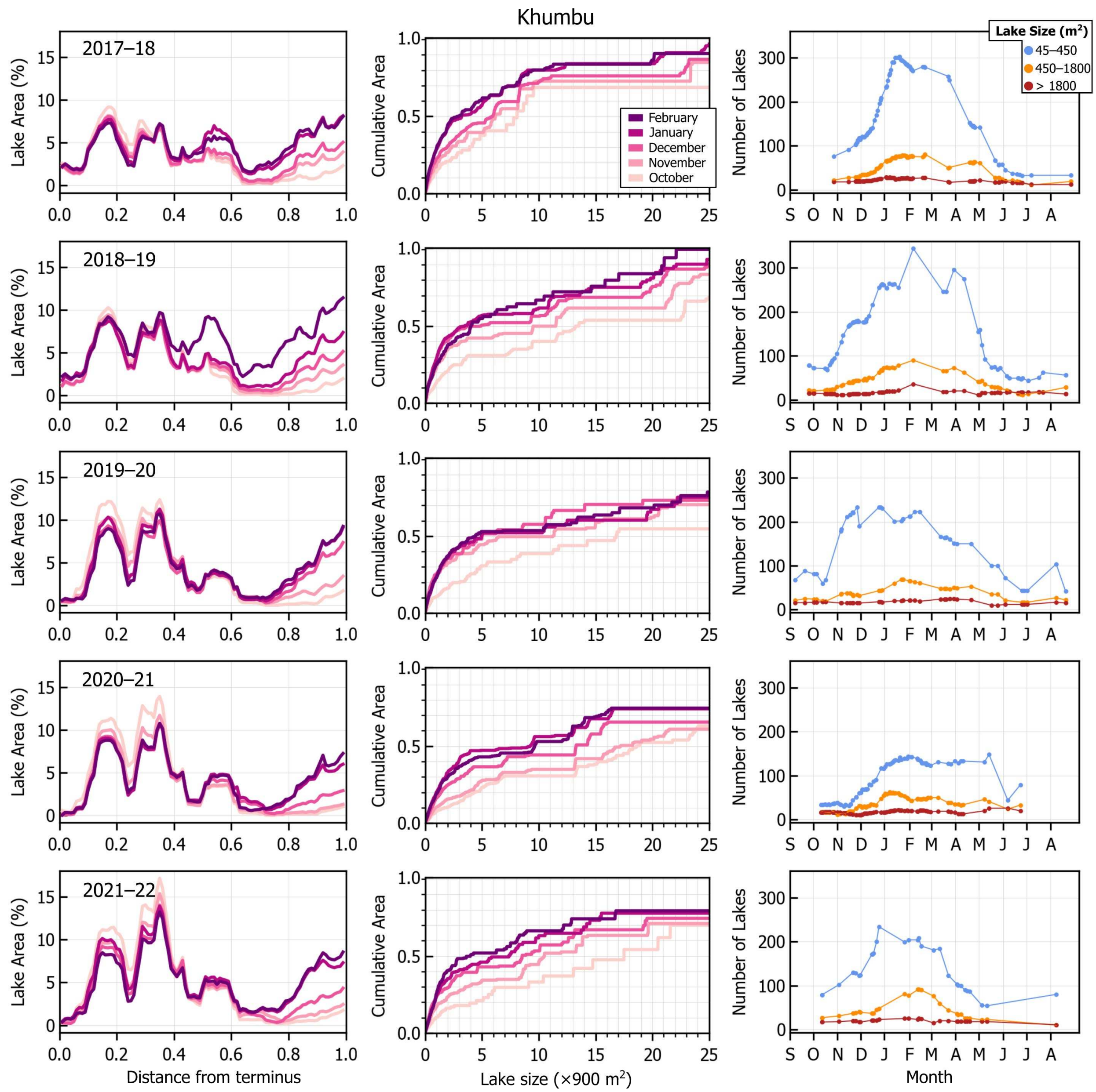

Figure B8: Seasonality in lake area and count on Khumbu Glacier, presented identically as Figure 20.

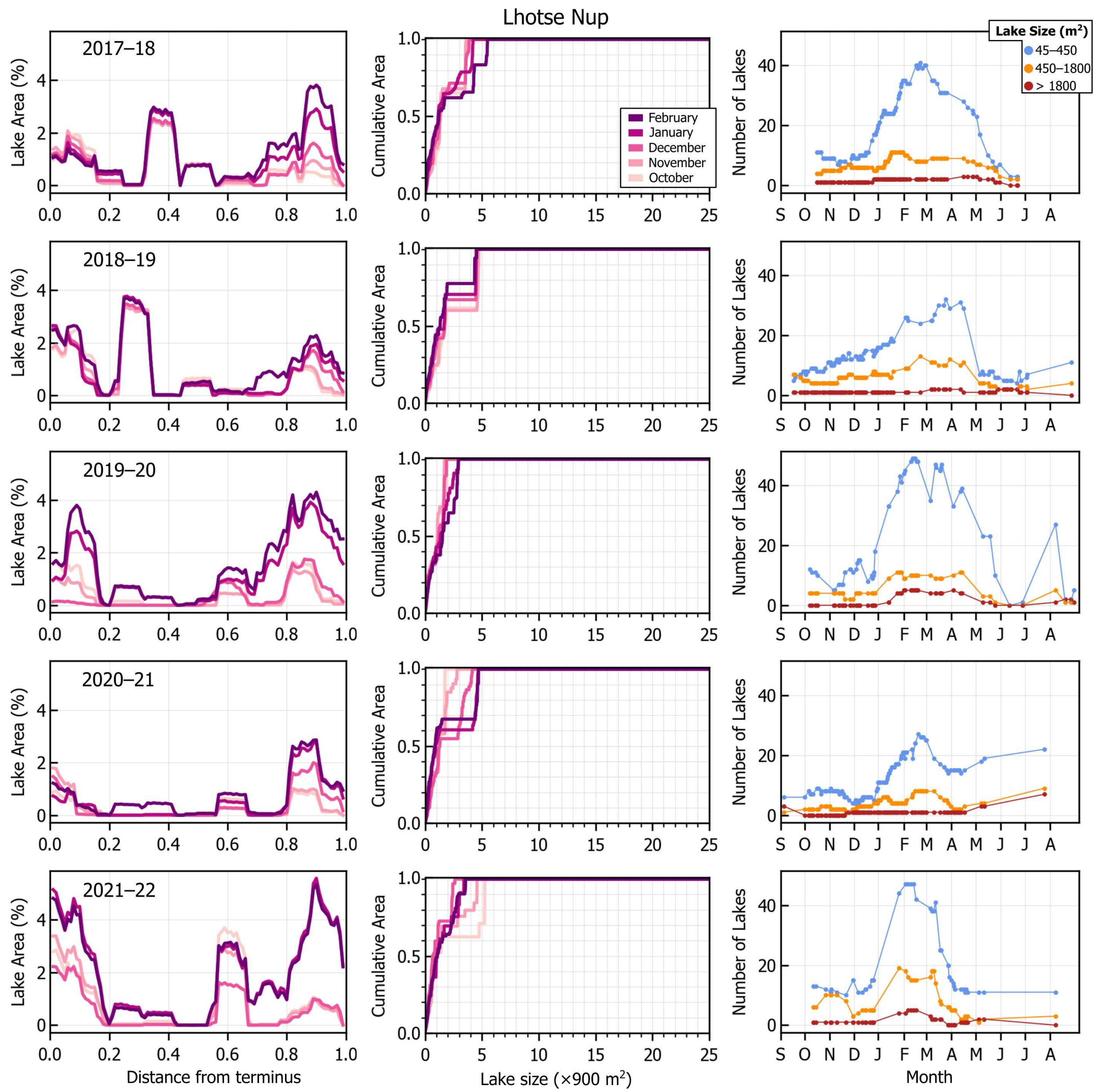

Figure B9: Seasonality in lake area and count on Lhotse Nup Glacier, presented identically as Figure 20.

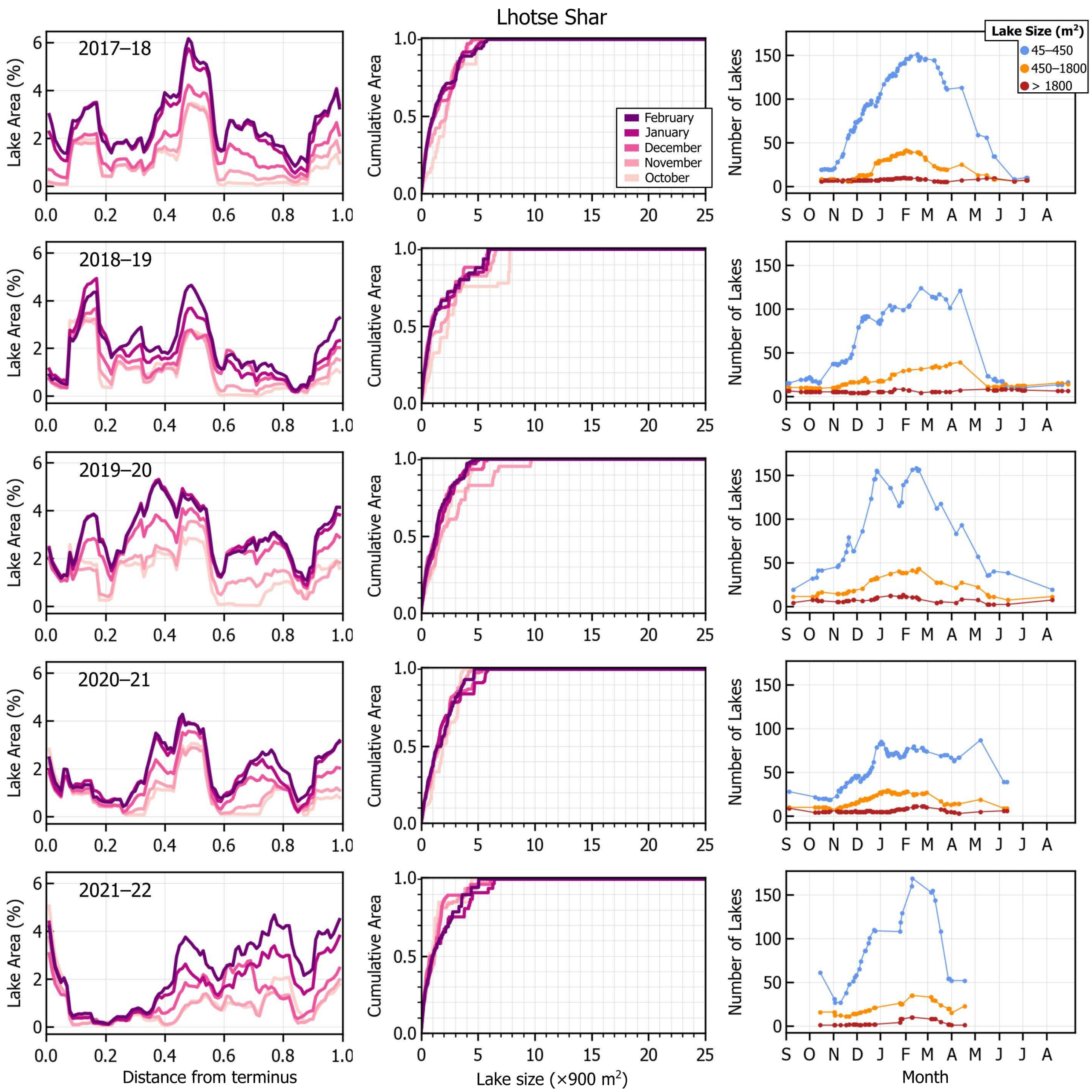

Figure B10: Seasonality in lake area and count on Lhotse Shar Glacier, presented identically as Figure 20.

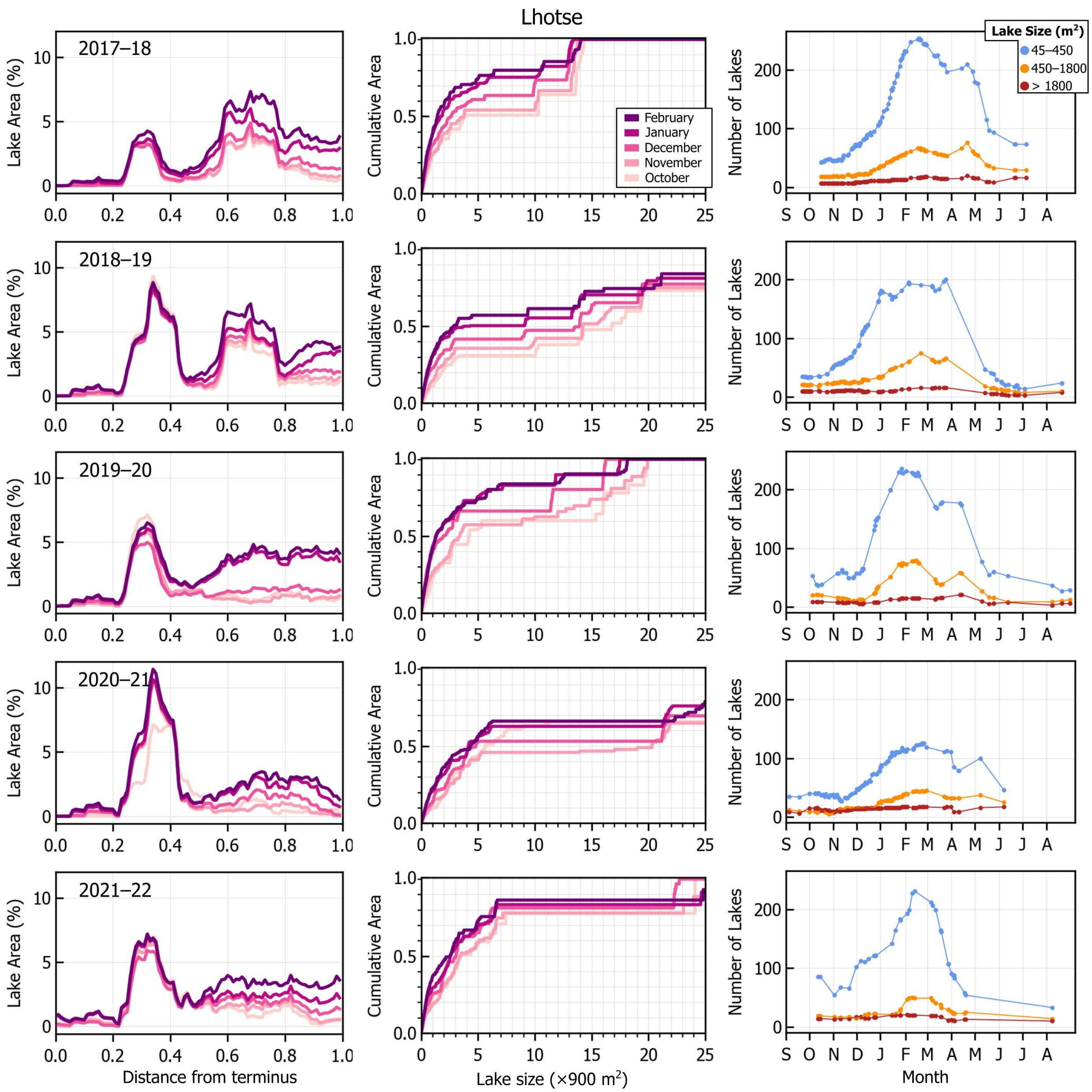

Figure B11: Seasonality in lake area and count on Lhotse Glacier, presented identically as Figure 20.

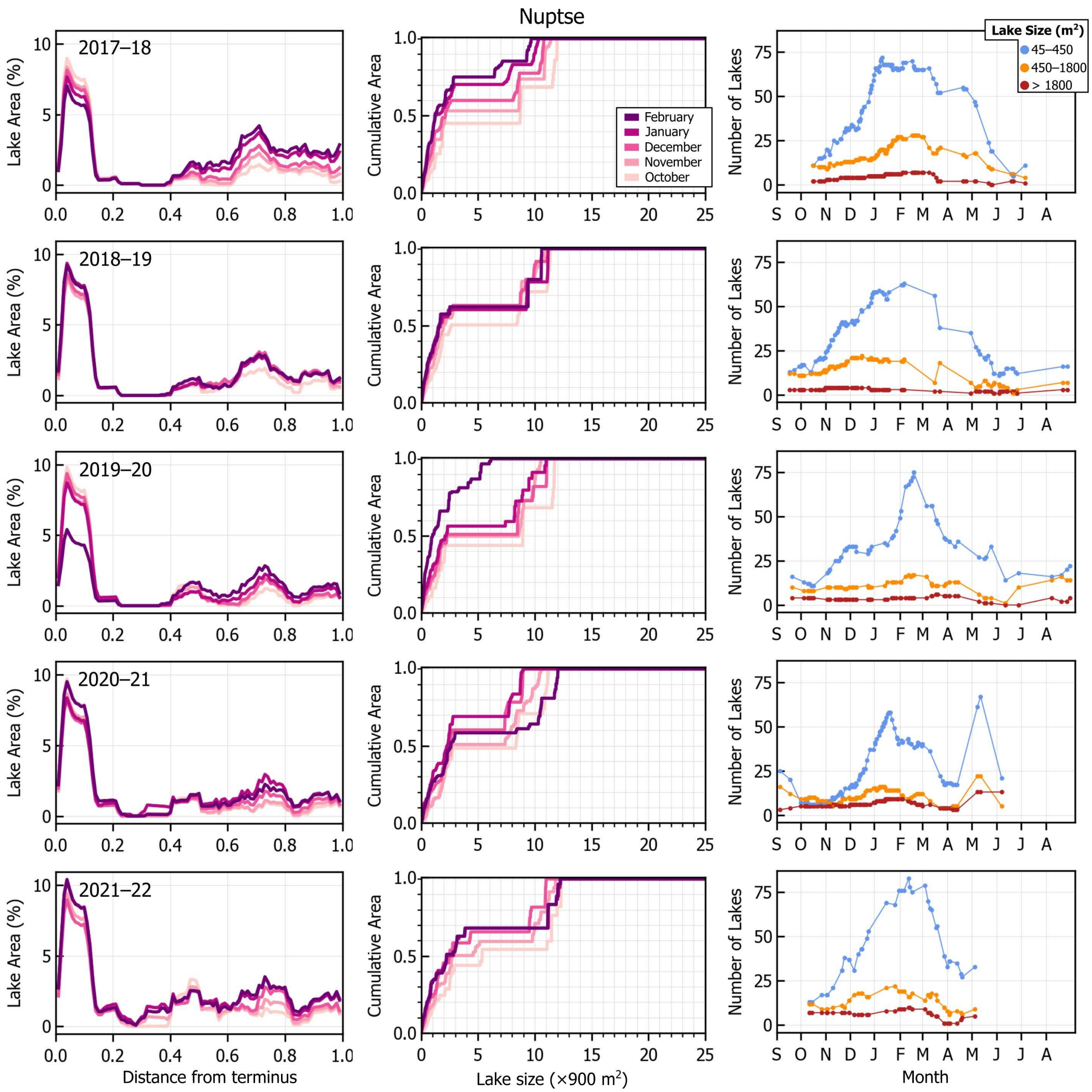

Figure B12: Seasonality in lake area and count on Nuptse Glacier, presented identically as Figure 20.

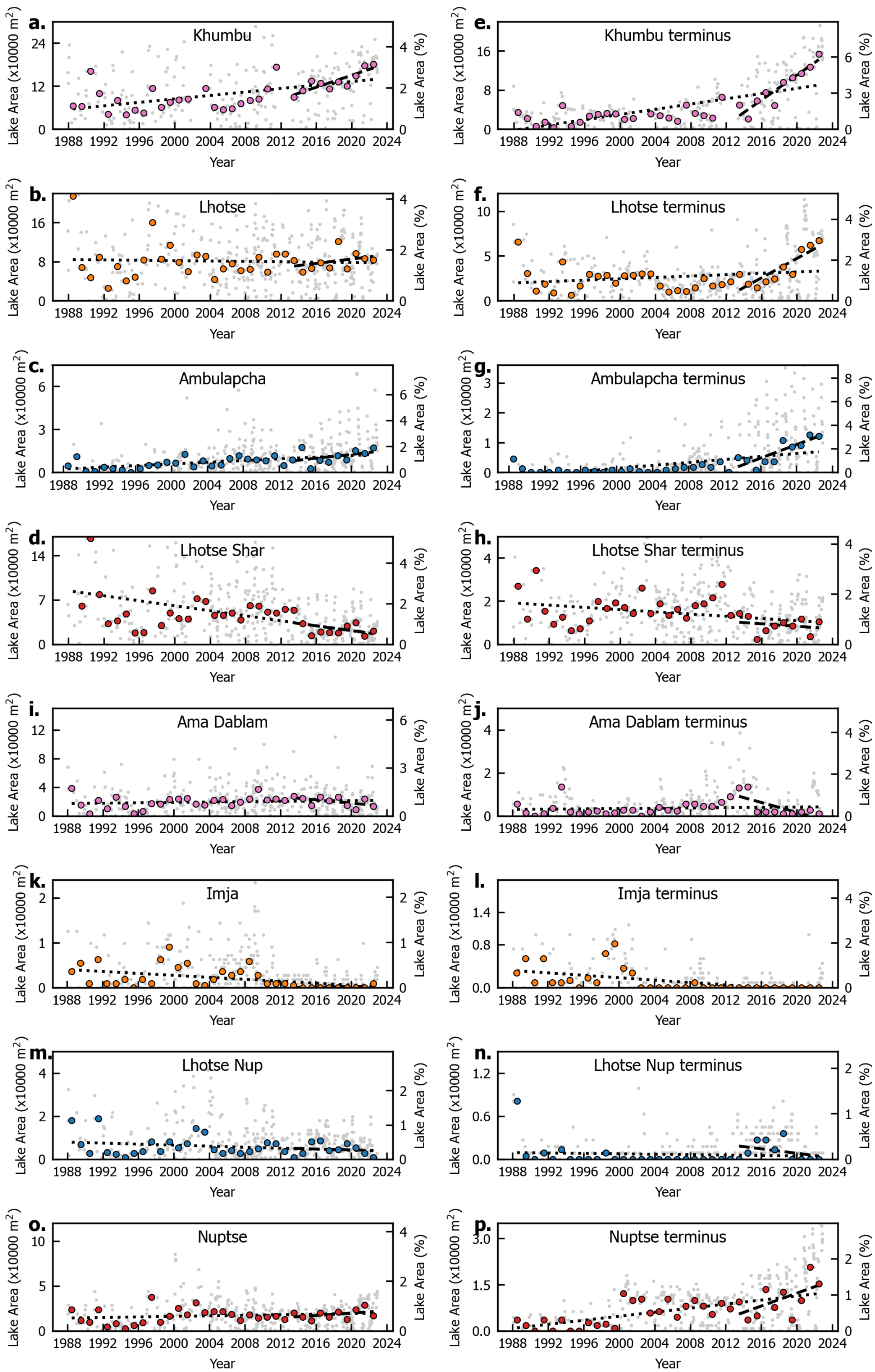

Figure B13: Landsat-derived time series of SGL area of all 8 glaciers.

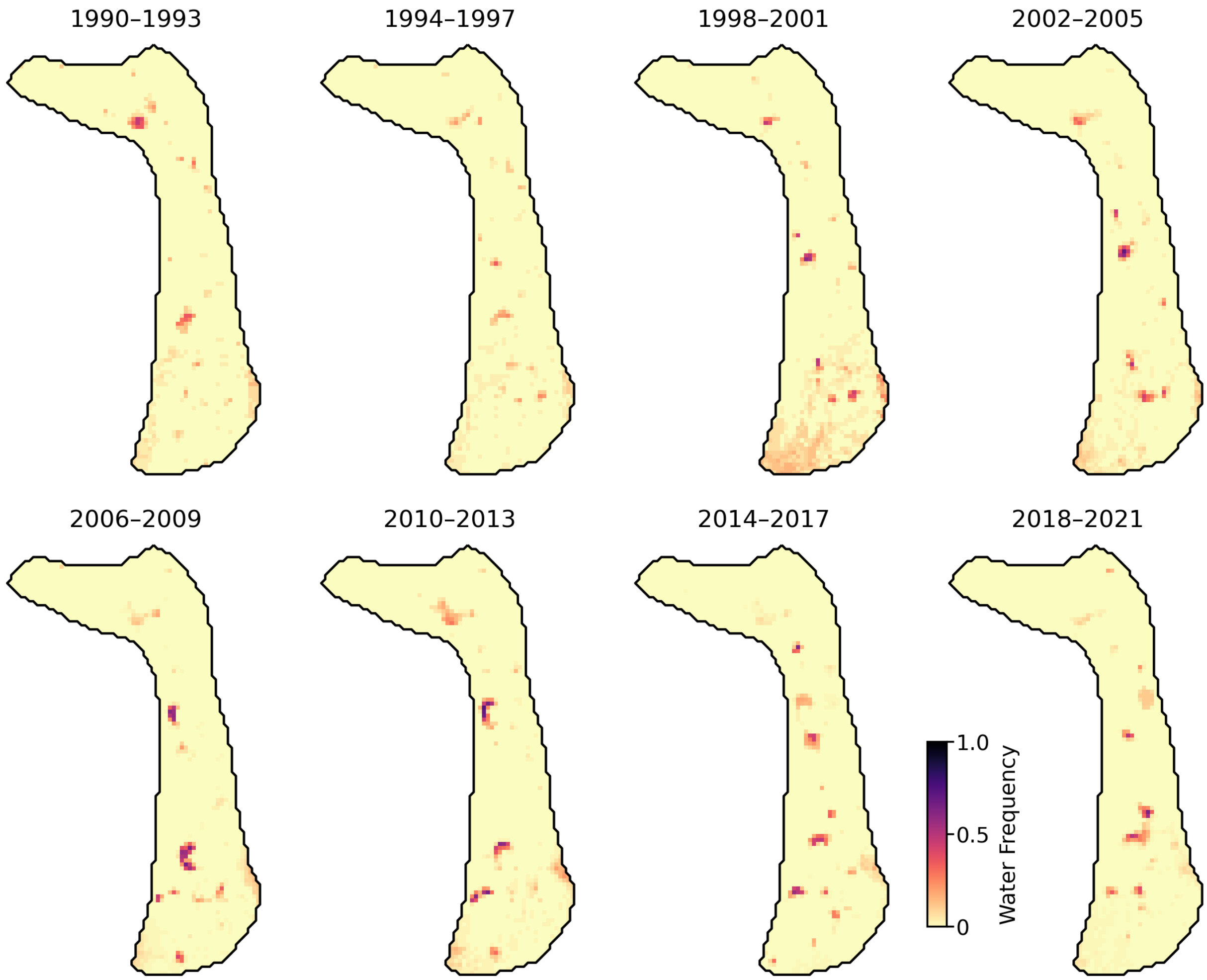

Figure B14: Repeat 4-year maps of SGLs on Ama Dablam Glacier, from Landsat imagery.

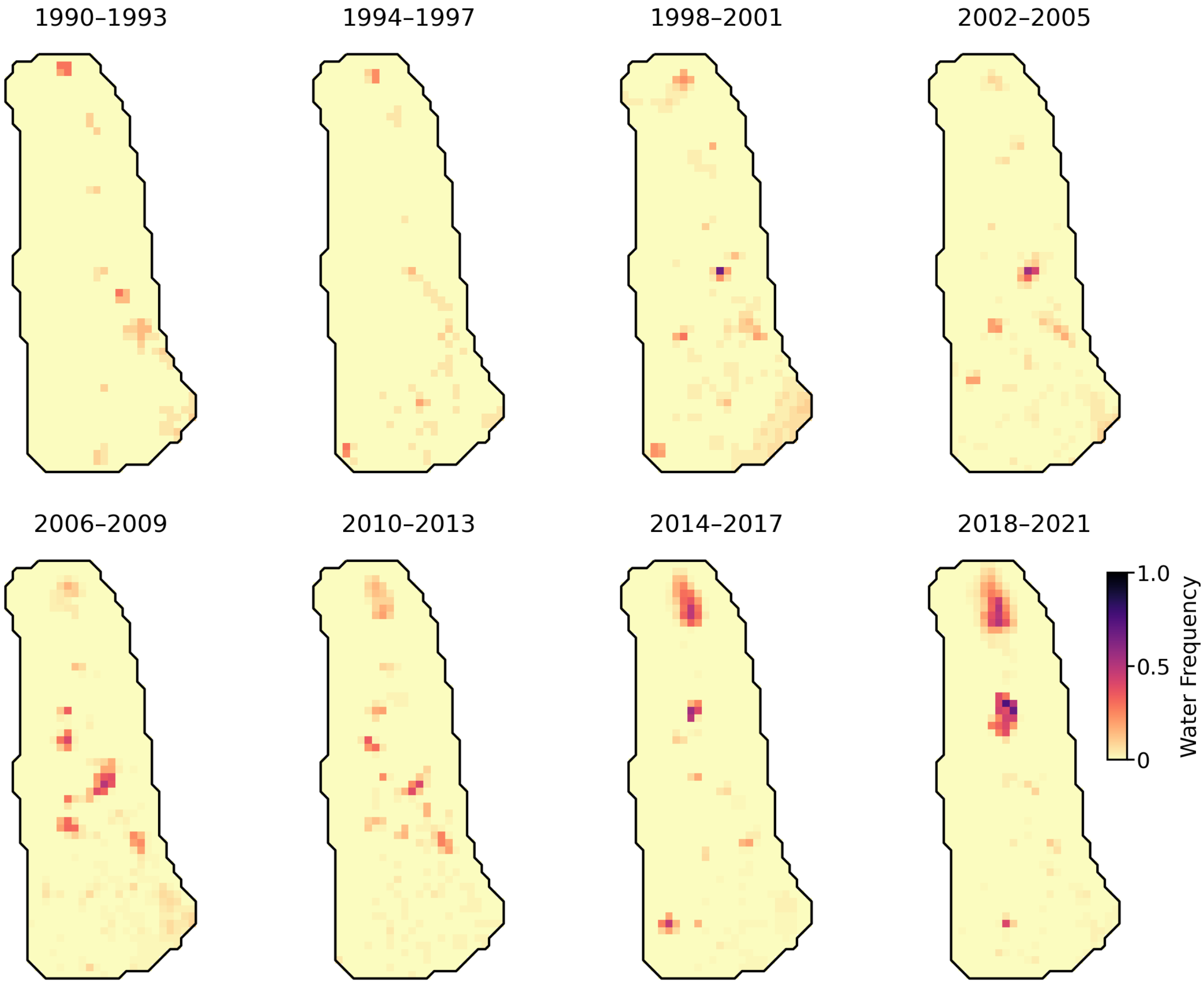

Figure B15: Repeat 4-year maps of SGLs on Ambulapcha Glacier, from Landsat imagery.

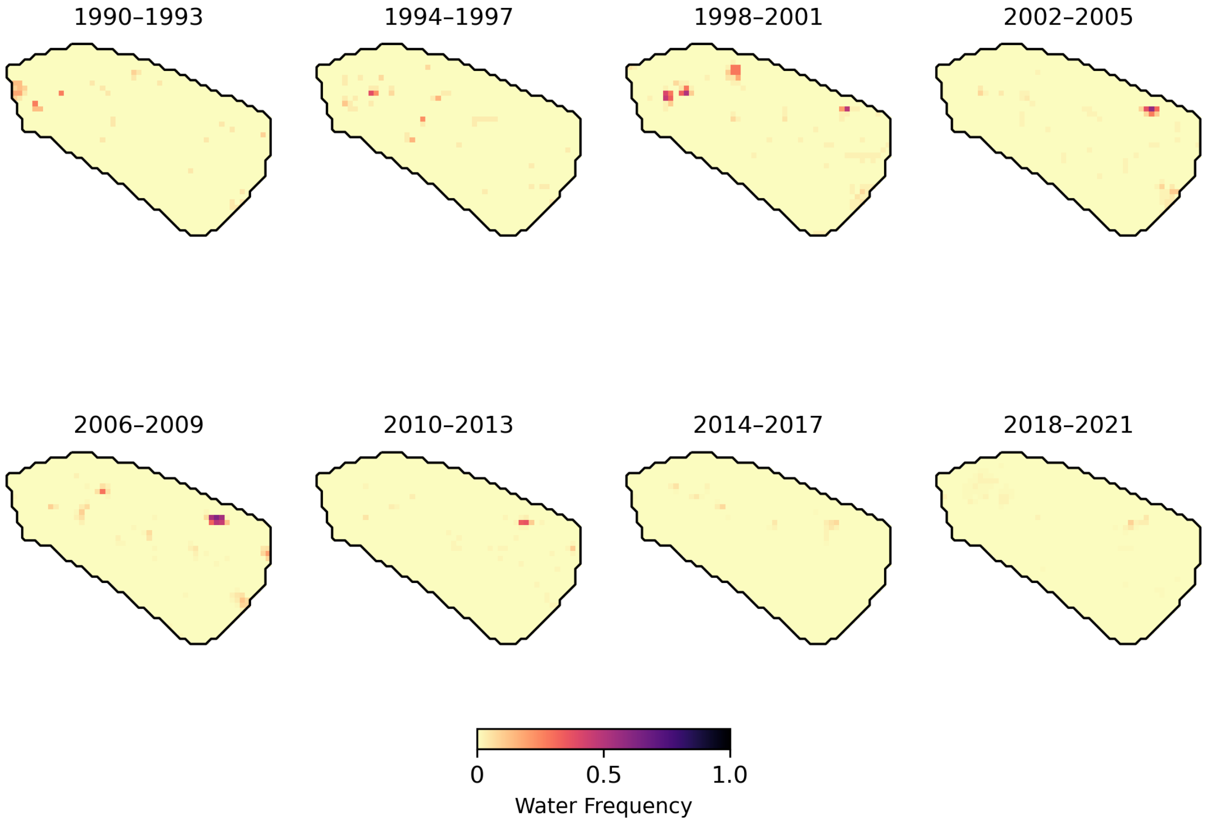

Figure B16: Repeat 4-year maps of SGLs on Imja Glacier, from Landsat imagery.

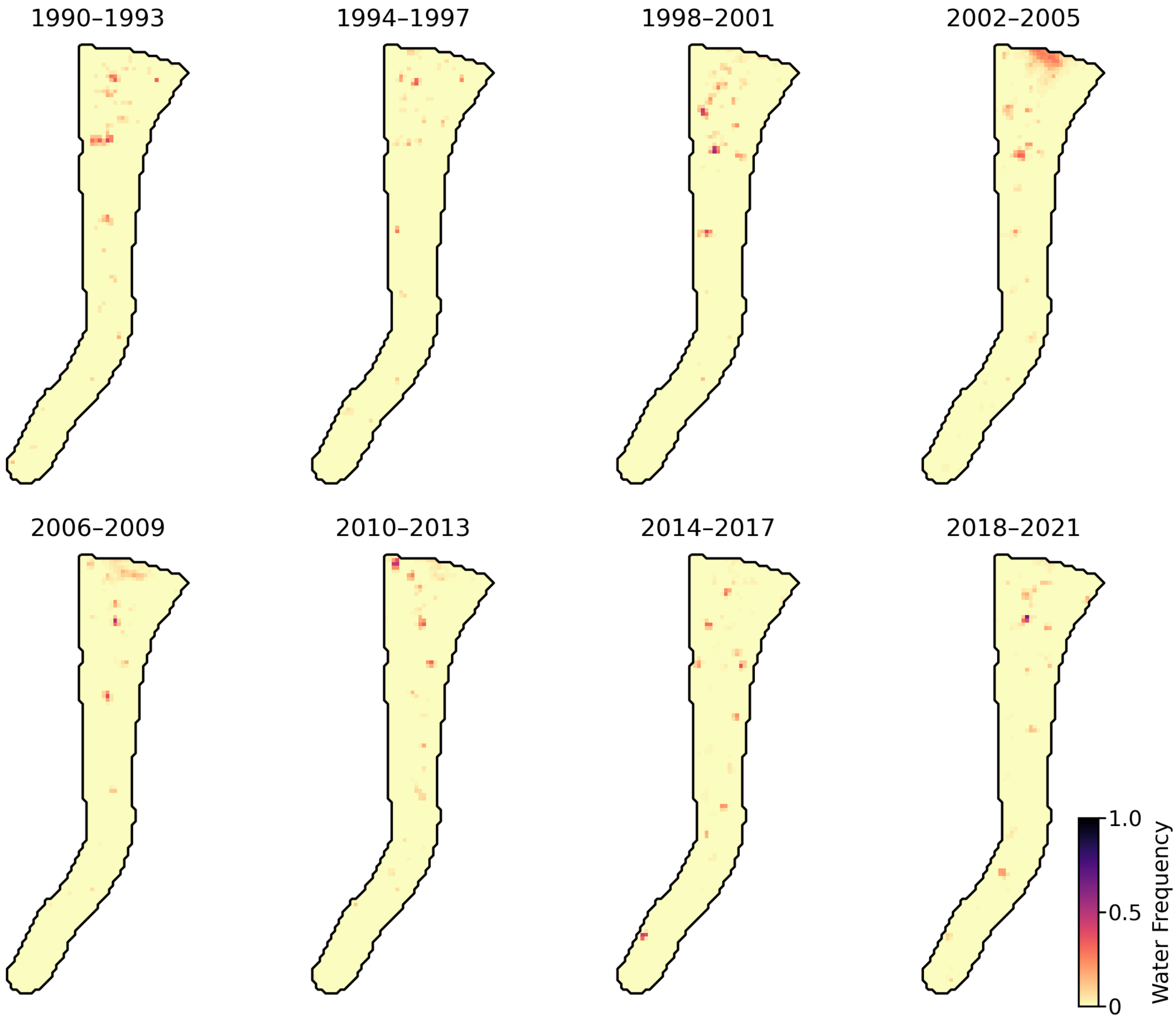

Figure B17: Repeat 4-year maps of SGLs on Lhotse Nup Glacier, from Landsat imagery.

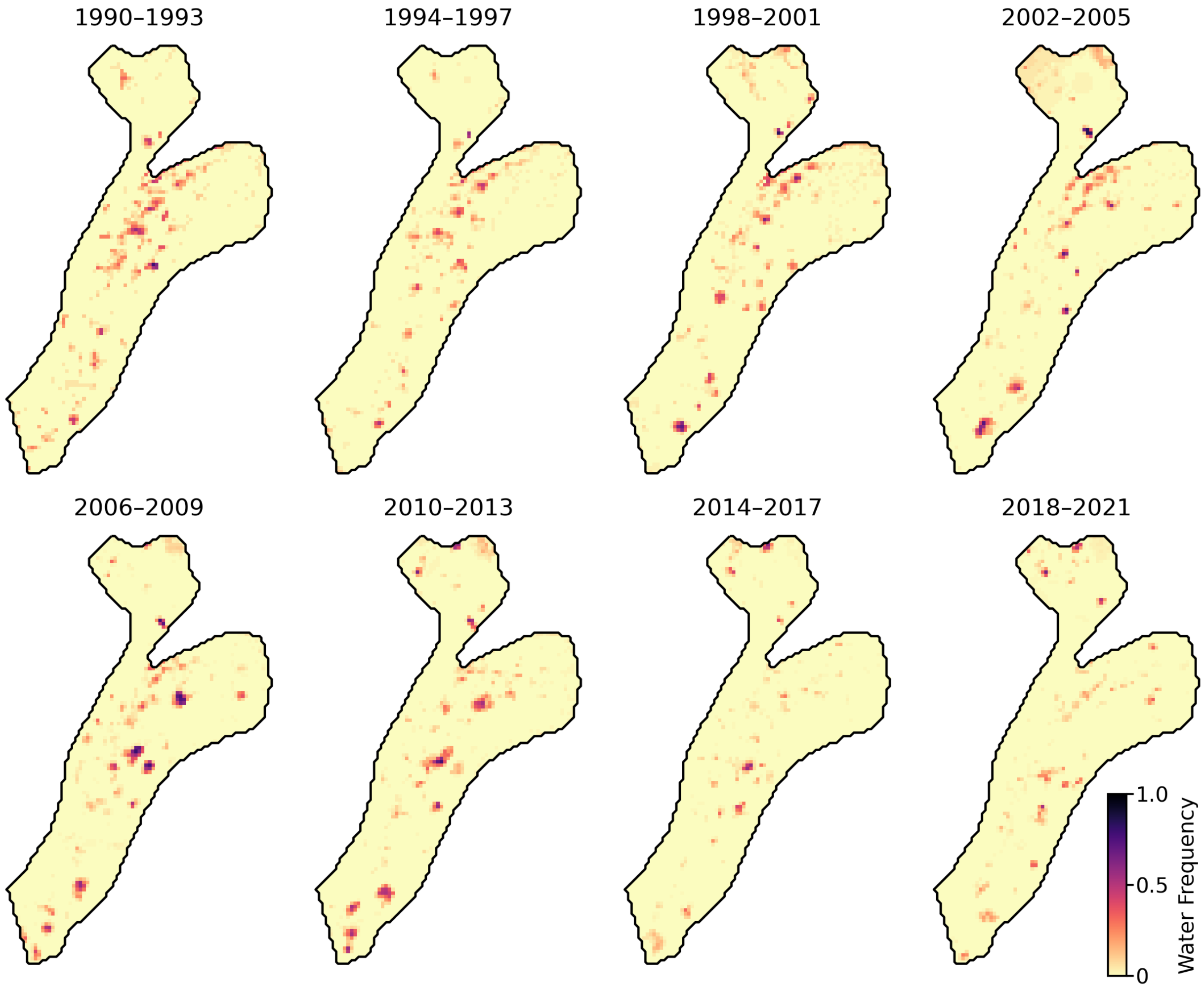

Figure B18: Repeat 4-year maps of SGLs on Lhotse Shar Glacier, from Landsat imagery.

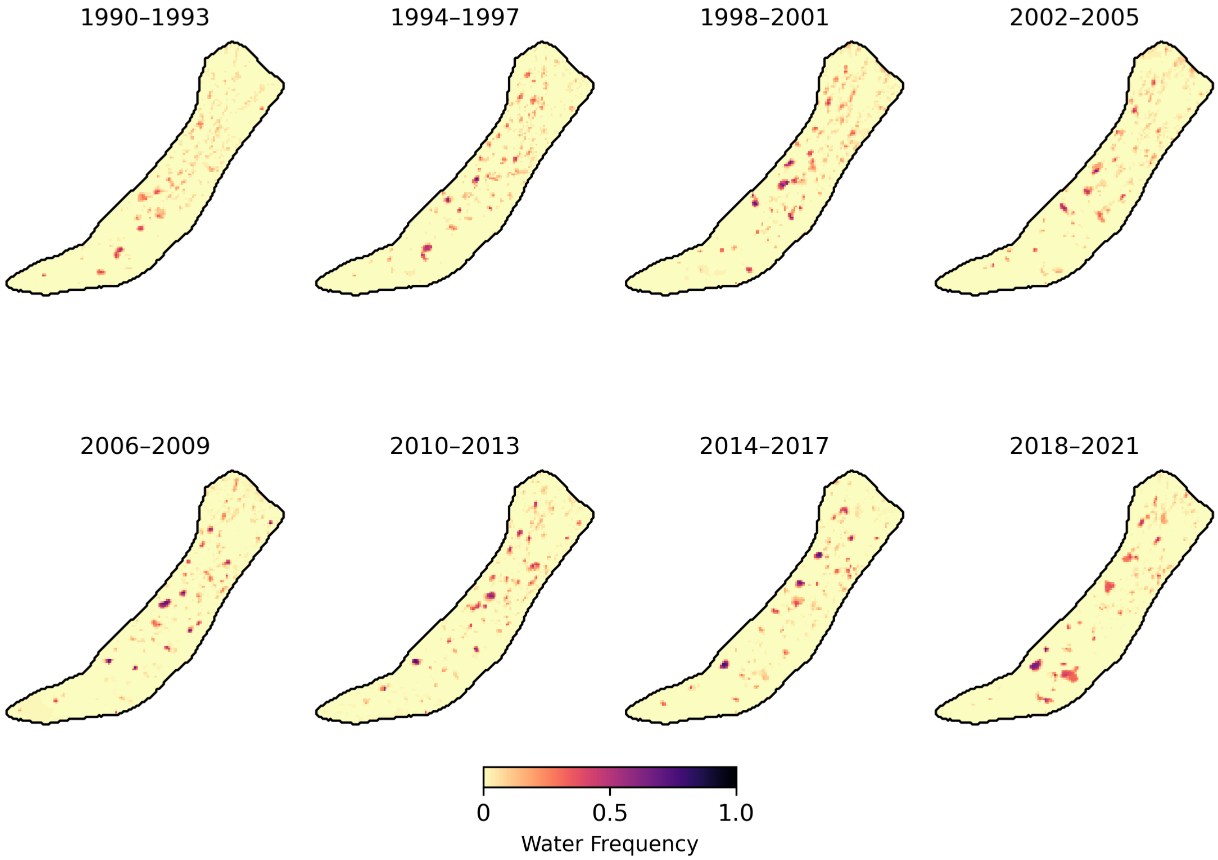

Figure B19: Repeat 4-year maps of SGLs on Lhotse Glacier, from Landsat imagery.

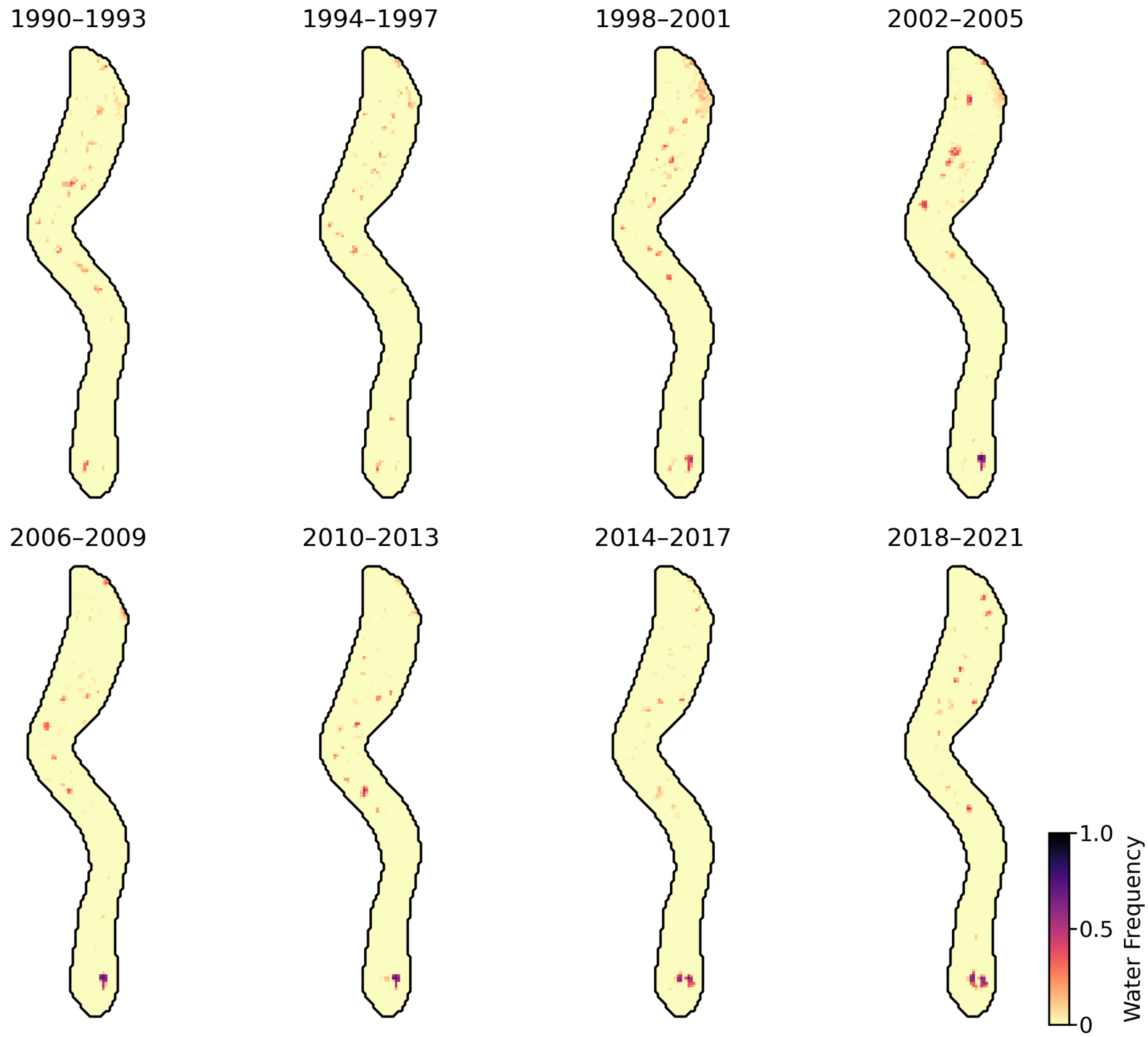

Figure B20: Repeat 4-year maps of SGLs on Nuptse Glacier, from Landsat imagery.

APPENDIX C: SUPPLEMENT TO CHAPTER 3

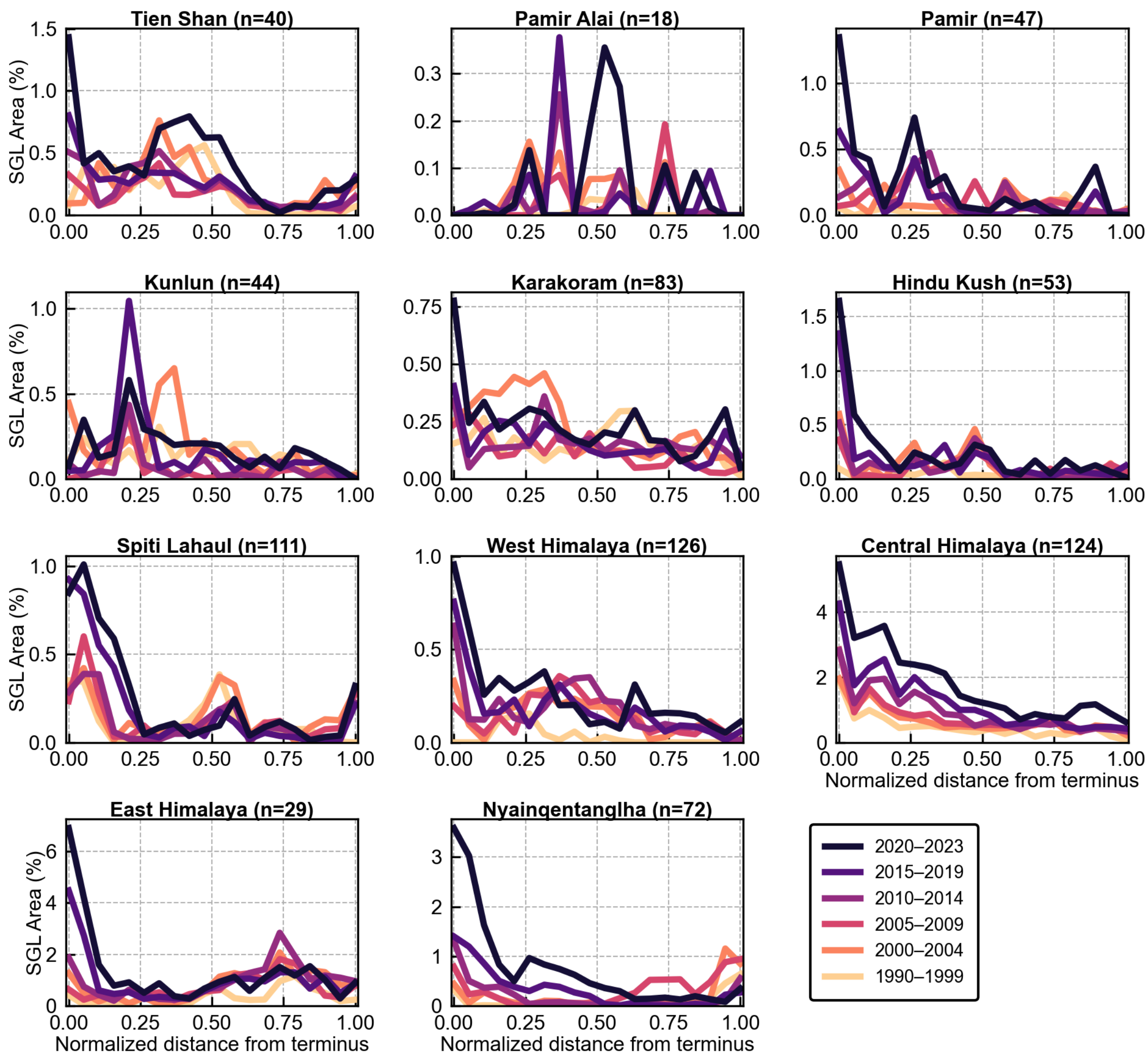

Figure C1: Changing patterns of SGL distribution as a function of distance from the glacier termini, broken down into the 11 subregions used in Chapter 3.